UNIVERSITY OF OKLAHOMA

GRADUATE COLLEGE

THE IMPACT OF ADDITIVES IN ACIDIC ZEOLITES ON HYDROCARBON-BASED REACTIONS

A DISSERTATION

SUBMITTED TO THE GRADUATE FACULTY

in partial fulfillment of the requirements for the

Degree of

DOCTOR OF PHILOSOPHY

By

NABIHAN ABDUL RAHMAN

Norman, Oklahoma

2024

Downloaded from SHAREOK. Persistent Handle URL: https://hdl.handle.net/11244/340404

THE IMPACT OF ADDITIVES IN ACIDIC ZEOLITES ON HYDROCARBON-BASED REACTIONS

A DISSERTATION APPROVED FOR THE
SCHOOL OF SUSTAINABLE CHEMICAL, BIOLOGICAL AND MATERIALS ENGINEERING

BY THE COMMITTEE CONSISTING OF

Dr. Daniel E. Resasco, Chair

Dr. Zhibo Yang

Dr. Steven P. Crossley

Dr. Bin Wang

Dr. Lance Lobban

© Copyright by NABIHAN ABDUL RAHMAN 2024
All Rights Reserved.

Untuk Ayah, Mama, dan sekeluarga.

Acknowledgment

First, I am immensely grateful to Dr. Daniel Resasco for accepting me into his research group and for being a constant source of inspiration throughout my academic journey. His dedication to research and his innovative approach to problem-solving have greatly influenced my own thinking. I am truly humbled to be mentored by someone as knowledgeable and experienced as him. Under his guidance, my horizons have been broadened, and I have been given the opportunity to grow not only as a researcher but also as a storyteller, learning to communicate complex ideas with clarity and precision. I am deeply thankful for his mentorship and the impact he has had on my development as a scientist.

Next, I would like to express my deepest gratitude to my parents, whose unwavering support and boundless love have been the cornerstone of my journey. Their encouragement, sacrifices, and belief in my abilities have been my main motivation, propelling me forward even in the face of challenges. Their endless support has kept me going, inspiring me to strive for excellence and pursue my dreams. I dedicate this thesis to them, with the hope of making them proud.

I would also like to thank Dr. Steven Crossley, Dr. Lance Lobban, Dr. Bin Wang, and Dr. Jefferey White. Their feedback, guidance, and insightful discussions have been instrumental in shaping me into the researcher I am today. Their diverse expertise and perspectives have broadened my view of catalysis and have instilled in me a curiosity for exploring different research areas within the field. I am grateful for the opportunity to work alongside such brilliant minds, and I am inspired by their passion for research and their commitment to excellence.

I am also grateful for the invaluable contributions of the current and past students in our research group, including Dr. Nilson de Paula, Dr. Felipe Anaya, Daniela Santos Trejos, Dr.

Gengnan Li, Dr. Yang Feifei, Dr. Reda Babarik, Ismaeel Alalq, Dr. Alejandra Gomez, Dr. Ana Carolina Jerdy, Dr. Han Chau, Thomas Salas, Caleb BavInka, as well as Anya Zornes and Omio Dias from Oklahoma State University. Their passion for catalysis and their willingness to engage in insightful discussions have always been a source of inspiration for me. I have learned so much from our interactions, and I am thankful for the camaraderie and collaboration that have defined our research environment. Their diverse perspectives and experiences have enriched my own research journey, and I am grateful for the opportunity to work alongside them. I will be monitoring their future careers with great interest and hope that we can stay connected.

I would like to express my sincere gratitude to Phillips 66 for their generous student scholarship support throughout my PhD studies. This scholarship also provided me with invaluable opportunities to closely collaborate with the company, gaining insightful perspectives into industrial applications and research. I am truly thankful for the support and guidance I have received, which has greatly enriched my academic and professional journey.

I would like to thank Majlis Amanah Rakyat (MARA) and the Malaysian government for the ample opportunities they have provided me to study abroad. Their support and investment in my education have been instrumental in shaping my academic and personal growth. I am forever grateful for their belief in me and for giving me the chance to pursue my dreams on an international platform. Thank you for your unwavering support and for believing in the power of education.

Finally, I would like to express my heartfelt gratitude to my two furry companions, Haru and Toast. Their presence in my life has been a constant source of comfort and joy, especially during challenging times. I am so grateful that I adopted them during my PhD, as they have become an integral part of my life's journey.

Table of Contents

Acknowledgment ..... *v*
Table of Contents ..... *vii*
List of Tables ..... *x*
List of Figures ..... *xii*
List of Schemes ..... *xix*
Abstract ..... *xx*
Chapter 1: General Introduction *1*
1.1 Crude Oil and Petrochemical industries 2
1.3 Zeolites 3
1.3.2 Properties of Zeolites 3
1.4 Metal additives in zeolites 4
1.4.2 Addition of sodium (Na) and calcium (Ca) as Bronsted acid titrant 5
1.4.3 Usage of Lanthanum as additive 5
1.5 Hydrocarbon reactions over acidic zeolites 6
1.5.1 Alkane cracking and activation over Bronsted acid 6
1.5.1.1 Monomolecular cracking mechanism – Carbonium ion transition state 6
1.5.1.2 Bimolecular Cracking mechanism via Hydrogen transfer – Carbenium ion formation and β-scission 8
1.5.2 Aromatic Alkylation Reaction 11
1.6 Importance of Hydrogen Transfer in chemical processes 12
1.7 Hydrogen transfer reaction probes 13
1.7.1 Alkane to alkene ratio of the product stream during alkane cracking 13
1.7.2 Cyclohexene 14
1.7.3 Isobutane/butene alkylation reaction 14
1.8 Scope of thesis 16Chap
Chapter 2: Investigating the interplay of hydrogen transfer, protolytic cracking, and dehydrogenation reactions over faujasite zeolites by using isooctane conversion as a probe .. 17
2.1 Introduction 18
2.2 Materials and Methodologies 20
2.2.1 Materials 20
2.2.2 Powder X-Ray Diffraction (XRD) 21
2.2.3 Isopropylamine Temperature Programmed Reaction/Decomposition (IPA-TPD)22
2.2.4 Catalytic Reaction 22

2.2.5 Determining the rate and distribution of protolytic cracking, hydrogen transfer and dehydrogenation. 23
2.3 Results and Discussion 25
2.3.2 Isooctane Cracking Reaction Mechanism Over Acid Sites – Hydrogen Transfer, Protolytic Cracking, and Dehydrogenation Pathways 27
2.3.3 Enhanced Dehydrogenation Pathway by Cobalt Titration and Gas-Phase Hydrogen Donation from 2,3-Dimethylbutane 34
2.3.4 Shortcomings of using C_4/C_4= ratio as an indicator of hydrogen transfer activity in isooctane cracking 35
2.3.5 Role of synergistic sites– varying Na titration level in Y15 zeolite 36
2.3.6 Y15 and titrated Y15 Analysis using Ternary Plots 38
2.3.7 Case study: Understanding the role of Lanthanum in alkane cracking using isooctane cracking as a probe reaction. 41
2.5 Conclusion 52
Chapter 3: Lanthanum-Incorporated Zeolite Y: Impact of La on Physical and Acid Properties of the zeolite and its Influence on Isooctane Cracking Performance 53
3.5 Introduction 54
3.7 Experimental and Methodologies 56
3.7.2 Materials and Catalysts Synthesis. 56
3.7.3 Catalyst Characterizations 57
3.7.3.1 Elemental analysis 57
3.7.3.3 BET pore analysis 59
3.7.3.4 Isopropylamine Temperature Programmed Reaction/Decomposition (IPA-TPD) 59
3.7.3.5 Ammonia Temperature Programmed Desorption, NH_3-TPD. 59
3.7.3.6 X-Ray Diffraction (XRD). 60
3.7.3.7 FTIR Spectroscopy. 60
3.7.3.8 Isooctane heat of adsorption calorimetry. 61
3.7.3.9 Catalytic Test 61
3.8 Results 61
3.8.2 Effects of La on the physical and structural properties of zeolite Y 62
3.8.3 Effects of La on the acid properties of zeolite Y 71
3.8.4 Effects of La on activity, selectivity, and activation energy during isooctane cracking 76
3.10 Discussions 86
3.11 Conclusion 91

Chapter 4: Incorporation of Lanthanum in H-MOR Zeolite to Improve Shape Selectivity and Stability Against Coke Formation during Toluene Alkylation with Isopropanol 92
4.5 Introduction 93
4.6 Experimental and Methodologies 95
4.6.2 Chemicals and Materials 95
4.6.3 Catalyst Preparation 95
4.6.4 Catalyst Characterization 96
4.6.4.1 BET Surface area and pore volume 96
4.6.4.2 Temperature Program Desorption (TPD) 96
4.6.4.3 X-ray Diffraction (XRD) 97
4.6.4.4 Fourier Transform Infrared Spectroscopy (FTIR) 97
4.6.4.5 Thermogravimetric Mass Spectroscopy (TG-MS) 98
4.6.4.6 Solid state ^{13}C-MAS NMR 98
4.6.5 Catalytic Test 99
4.6.5.1 Liquid phase batch reactor 99
4.6.5.2 Gas-phase continuous-flow reactor 101
4.6.5.2.1 Alkylation reaction 101
4.6.5.2.2 Isooctane cracking reaction 101
4.7 Results 102
4.7.2 Fresh Catalysts Characterizations 102
4.7.2.1 Physical Properties 102
4.7.2.2 Acidic Properties 103
4.7.3 Alkylation Reaction 108
4.7.3.1 Reaction Pathways 108
4.7.3.2 Shape selectivity 109
4.7.3.3 Catalyst stability 110
4.7.4 Post Reaction Catalysts Characterizations 112
4.7.5 Isooctane cracking reaction 116
4.7.6 Comparing La-MOR and Na-MOR 117
4.8 Discussions 118
4.9 Conclusion 119
References 121

List of Tables

Table 1. Bronsted acid site density and elemental analysis of Y15, Y15Na, Y15Ca, and Y15Co. 25

Table 2. Turnover frequency (TOF) of protolytic cracking and hydrogen transfer for Y15, Y15Na and Y15Ca. Reaction conditions: pulse mode, isooctane partial pressure was 1.7 kPa, the carrier gas flow rate was 100 mL/min, at 400ºC and 1 atm. Reaction for all catalysts under similar range of isooctane conversion (8-10%). 33

Table 3. Bronsted acid site density of Y2.6 and LaY2.6. 42

Table 4. Zeolite synthesis step and history notation 56

Table 5. Simplified name of some of the samples used in this work. 57

Table 6. Lanthanum loading and the bulk SI/Al ratio 62

Table 7. BET surface area and pore volume of HY and LaY samples. 63

Table 8. Total acid density, Bronsted acid density, and the fraction of Bronsted acid density from NH3-TPD and IPA-TPD. 74

Table 9. Series of reactions in the cracking of isooctane over Bronsted acid sites via protolytic cracking and hydrogen transfer. 80

Table 10. Rate constants for HY and 1.0LaY during isooctane cracking. . Reaction conditions: continuous flow reactor at 2.4 kPa of isooctane partial pressure, 80 mL/min of carrier gas flow, 400ºC, 1 atm. 82

Table 11. Lanthanum weight% for all La-MOR samples 96

Table 12. BET surface area and pore volume of fresh samples. 103

Table 13. Total acid density, Bronsted acid density, and Lewis acid density of fresh samples. 104

Table 14. Deactivation coefficient of alkylation reaction for all catalysts in both liquid phase batch reaction and gas phase continouds flow reaction. 111

Table 15. Amount of coke depsotied and Bronsted acid sites retained after reaction 114

List of Figures

Figure 1. Protolytic cracking of n-butane and possible products. A) Methane and propyl carbenium ion B) Ethane and ethyl carbenium ion. C) Dihydrogen and butyl carbenium ion..... 7

Figure 2. Bimolecular cracking mechanism of isooctane via hydrogen transfer and β-scission... 8

Figure 3. Classification of β-scission step of alkylcarbenium ion. Retrieved from [41] 10

Figure 4. XRD patterns of Y15, Y15 Na, Y15 Ca, and Y15 Co..... 26

Figure 5. SEM images of Y15 (A), Y15 Na (B), Y15 Ca (C), Y15 Co (D), and the particle size distributions (E). 26

Figure 6. Products distribution and conversion of 2-methylhexane cracking over Y15 zeolite in flow mode. Red bars: 400 ºC, green bars: 410 ºC, blue bars: 420 ºC. Subsequent bar of a given color represents various iC8 feeding rate: 0.4, 0.6 and 0.8 mL/hr. Reaction conditions: 50 mg, 80 mL/min of He flow. Pretreatment under He flow at 300 ºC for 2 hours. 29

Figure 7. Experimental data of parent, Na and Ca titrated Y15 for both pulse mode and flow mode reactor at various conversion, along with the proposed correlation. Reaction conditions: Both, in the feed to the continuous flow reactor and the injection loop to the micropulse reactor the isooctane partial pressure was 1.7 kPa; in both cases, the carrier gas flow rate was 100 mL/min, at 400ºC and 1 atm. The conversion was varied by changing the catalyst mass in the range 5-30 mg. 33

Figure 8. C4 vs C1 selectivity plot of Co titrated Y15, and isooctane cofed with dimethylbutane over Y15 and Y15Na. Reaction conditions: Both, in the feed to the continuous flow reactor and the injection loop to the micropulse reactor the isooctane partial pressure was 1.7 kPa; in both cases, the carrier gas flow rate was 100 mL/min, at 400ºC and 1 atm. The conversion was varied by changing the catalyst mass in the range 5-30 mg. DMButane was cofed at 1.2 kPa..... 34

Figure 9. C4/C4= ratio of varying isooctane conversion over parent (◆), Na- (▼), Ca- (■), and Co- (▲) titrated Y15 zeolite. Reaction conditions: micropulse mode reactor at 1.7 kPa of isooctane partial pressure, 100 mL/min of carrier gas flow, 400ºC, 1 atm. The conversion was varied by changing the catalyst mass, 5-30 mg. Error bars are the deviation of six subsequent pulses of isooctane. 36

Figure 10. Conversion of isooctane per Bronsted site over Y15 at various level of Na titration. Reaction conditions: 400ºC, 3.5 mg, flow mode, 250 min time on stream. Error bars reflect the deviation in activity over the whole time on stream. 37

Figure 11. A) Ternary Plot of various titrated Y15 samples for both flow mode and pulse mode, B) Pulse mode region, C) Flow mode region. 40

Figure 12. C4/C4= ratio of Y2.6 (▲) and LaY2.6 (■) at various catalytic conversions. Reaction conditions: continuous flow reactor at 2.4 kPa of isooctane partial pressure, 80 mL/min of carrier gas flow, 400ºC, 1 atm. The conversion was varied by changing the catalyst mass, 10-75mg.... 43

Figure 13 Ternary plot of Y2.6 (▲) and LaY2.6 (■) at various catalytic conversions. Reaction conditions: continuous flow reactor at 2.4 kPa of isooctane partial pressure, 80 mL/min of carrier gas flow, 400ºC, 1 atm. The conversion was varied by changing the catalyst mass, 10-75mg, and time on stream, 15-135 mins..... 45

Figure 14. Turnover frequency (TOF) of Y2.6 (▲) and LaY2.6 (■) at various isooctane conversion. A) protolytic cracking, B) hydrogen transfer, C) dehydrogenation. Reaction conditions: continuous flow reactor at 2.4 kPa of isooctane partial pressure, 80 mL/min of carrier gas flow, 400ºC, 1 atm. The isooctane conversion was varied by changing the catalyst mass, 10-150 mg. 46

Figure 15. Isooctane cracking over Y2.6 and LaY2.6 at various isooctane partial pressure. Y2.6 (▲) ternary plot; B) LaY2.6 (■) ternary plot. Reaction conditions: continuous flow reactor at 0.3-7.2 kPa of isooctane partial pressure, 30 mg catalyst, 80 mL/min of carrier gas flow, 400ºC, 1 atm..... 47

Figure 16. Turnover frequencies (TOF) of Y2.6 (▲) and LaY2.6 (■) at various isooctane partial pressure. A) protolytic cracking, B) hydrogen transfer, C) dehydrogenation. Reaction conditions: continuous flow reactor at 0.3-7.2 kPa of isooctane partial pressure, 30 mg catalyst, 80 mL/min of carrier gas flow, 400ºC, 1 atm. 48

Figure 17. Natural log of overall isooctane cracking rate versus natural log of isooctane partial pressure. Reaction conditions: continuous flow reactor at 0.3-7.2 kPa of isooctane partial pressure, 30 mg catalyst, 80 mL/min of carrier gas flow, 400ºC, 1 atm. While the observed reaction order is about 1 for the parent Y2.6 zeolite in the entire range, the LaY2.6 sample exhibits two regimes, first order at low partial pressures and second order at high partial pressures..... 49

Figure 18. Isooctane conversion as a function of time on stream over LaY2.6 at A) varying isooctane partial pressure and B) first order partial pressure region. Reaction conditions: continuous flow reactor, 80 mL/min of carrier gas flow, 400ºC, 1 atm, 50mg. 49

Figure 19. Ternary plot of isooctane cracking over Y30 zeolites with various lanthanum loadings and isooctane conversion. Reaction conditions: continuous flow reactor at 2.4 kPa of isooctane partial pressure, 80 mL/min of carrier gas flow, 20-120 mg catalyst, 400ºC, 1atm. All reactions are below 3% isooctane conversion to minimize sequential reactions. 50

Figure 20. A) Nitrogen adsorption-desorption isotherms; B) the HK pore size distribution of the various La samples. Size <1.0 nm was calculated using HK method (micropore). Size >1.0 nm was calculated using BJH method (mesopore) 65

Figure 21. A) XRD patterns of 2θ between 10° and 40° for HY and LaY samples. B) Amplified XRD patterns between 10° and 20° for HY and LaY samples. 66

Figure 22. Percent distribution of (311) peak and (222) peak as a function of La loading 67

Figure 23. XRD patterns of LaY samples at varying stages of synthesis 70

Figure 24. NH_3-TPD and IPA-TPD for all samples. A) Ammonia profiles from NH_3-TPD with peak deconvolution B) Propylene profiles from IPA-TPD..... 73

Figure 25. A) Total acid density and Bronsted acid density at various La loadings via NH_3-TPD and IPA-TPD. B) Fraction of the middle peak in NH_3-TPD versus fraction of Bronsted from IPA-TPD to total acid from NH_3-TPD..... 74

Figure 26. A) FTIR spectra of HY and LaY samples at varying La loadings in the hydroxyl region. B) Distribution of area under the peak for the four bands found from the FTIR spectra for the various zeolite samples. All spectra were recorded at 300 °C. 75

Figure 27. Isooctane heat of adsorption over HY and 1.0LaY at varying isooctane coverage. Adsorption conditions: 300 mg, 100 °C. 77

Figure 28. A) Isooctane cracking TOF, methane selectivity, and butane selectivity over 10mg of various La loading. B) Isooctane cracking TOF, methane selectivity, and butane selectivity over 25mg of various La loading. C) Isooctane cracking TOF comparing 10mg and 25mg loading of the various samples. D) Methane and butane product selectivity over 10mg and 25mg loading of the various samples. 78

Figure 29. Simulated isooctane conversion and isooctane TOF as a function of catalyst mass using series of reaction equations from **Table 9**. A) Isooctane conversion versus catalyst mass by changing k_{HT}. B) Isooctane TOF versus catalyst mass by changing k_{HT}. C) Isooctane conversion versus catalyst mass by changing k_{PC}. D) Isooctane TOF versus catalyst mass by changing k_{PC}.81

Figure 30. Isooctane conversion as a function of catalyst mass for HY and 1.0LaY. Solid lines represent the model using the reaction constants from **Table 10**. Reaction conditions: continuous flow reactor at 2.4 kPa of isooctane partial pressure, 80 mL/min of carrier gas flow, 400ºC, 1 atm..... 82

Figure 31. A) Isooctane cracking over various zeolite samples at isooconversion B) Reaction pathway distribution. Reaction conditions: Reaction conditions: 400 C, 10-25mg cat, 1.7 kPa, continuous flow mode. Error bars reflect the deviation in activity over 220 min t.o.s..... 84

Figure 32. Apparent activation energy for A) protolytic cracking pathway and B) hydrogen transfer pathway for HY and LaY samples. PC reaction conditions: Pulse mode. 5 mg catalyst. 0.56 kPa. 100 mL/min N2 carrier flow. 400-430 ºC.HT reaction conditions: Continuous flow mode. 5-12 mg catalyst. 1.11 kPa. 100 mL/min N2 carrier flow. 160-180 ºC..... 84

Figure 33. Ratio of TOF of isooctane cracking over 25mg and 10mg catalyst loading as a function of Bronsted acid density. 88

Figure 34. Visual representation of mass x time method in comparing deactivation between catalysts in a batch reactor. 100

Figure 35. A) XRD spectra of H-MOR and La-MOR samples, B) XRD spectra of H-MOR and La-MOR samples at 2θ=18º-22º 103

Figure 36. NH3-TPD curves of H-MOR, La-MOR 0.04M, La-MOR 1.0M, and La-MOR 2.0M 105

Figure 37. A) FTIR spectra of H-MOR and La-MOR samples, B) Area distribution of 8-MR and 12-MR Bronsted acid sites from the deconvolution of 3600 cm^{-1} peak..... 106

Figure 38. 3600 cm^{-1} peak deconvolution into 3592 cm^{-1} and 3611 cm^{-1} of A) H-MOR, B) La-MOR 0.1M, C) La-MOR 0.5M, La-MOR 1.0M 107

Figure 39. Reaction pathways in the alkylation reaction between toluene and isopropanol. 108

Figure 40. A) Alkylation product distribution for MOR catalysts at different La loading. Reaction conditions: 20 mins, 50 mL volume, 100 mg-cat, 0.5M isopropanol 1.0M toluene; B) ratio of para and orto-selectivity at varying toluene conversion in liquid phase. 109

Figure 41. A) Liquid phase alkylation reaction. Concentration of alkylated products as a function of mass-cat x time for two different masses: 50 mg and 100 mg over H-MOR, La-MOR 1.0M, and La-MOR 2.0M. Reaction conditions: 220 ºC, 1.0M toluene and 2.0M isopropanol in cyclohexane, 50 mL total volume. B) Gas phase, continous flow alkylation reaction. Experimental data and deactivation model curve of toluene conversion as a function of time on stream. Reaction conditions: 5:1 mol toluene: isopropanol reactant mixture, 0.2 mL/hr reactant mixture injection rate, 220 C, 100 mL/min He, 1 atm, 200 mg catalyst..... 110

Figure 42. Changing toluene: isopropanol ratio to increase the degree of oligomerizations. Reaction conditions: 0.15 mL/hr reactant mixture injection rate, 220℃, 100 mL/min He, 100 mg cat, 1 atm..... 111

Figure 43. TGA curve of the spent catalyst from gas-phase reaction. Reaction conditions: 5:1 mol toluene: isopropanol reactant mixture, 0.2 mL/hr reactant mixture injection rate, 220℃, 300 min t.o.s., 100 mL/min He, 1 atm, 200 mg catalyst..... 112

Figure 44. TGA curve of the spent catalyst of H-MOR from liquid-phase batch reaction at varying reaction time. Reaction conditions: 1.0M toluene, 1.0M isopropanol in cyclohexane, 50 mL, 300 rpm, 220℃, 300 psig, 100 mg catalyst. 113

Figure 45. Deconvolution of the MS signals from evolved CO2 (m/z = 44) and H2O (m/z = 18) during the coke burning process of the spent catalysts from the gas-phase reaction. 115

Figure 46. A) ^{13}C MAS-NMR of spent catalysts of H-MOR and La-MOR 1.0M in liquid phase; B) and C) the difference between the spectra. Reaction conditions: 20 mins, 50 mL volume, 100 mg-cat, 2.0M isopropanol, 1.0M toluene. 116

Figure 47. Isooctane cracking reaction A) Ternary plot of reaction pathways, B) Turnover frequency of reaction pathways. Reaction conditions: Approximately 10% isooctane conversion, 2.74 kPa isooctane partial pressure, continuous flow mode, 400°C, 80 mL/min N_2 carrier. Pretreatment: 0.5°C/min to 300°C and hold 1 h. Heat to 400°C at 2°C/min. 116

Figure 48. Alkylation reaction of H-MOR, La-MOR 1.0M and Na-MOR. Reaction conditions: 5:1 toluene to isopropanol. 0.2 mL/hr reactant mixture injection rate, 150 °C, 100 mL/min He, 1 atm, 200 mg catalyst A) toluene conversion as a function of time on stream. B) Para- to ortho-cymene ratio as a function of time on stream. 117

Figure 49. A) Lanthanum role in improving shape selectivity via pore constriction. B) Lanthanum role in improving catalyst stability by increasing the hydrogen transfer rate resulting in a lower carbenium ion lifetime on the surface. 118

List of Schemes

Scheme 1.Structure of Bronsted acid and the formation of Lewis acid via framework dealumination..... 4

Scheme 2.Reaction pathways during alkylation between toluene and propylene over Bronsted acid..... 11

Scheme 3. Reaction pathway of cyclohexene over FCC catalysts using an overall lumped kinetic model. Retrieved from [65]..... 14

Scheme 4.Simplified reaction network of alkylation reaction between isobutane and 2-butene. Retrieved from [70]..... 15

Scheme 5. Isooctane cracking over acid sites through protolytic cracking pathway via iC8 carbonium ion formation..... 27

Scheme 6. Isooctane cracking over acid sites through hydrogen transfer pathway and dehydrogenation pathway via iC8 carbenium ion formation..... 28

Abstract

The incorporation of metal additives into zeolites has allowed a much higher degree of zeolite tunability, including altering the original active sites, introducing new active sites, modifying pore structures, and introducing bifunctional properties. As a result, these modifications have a profound impact on the catalyst performance, altering product selectivity, catalyst activity, and catalyst stability. This thesis investigates the role of several metal additives, including sodium, calcium, cobalt and lanthanum, focusing on their impact during isooctane cracking and aromatic alkylation reaction between toluene and isopropanol.

The first part of this thesis explores isooctane cracking over faujasite zeolite as probe enabling the quantification of protolytic cracking, dehydrogenation, and hydrogen transfer pathway. The development of this probe was possible by the addition of metal cations such as Na, Ca, Co as additives to modify the rates of these reaction pathways. This has enabled a quantitative assessment of cation titration at not only promoting new pathways, but selectively titrating sites that are most active for protolytic cracking. We further contrast this simple approach in ternary diagrams that visually depict the contributions of catalyst modifications and reaction conditions on the three parallel reactions, revealing that Na selectively titrates sites responsible for protolytic cracking while Co promotes dehydrogenation reactions. Finally, we reveal that the incorporation of La, often added to Y zeolites in industrial catalytic cracking operations, enhances both hydrogen transfer rates and dehydrogenation rate of alkanes.

The second and third part of the thesis primarily focuses on La as an additive. The second part is a continuation of La modified Y zeolite from the first part. This section focuses the impact of La introduction as an additive via ion exchange on the physical and chemical properties of low Si/Al Y zeolite, including the preservation of zeolitic structural integrity and acid sites

modifications. The addition of La has a pronounced effect on the isooctane cracking performance of zeolite Y, altering the reaction pathway selectivity and cracking activity.

Finally, the final part of the thesis investigates the effects of La incorporation in H-MOR via wetness impregnation and focuses on the impact of La on shape selectivity and catalysts' stability against coking during the alkylation between toluene and isopropanol. The addition of La alters the pore size of the MOR zeolite via pore constriction. Furthermore, La also enhances the hydrogen transfer activity between carbenium ion and coke deposited. This modification leads to improved product selectivity and catalyst stability, highlighting the potential of La-modified zeolites in enhancing catalytic performance.

Collectively, these findings deepen our understanding of the role of these additives in zeolite catalysis, offering insights for optimizing catalyst synthesis for hydrocarbon reactions.

Chapter 1

General Introduction

1.1 Crude Oil and Petrochemical industries

Crude oil refineries have been the forefront of energy sources and chemical feedstocks over the last century. The demand of crude oil has seen a rapid increase in the past few decades, due to the increasing demand in energy consumption [1, 2]. Crude oil refineries primarily produce transportation fuels and industrial usage such as gasoline, diesel, kerosene, heavy oils, asphalt, and naphtha, which can be utilized directly [3, 4]. Additionally, they yield various simpler chemicals like propylene, butene, ethene, and BTX (benzene, toluene, xylene), serving as essential building blocks for the production of a wide range of valuable chemicals and products [5, 6]. The consumption of energy will continue to increase, and many efforts have been made to diversify the energy source including biofuel and hydrogen fuel. Despite that, crude oil is still the biggest industry for energy source due to the high degree of maturity in scale and technology. Furthermore, recent advances in hydraulic fracturing (fracking) and CO_2 reduction technology will contribute to a heightened demand of the crude oil refineries [7-9]. Hence, the immediate challenges involve discovering more efficient methods for converting crude oil into consumer-ready products. This includes optimizing reaction conditions and catalysts within the diverse catalytic units in refineries. The catalysts employed in petrochemical industries are demonstrated to possess high levels of activity, selectivity, durability, and stability, establishing them as crucial components. Continuously striving to enhance these attributes remains the primary objective, addressing the evolving challenges associated with the escalating demand for consumer ready products.

1.3 Zeolites

Zeolite is a well-defined crystalline aluminosilicate, with three-dimensional structures containing pores, channels, and cavities at a molecular scale [10, 11]. These structures are possible by using SiO_4 and AlO_4^- tetrahedra as building blocks, which are connected by oxygen atoms at each corner. Due to the charge difference between SiO_4 and AlO_4^-, the negative charge is compensated with a cation, including Na^+, NH_4^+, H^+, and others. Naturally, zeolites are found in abundance around areas that are high in volcanic activity, but they can also be synthetically synthesized. There are more than 200 zeolite structures that have been reported, and each structure holds unique physical and chemical properties that can be used and utilized, depending on the applications[12, 13].

Due to these unique physical and chemical properties, they are widely used in chemical industries in catalysis, adsorption, separation, and ion exchange [11, 13, 14]. In refining industries, fluid catalytic cracking (FCC) and hydrocracking are the leading users of zeolites for catalytic applications. Furthermore, recent advancement in methanol-to-hydrocarbon (MTH) and biomass conversions over zeolite catalysts have been shown to be an appealing route in producing gasoline, aromatics, and olefins [13]. Aside from refineries, zeolites have also been used extensively in transforming basic, building block chemicals into larger, more valuable ones. For instance, Friedel-Crafts acylation and alkylation reactions have been used extensively over zeolite catalysts. These reactions have been directly involved in synthetic organic chemistry production, contributing to various industries including pharmaceuticals, fragrance, dye, and agrochemical industries [15]. Therefore, the usage and demands of utilizing zeolites for commercial applications will only continue to rise, and it is important to further research and develop innovative methods to enhance their synthesis, characterization, and application in various industries.

1.3.2 Properties of Zeolites

Corma highlighted some of the characteristics of zeolites as to why the usage of zeolites are a huge success in chemical industries as solid catalysts [16]. These characteristics include: 1) High surface area and adsorption capacity. 2) Controllable adsorption properties. 3) Tunable active sites. 4) The sizes of the channels are a typical range for many molecules of interest. 6) Channels structures that allow shape selectivity. 6) High stability against harsh thermochemical conditions. These characteristics are often associated with great catalysts, as they enable us to fulfill the demands of performing a specific reaction with a high degree of controllability.

The most important aspect of zeolites is their acid sites, which has been largely attributed to their success in heterogenous catalysis. As previously mentioned, due to the charge difference between SiO_4 and AlO_4^-, the negative charge is compensated with a cation, including Na^+, NH_4^+, H^+, and others. The H^+ within the zeolite is associated with the Bronsted acid site, which is the primary active site that is responsible for catalyzing most of zeolite reactions. The Bronsted acid site is also known as the bridging Si-OH-Al group. Lewis acid sites are also present within the zeolites, and this is attributed to the uncoordinated Al center of the zeolite framework, which can be formed via framework dealumination [17]. **Scheme 1** shows the relationship between Bronsted acid and Lewis acid within zeolites. The appealing properties of using zeolite as an acid catalyst is the tunability of the acid properties, both in acid density and acid strength.

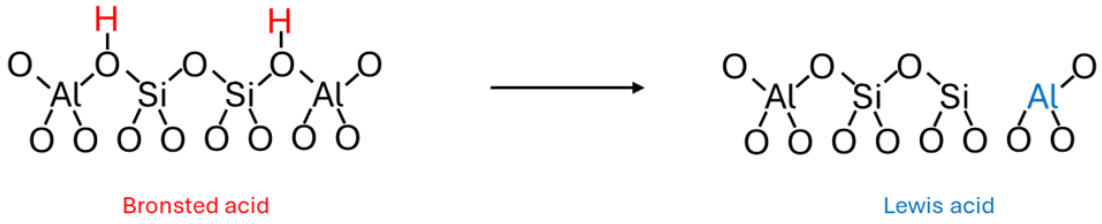

Scheme 1.Structure of Bronsted acid and the formation of Lewis acid via framework dealumination

1.4 Metal additives in zeolites

One of the methods in altering the physical and chemical properties of zeolites is by introducing metal additives. These additives include alkali metals (Na, K, Rb, Cs), early transition metals (Cu, Fe, Ni), noble metals (Pt, Pd, Rh, Ru, Ir), and rare-earth metals (La, Ce). These additives allow a much higher degree of zeolite tunability, including altering the original active sites, introducing new active sites, modifying pore structures, and introducing bifunctional properties. These metals are introduced in various ways, including metal framework substitution, metal ion-exchange, and metal clusters. A review work by Zhang and coworkers summarizes the synthesis strategies of incorporating various metals into zeolites and their catalytic applications for various reactions [18].

1.4.2 Addition of sodium (Na) and calcium (Ca) as Bronsted acid titrant

Introduction of Na and Ca into acidic zeolites via ion exchange has been a well-established method in titrating Bronsted acid sites [19-21]. The positive charge of Na and Ca are introduced into the zeolites structure as the charge balance species, resulting in the reduction of available Bronsted sites for reaction. Hence, the introduction of Na and Ca via ion exchange allows the tunability of the Bronsted acid density, without altering the structure of the zeolite framework. Furthermore, due to 2+ charge of the Ca ion, framework paired Bronsted acid sites can be exclusively titrated. These paired sites are categorized as part of the synergistic sites within the zeolites [22-25]. The roles of these sites have garnered attention in zeolite catalysis works.

1.4.3 Usage of Lanthanum as additive

The introduction of rare earth (RE) metals such as Lanthanum (La) into zeolite Y via ion exchange is one of the most important additives in preparing FCC catalysts, as it has been attributed to improving thermal stability, selectivity and activity of the catalysts [26-28]. During the ion exchange, the La species is introduced into the zeolite framework by exchanging the

Bronsted acid sites via hydrolysis [29-32]. The exact roles of La in improving the performance of Y zeolites in FCC processes have been thoroughly debated in the literature, including enhancing zeolite framework stability against hydrothermal conditions, altering the acid properties of the zeolites, changing the size of the crystal lattice, as well as improving the intrinsic catalyst activity.

1.5 Hydrocarbon reactions over acidic zeolites

1.5.1 Alkane cracking and activation over Bronsted acid

As previously mentioned, most of the feeds entering the FCC unit consist of a long chain of hydrocarbons, including alkanes and alkenes. This section will discuss the activation mechanisms of these molecules over Bronsted acid sites within zeolites, leading to C-C cleavage and the formation of smaller, desired products.

1.5.1.1 Monomolecular cracking mechanism – Carbonium ion transition state

Monomolecular alkane cracking mechanism involves the formation of a penta-coordinated carbonium ion transition state, resulted from the protonation of the alkane by a strong Bronsted acid site [33, 34]. As a result, the carbonium ion transition state species collapse into: an alkane or dihydrogen and an adsorbed carbenium ion (alkoxide) [33]. In the case of n-butane cracking, the possible products pairs are dihydrogen and butene carbenium ion (butoxide); ethane and ethyl carbenium ion (ethoxide); and methane and propyl carbenium ion (propoxide). The fate of the carbenium ion/alkoxide formed from the reaction can either proceed subsequent reaction involving carbenium ion chemistry, or leave the original Bronsted acid site forming an alkene. The pathway that resulted in smaller alkane and carbenium ion transition state is called the protolytic cracking pathway, while the pathway that produces dihydrogen and the carbenium ion transition state is known as the dehydrogenation pathway.

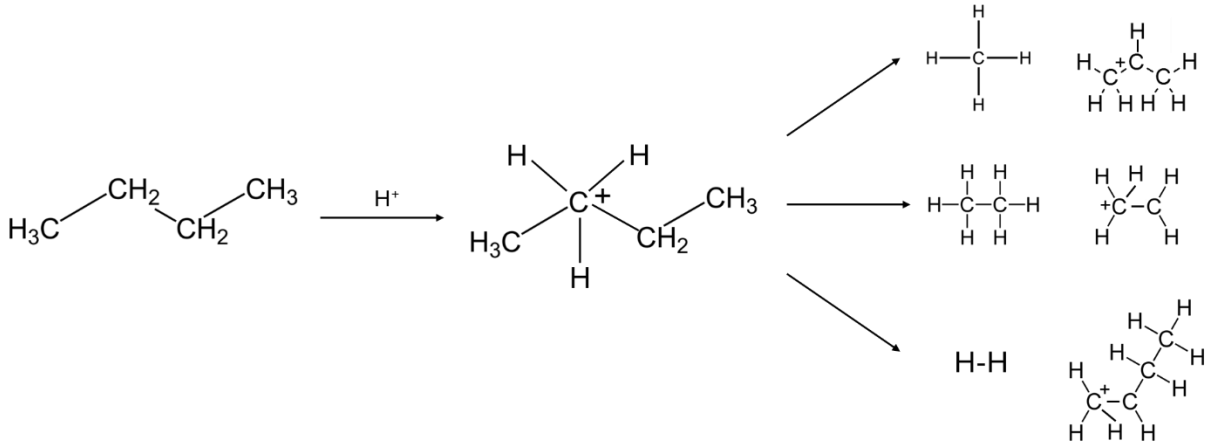

Figure 1. Protolytic cracking of n-butane and possible products. A) Methane and propyl carbenium ion B) Ethane and ethyl carbenium ion. C) Dihydrogen and butyl carbenium ion.

Monomolecular, carbonium ion cracking pathway is often favored under the following reaction conditions:

1) High reaction temperature: Protolytic cracking is often associated with high activation energy barrier, relative to β-scission and carbenium ion chemistry [35, 36]. The activation energy also depends on the alkane chain length and branching, as the stability of the transition state depends on these two characteristics [37]. A typical protolytic cracking temperature range for linear small alkanes is around 623K and above [33].

2) Low alkane partial pressure: Protolytic cracking is a monomolecular mechanism, requiring minimal gas phase reactant partial pressure that minimize the shift of the reaction mechanism to a bimolecular mechanism (**Section 1.5.1.2**).

3) Low alkane conversion: Protolytic cracking involved the initial activation of the alkane with an empty Bronsted acid site. Ensuring the surface coverage is minimal with the cracking products can minimize subsequent and chain reactions, which is key to carbenium ion chemistry. A typical

conversion range to maximize protolytic cracking has been shown to be around 2% or lower, depending on the alkane and zeolites structures [38].

1.5.1.2 Bimolecular Cracking mechanism via Hydrogen transfer – Carbenium ion formation and β-scission

Another parallel, competing mechanism in alkane cracking is the hydrogen transfer pathway, a process of the gas phase alkane donates a hydrogen (hydride) to the surface alkoxide species, resulting the gas phase alkane forming a carbenium ion transition state species, while an alkane is formed from the initial surface species receiving the hydride [35]. This process is also known as the bimolecular cracking mechanism, involving the gas phase reactant and the surface species, originate from the products of the previous catalytic cycle. Once the carbenium ion is formed, the C-C bond breaking step occurs, involving the carbon pairs neighboring the positively charged carbon. This process is known as the β-scission step, leading to the fragmentation of the initial carbenium ion transition state species forming a smaller alkene and a smaller alkyl carbenium ion. **Figure 2** shows the cracking of isooctane via hydrogen transfer mechanism with the surface isobutyl carbenium ion transition state species, forming the isoctyl carbenium ion species, and the subsequent β-scission products.

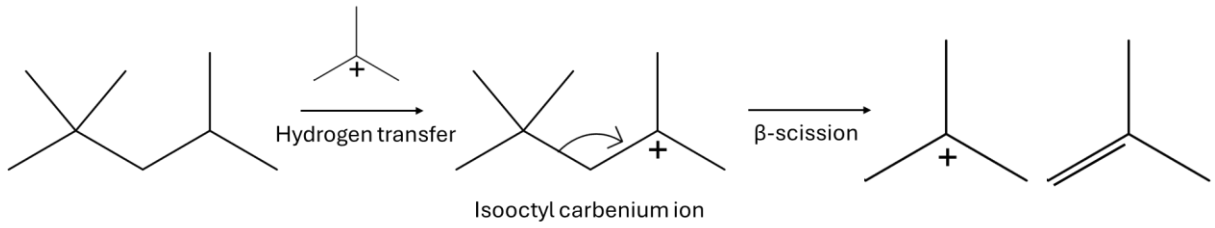

Figure 2. Bimolecular cracking mechanism of isooctane via hydrogen transfer and β-scission.

Depending on the rate limiting step, the rate of bimolecular cracking mechanism depends on either the hydrogen transfer step or the β-scission step. In the case of hydrogen transfer, the rate is

dependent on the hydride donor (gas phase alkane) and the hydride acceptor (surface alkoxide). Mullen and Janik investigated the energetics of hydride transfer process of various hydride donor and hydrogen transfer over MOR zeolite via DFT, and they found that alkane with ternary carbon makes a great hydride donor when compared to secondary and primary alkane, while alkoxide with ternary carbon makes a great hydride acceptor when compared to secondary and primary alkoxide [39]. In the case of β-scission as the rate limiting, similarly, the relative rate of the β-scission step will depend on the nature of the alkyl carbenium ion. These conditions will dictate whether the carbenium ion directly undergoes β-scission, or first goes through isomerization step before the β-scission. Weitkamp and coworkers noted that the rate of β-scission depends on the skeletal structure initial carbenium ion, as well as the structure of resulted carbenium ion after the C-C cleavage (**Figure 3**) [40, 41].

The reaction conditions that favor bimolecular cracking mechanism include:

1) Mild reaction temperature: Relative to monomolecular, carbonium ion pathway, hydrogen transfer process has a much lower activation energy barrier [42]. Thus, by working under a milder reaction condition, carbonium ion pathway can be minimized. Furthermore, the equilibrium constant of surface alkoxide and the desorbed alkene from the cracking products can be higher, resulting in a higher coverage of the surface alkoxide at lower temperature.

2) High alkane partial pressure: Since hydrogen transfer is a bimolecular reaction, high reactant partial pressure will favor hydrogen transfer pathway.

3) High reactant conversion: By operating at a high alkane conversion, the concentration of the alkoxide surface species that act as a hydride acceptor will be higher. As a result, hydrogen transfer pathway is favored at high conversion. Furthermore, by increasing the surface coverage with the

alkoxide, this will result in a lower concentration of available Bronsted acid sites that are available for a monomolecular cracking reaction.

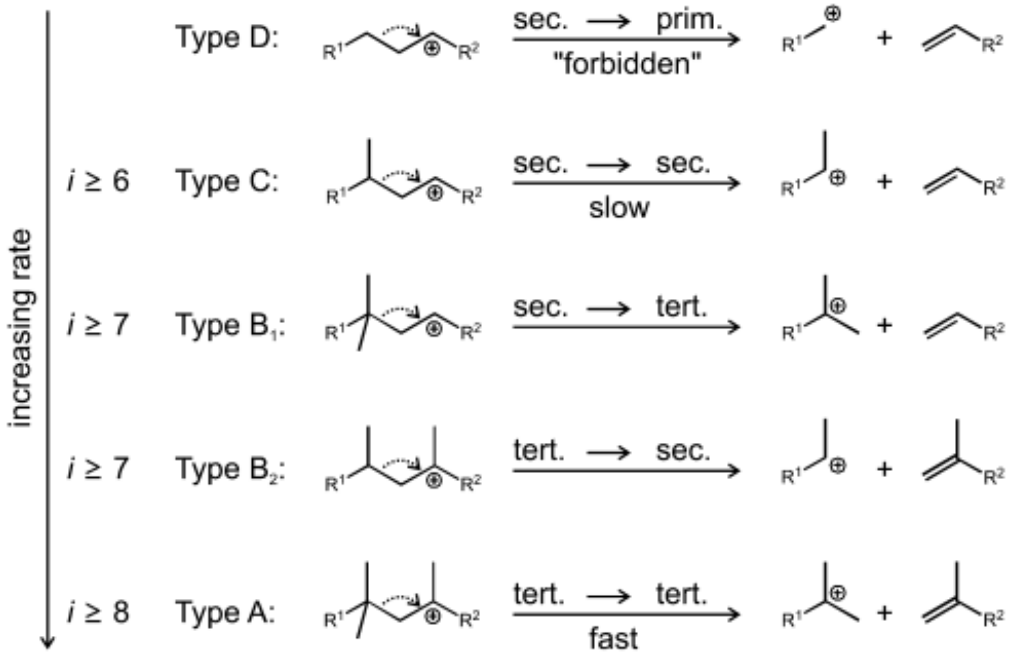

Figure 3. Classification of β-scission step of alkylcarbenium ion. Retrieved from [41]

1.5.2 Aromatic Alkylation Reaction

Aromatic alkylation reaction is the process of converting aromatic and olefin feeds into a bigger compound via C-C coupling. Alkylation of aromatics with an alkylating agent is the most common alkylation process in petrochemical industries. Examples of aromatics include benzene, toluene, and xylene (BTX), while olefins and short alcohols are examples of alkylating agents. Alkylated intermediates, such as ethylbenzene (EB), cumene, para-diethylbenzene (para-DEB), para-and meta-diisopropylbenzene (para-and meta-DIPB), linear alkylbenzenes (LAB), para-ethyltoluene, and para-and meta-cymene, are then used to produce other valuable products such as polymers, paints, detergents, medicines, agricultural products, and explosives [43, 44].

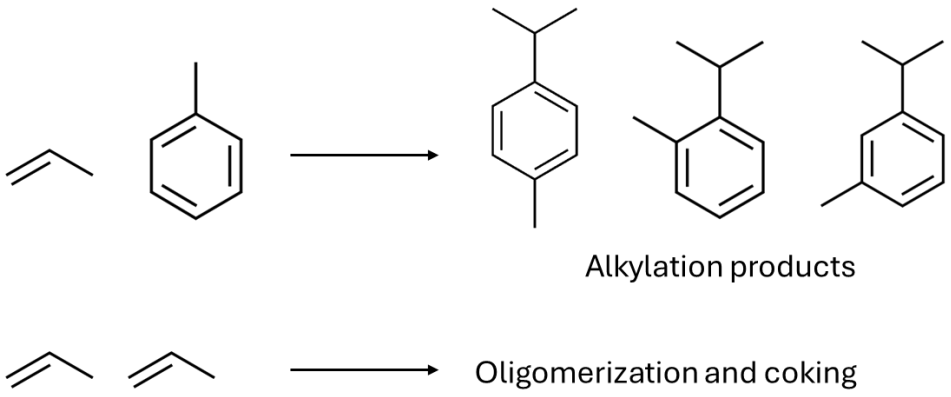

Scheme 2.Reaction pathways during alkylation between toluene and propylene over Bronsted acid

Scheme 2 shows an example of alkylation reaction between toluene and propylene. Alkylation reaction requires a Bronsted acid site. Often, the alkylate will form a carbenium ion transition state species with the Bronsted acid site, allowing the formation of the C-C bond between the aromatic compound and the alkylate. The exact reaction mechanism of aromatic alkylation reaction remained controversial, as the rate limiting step is often associated with the reaction conditions as well as the characteristics of the acid catalysts [45]. Microporous structure of the zeolites allows shape selectivity during aromatic alkylation processes, as the demand for the isomers of the

alkylated products are varied. A competing reaction is also present during this reaction, where the carbenium ion from the alkylate can dimerize with itself, leading to oligomerization and coke formation [46-48].

1.6 Importance of Hydrogen Transfer in chemical processes

Hydrogen transfer reaction serves as one of the most important reactions in chemical processes, as it influences product selectivity and catalyst stability. In the context of FCC processes, hydrogen transfer plays a crucial role in altering the products' octane number. For example, hydrogen transfer process is directly responsible in converting olefins and naphthenes to paraffins and aromatics. [49, 50]. Furthermore, a higher hydrogen transfer rate prevents further cracking by minimizing the carbenium ion lifetime [49]. As a result, the final products have higher selectivity toward the gasoline-range hydrocarbon, while lowering light gases products. However, a high hydrogen transfer rate may not be desirable for product selectivity. Even though the formation of aromatics is beneficial in octane enhancement, the loss in olefins and naphthene, as well as the formation of paraffins resulted in a net loss in octane number. Moreover, it also reduces light olefins yield, which are crucial chemical feed for other processes such as alkylation and polymerizations [49].

In the case of catalyst deactivation, high hydrogen transfer rate reduces the amount of coke production by limiting the carbenium ion lifetime that is susceptible to oligomerization reactions, the main source of coke. However, high rate of hydrogen transfer can also increase aromaticity of the products, which are susceptible to form coke [51, 52]. It is also important to recognize that coke formation in FCC and chemical processes is not strictly unwanted, as it is important as a source of hydride for hydrogen in limiting carbenium ion lifetime[49, 53], as well as a source of energy for the FCC unit since coke combustion is an exothermic process [51, 54, 55]. Hence, when

selecting a catalyst for FCC processes, it is crucial to understand its ability to perform hydrogen transfer reactions. This understanding is essential for achieving the desired balance between product selectivity and catalyst stability.

In the context of aromatic alkylation reactions over acidic zeolites, the catalyst's hydrogen transfer activity is important in maintaining its stability. To maintain catalyst stability, it is essential to minimize the lifetime of the carbenium ion, which reduces the rate of oligomerization. The reduction in oligomerization rate is pivotal as it is the primary cause of catalyst coking and deactivation.

1.7 Hydrogen transfer reaction probes

The previous section discusses the importance of hydrogen transfer reaction in FCC processes, and it is at utmost importance in selecting the right catalyst. In literature, there are several indexes and probe reactions that have been proposed as a fingerprint to measure the catalyst ability in performing hydrogen transfer reaction.

1.7.1 Alkane to alkene ratio of the product stream during alkane cracking

Traditionally, the product alkane to alkene ratio has been used as an indicator of hydrogen transfer activity of a given catalyst during cracking reactions [56-58]. This concept was developed based on the fate of the surface intermediates that react from their carboxide resting state via a carbenium ion transition state. They can either desorb as an alkene or accept a hydride from a hydride donor and leave the surface as an alkane. By comparing the alkane/alkene ratio obtained from different catalysts at given reaction conditions and conversion levels, the catalyst’s ability to perform hydrogen transfer during alkane cracking can be inferred [59-64].

1.7.2 Cyclohexene

De la Puenete and Sedran proposed the usage of cyclohexene as a test reactant to evaluate hydrogen transfer reaction in several FCC catalysts [65]. Using a batch fluidized-bed reactor under a very short contact times at 300C, the relative rate of the products evolved from cyclohexene feed can describe a hydrogen transfer index of the catalyst. **Scheme 3** shows the reaction scheme for cyclohexene using overall lumped kinetic model.

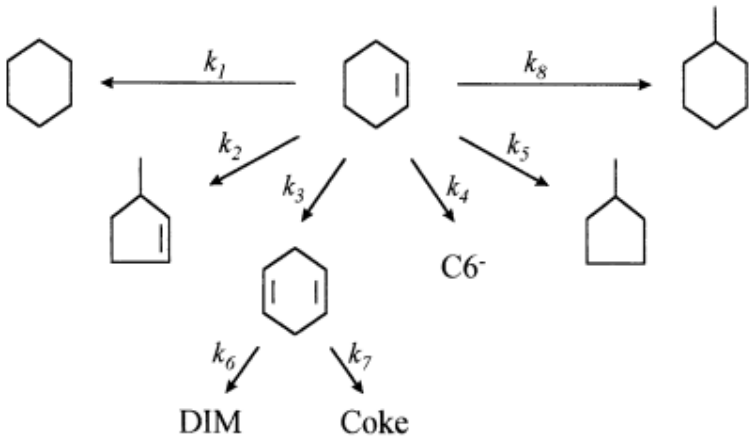

Scheme 3. Reaction pathway of cyclohexene over FCC catalysts using an overall lumped kinetic model. Retrieved from [65].

. The key product that reflects the hydrogen transfer process is the formation of methyl cyclopentane, since this product is formed based on the fate of the methylcyclopentyl carbenium ion receiving hydride from the gas phase cyclohexene. The group proposes the following equation as hydrogen transfer index:

$$i_{HT} = \frac{k_5}{k_2 + k_4 + k_5}$$

1.7.3 Isobutane/butene alkylation reaction

Alkylation reaction between isobutane with butene is one of the most important reactions in the refining industries, as this reaction is the main way in producing highly branched C_8 alkanes,

which are key chemicals in producing high-octane fuels. Lercher's group have extensively investigated the alkylation reaction between isobutane and butene over various acidic zeolites [66-70]. **Scheme 4** shows the reaction network in isobutane/2-butene alkylation reaction. First, butene is adsorbed on the surface to form a butyl alkoxide, which can dimerize to form a C_8 alkoxide. Then, there are two competing pathways in isobutane/butene alkylation. The first pathway is the hydrogen transfer pathway, where the gas phase isobutane acts as a hydride donor to the surface alkoxide, forming an isobutyl alkoxide and an alkane product. Hence, alkane C_8 isomers can be used as a fingerprint of a hydrogen transfer product. Furthermore, the competing reaction is the further oligomerization of the surface alkoxide, resulting from a longer carbenium ion lifetime due to the lack of hydrogen transfer process. As a result, the higher oligomerization rate will result in coke formation and reduces the catalyst lifetime. Therefore, by measuring the relative rate of C_8 alkane isomers, as well as the relative stability of the catalyst against coke formation can indicate the relative hydrogen transfer rate of different catalysts.

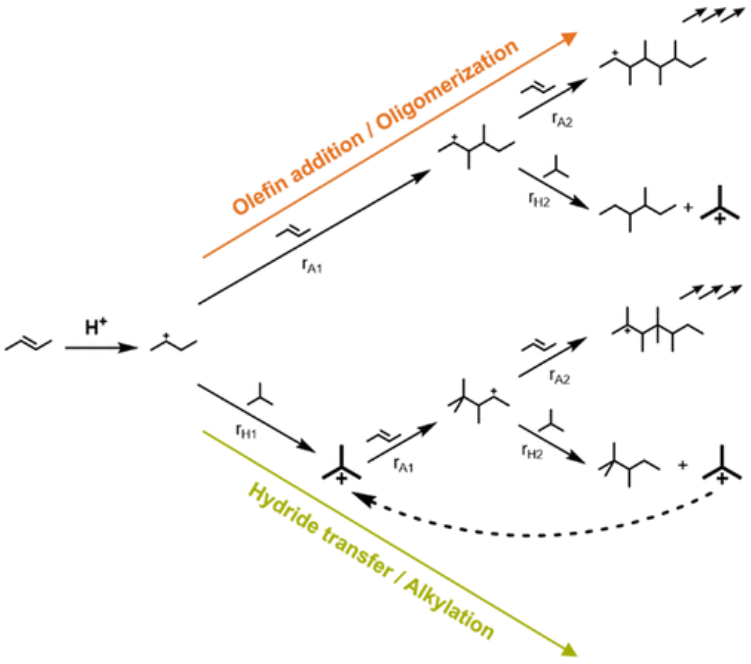

Scheme 4.Simplified reaction network of alkylation reaction between isobutane and 2-butene. Retrieved from [70]

1.8 Scope of thesis

The goal of this thesis will focus on additives incorporation into acidic zeolites and investigate their effect on hydrocarbons reactions such as alkane cracking and aromatic alkylation reaction. The goal is to explore how these additives alter the reaction pathways during these processes, particularly related to hydrogen transfer pathway.

In chapter two, this thesis discusses isooctane cracking as a reaction probe to investigate hydrogen transfer reaction in faujasite zeolites. Due to isooctane unique property, isooctane cracking allows for appreciable protolytic cracking and hydrogen transfer reaction rates under modest reaction conditions where zeolite structural integrity is preserved. The incorporation of additives such as Na, Ca, Co, and La appear to alter the reaction pathways, and the roles of these additives in altering zeolite activity and selectivity during isooctane cracking will be discussed.

Chapter three is a continuation of chapter two, where La as an additive will be a major interest. In this chapter, this work explores the characterization of La incorporated Y zeolites at various La loadings. These characterizations techniques shed some lights into the impact of La in modifying physical and chemical properties of the zeolites, how on these properties resulted in altering the zeolite performance during isooctane cracking, particularly with the enhancement of hydrogen transfer pathway.

Finally, the theme of La as additive in zeolite continues in chapter four, where La is incorporated in H-MOR zeolite to improve the shape selectivity and catalyst stability against coke formation during the alkylation of toluene with isopropanol.

Chapter 2

Investigating the interplay of hydrogen transfer, protolytic cracking, and dehydrogenation reactions over faujasite zeolites by using isooctane conversion as a probe

Isooctane can serve as a useful probe to investigate hydrogen transfer reactions in faujasite zeolites. Its unique nature, containing both quaternary and ternary carbons, allows for appreciable protolytic cracking and hydrogen transfer reaction rates under modest reaction conditions where zeolite structural integrity is preserved. We show how a simple plot of C4 alkane selectivity vs. C1 selectivity allows for visible quantification among the tradeoffs between protolytic cracking and hydrogen transfer pathways. Similarly, we illustrate how deviations from a linear relationship between these two products can be used to quantify dehydrogenation rates. The role of metal cations such as Na, Ca, and Co as titrants was explored to modify the rates of these reaction pathways, enabling quantitative assessment of cation titration at not only promoting new pathways, but selectively titrating sites that are most active for protolytic cracking. We further contrast this simple approach in ternary diagrams that visually depict the contributions of catalyst modifications and reaction conditions on the three parallel reactions, revealing that Na selectively titrates sites responsible for protolytic cracking while Co promotes dehydrogenation reactions. Finally, we reveal that the incorporation of Lanthanum, often added to Y zeolites in industrial catalytic cracking operations, enhances both hydrogen transfer rates and dehydrogenation rate of alkanes. This comprehensive approach improves our understanding of catalyst performance and reaction mechanisms while offering insight for practical applications.

This work is a submitted manuscript

2.1 Introduction

Acidic zeolites play a crucial role in various refining applications, offering highly tunable and controllable properties that enhance catalyst design for specific reactions. [10] Alkane cracking over acidic zeolites is a process of great industrial importance as this converts heavy hydrocarbons into more valuable transportation fuels and valuable olefins [10, 53, 71, 72]. More recently, these zeolites have been shown to have promising performance in the emerging application area of waste polymer conversion to produce fuels and valuable olefins [73-76]. Therefore, the interest in cracking reactions over acidic zeolites is anticipated to continue to rise, and it is of utmost importance that these processes are well understood in order to contribute to the broader goals of refining and plastic waste management.

Many previous studies have established the role of monomolecular and bimolecular mechanisms of alkane cracking over Bronsted acid sites. Monomolecular mechanisms involve the formation of a penta-coordinated carbonium ion transition state via the protonation of an alkane molecule by the Bronsted acid site [33, 77]. Next, the C-C bond is cleaved, producing a smaller alkane, and a protonated, smaller alkene (surface alkoxide). This pathway is often referred to as the protolytic cracking pathway. A competing mechanism is the bimolecular mechanism, where a hydrogen transfer process occurs between the gas phase alkane (reactant) and a surface alkoxide (via a carbenium ion). The gas phase alkane will then form a second carbenium ion transition state, which undergoes rearrangement (isomerization) and/or β-scission, producing two smaller cracking products: a gas phase alkene and a surface alkoxide [78-81]. The conditions required to perform the two pathways have been linked to the reaction conditions, including temperature, the level of reactant conversion, and partial pressure [42, 77]. Protolytic cracking (monomolecular) typically exhibits higher activation energy barrier when compared with hydrogen transfer (bimolecular)

processes [42], leading to large differences in overall reaction rates depending on the reaction conditions that favor the bimolecular pathway to different extents. Often, this stark difference in barrier makes it challenging to contrast the two pathways under similar reaction conditions.

2,2,4-trimethylpentane, or isooctane, is a unique molecule that contains both quaternary and ternary carbon atoms. This unique feature has not been fully explored in the literature. The presence of quaternary carbons allows competing reaction mechanisms to occur under modest reaction conditions due to a much lower barrier for the quaternary carbon to go through the protolytic cracking pathway. This rate enhancement can be ascribed to the higher polarizability of the quaternary carbon, resulting from the presence of the three neighboring methyl groups, which leads to a more stable carbonium ion transition state [82]. Some previous studies have explored isooctane cracking over acidic zeolites, including the role of topology and acid properties [82-85]. However, the interplay between protolytic cracking (PC), hydrogen transfer (HT), and dehydrogenation (DH) at various reaction condition on the resulted products selectivity has not been previously investigated. Likewise, previous studies have not analyzed the effects of titrating Bronsted acid sites with metal cations (Na ,Ca, Co, La) on these competing reaction pathways. The present work analyzes the main reaction mechanisms involved in isooctane cracking over Bronsted acid sites (BAS), under reaction conditions that allow appreciable rates of protolytic cracking and hydrogen transfer. The role of titrating the Bronsted acid sites with metal cations, such as Na and Ca on the relative rates of PC and HT are also examined. This detailed study is contrasted with the typical alkane/alkene ratio which is often used as a fingerprint for hydride transfer over industrial catalysts. We reveal how often a selective titration of sites that promote protolytic cracking may be interpreted as an enhanced ability of a catalyst to promote hydride transfer, even when comparing at isoconversion, when employing such metrics. These results are further presented in

ternary plots that contrast rates of protolytic cracking, hydrogen transfer, and dehydrogenation to further clarify the ability of isooctane to delineate these trends, while illustrating the dual role of Lanthanum incorporation on the manipulation of hydride transfer and dehydrogenation rates.

2.2 Materials and Methodologies

2.2.1 Materials

The parent faujasite zeolite Y with Si/Al=15 (CBV 720) was obtained from Zeolyst International in the proton form. 2,2,4-trimethylpentane (>99.5), 2-methylhexane (>99%), 2,5-dimethylhexane (>99%), isobutane (>99%), sodium nitrate (>99%), calcium nitrate tetrahydrate (>99%), and cobalt (II) nitrate (>98%) were obtained from Sigma-Aldrich; they were used directly without further purification. The parent zeolite was first calcined at 550ºC for 4 hours, with a heating rate of 2ºC/min under 100 mL/min continuous flow of synthetic air (Ramp 1). To produce the Na-, Ca-, and Co-titrated zeolites (Y15Na, Y15Ca, Y15Co), an ion exchange procedure was performed between the parent zeolites and an aqueous solution containing a 0.01M metal nitrate. The various levels of Na titration were synthesized by exchanging the parent Y15 zeolite at various $NaNO_3$ solutions (0.01M, 0.025M, 0.065M). The exchange process was carried out at room temperature for one hour. Following the exchange, the samples were washed with deionized water, filtered, and dried in a vacuum oven at 80ºC overnight. Once dried, the samples underwent a similar calcination step (i.e., Ramp 1).

As for the La-containing Y zeolites, two different parent zeolites were used: zeolite Y with Si/Al=2.6 (CBV 300) and zeolite Y with Si/Al=30 (CBV 760), both were obtained in the NH_4 form from Zeolyst International. To produce the proton form, the parent zeolites were calcined to get HY2.6 and HY30, respectively, using a different ramping program (Ramp 2): heating to 90ºC at 5ºC/min, holding at 90ºC for one hour, heating to 350ºC at 0.5ºC/min, and then to 550ºC at

2ºC/min, and finally holding at 550ºC for 4 hours under 100 mL/min continuous flow of synthetic air.

Lanthanum (III) nitrate hexahydrate (>99%) was obtained from Sigma-Aldrich. Lanthanum was introduced via different methods for the two zeolites. For Si/Al=2.6 (LaY2.6), La was incorporated via ion-exchange with 0.5 M of lanthanum (III) nitrate solution (12 mL/g parent zeolite) at 80ºC for one hour. Following the exchange, the sample was washed with deionized water, filtered, and dried in a vacuum oven at 80ºC overnight. Once dried, the zeolite was calcined using Ramp 2. On the other hand, for Si/Al=30 (LaY30), La was introduced via incipient wetness impregnation (0.2 mL/g) using various lanthanum (III) nitrate solutions. After the impregnation step, the zeolite was dried overnight in a vacuum oven at 80ºC. Once dried, the zeolite was calcined using Ramp 2. The LaY30 samples are identified according to the La weight % in the catalyst.

The elemental analysis to quantify Si, Al, metal cations weight % in some samples was provided by Galbraith Laboratories (Knoxville, TN) using GLI Procedure ME-70.

2.2.2 Powder X-Ray Diffraction (XRD)

Powder X-ray diffraction (XRD) was performed on a Rigaku Ultima IV diffractometer (Cu Kα radiation, λ =1.5406 Å) in the 2θ range of 5–70° under an operating voltage of 40 kV and a current of 44 mA. Each sample was pretreated in a vacuum oven at 80 °C to remove moisture.

2.2.3 Isopropylamine Temperature Programmed Reaction/Decomposition (IPA-TPD)

Temperature-programmed desorption (TPD) of adsorbed isopropylamine was used to quantify the density of BAS. In each TPD measurement, 50 mg of catalyst was pretreated mirroring the treatments employed in reaction runs. After pretreatment, the catalyst was cooled to 100 °C under 20 sccm of He and exposed to ten consecutive 2 μL pulses of IPA. After flushing under He for 12 h at 100 °C to remove weakly adsorbed IPA, a 10 °C/min linear heating ramp was applied up to 600 °C. The desorbed products were analyzed and quantified on a Microvision Plus MS, scanning over a 1–60 m/z range at a speed of 26 cycles/min. To quantify the BAS density, the propylene signal (m/z = 41) was calibrated with 500 μL propylene pulses.

2.2.4 Catalytic Reaction

The vapor-phase conversion of isooctane (>99.5%, Sigma-Aldrich) over various zeolites was evaluated in a fixed-bed quartz tube reactor operated in either flow or micropulse mode by using a 6-port valve with constant loop volume of 500 μL. In flow-mode, a continuous and steady supply of reactants to the reactor was kept for a specified time on stream, whereas in micropulse mode, the 6-port valve set-up provides intermittent reactant injections to the reactor bed as the sample loop is filled with isooctane vapor in N_2. The reactant isooctane was fed using a syringe pump (KDS100, KD scientific) and vaporized before entering the N_2 stream (carrier gas) with the aid of heating tapes. In both modes, a the catalyst sample (ground pressed pellets 40-60 mesh) was placed between two layers of quartz wool in the center of the reactor. We must note here that even though the reactant in the injection loop used in the micropulse mode has the same isooctane partial pressure as the reaction stream in the continuous flow mode, the catalyst bed experiences a much lower isooctane exposure in the micropulse mode due to both the much shorter contact time of the

reactant molecules and the catalyst bed and the reactant axial dispersion through the carrier gas line.

Before every reaction run, the catalyst was pre-treated under flowing N_2 at 350ºC for 2 hours to remove any impurities or adsorbed water, and later, heated to the desired reaction temperature (400°C) at a ramping rate of 2ºC/min. All lines were kept heated at 230°C to avoid reactants and products condensation. The reaction was carried out at atmospheric pressure. For the Y15 series, the N_2/isooctane molar ratio was kept at 60 in all runs (1.7 kPa isooctane partial pressure), with 100 mL/min carrier gas flow. Products were quantified online in a gas chromatograph (GC7890B, Agilent) equipped with an HP-plot column. Prior to the catalytic tests, all products were identified by gas chromatography-mass spectrometry (GC-MS, Shimadzu QP2010SE).

2.2.5 Determining the rate and distribution of protolytic cracking, hydrogen transfer and dehydrogenation.

Compared to the cracking of other molecules of similar size, isooctane cracking demonstrates a much narrower product distribution. In fact, almost all the experiments conducted in this study at 400ºC resulted in over 95% of the products comprising just four species: C_1, $C_{3=}$, C_4, and $C_{4=}$. As depicted in **Schemes 1** and **2**, conversion of each isooctane molecule produces one C_1 and one $C_{4=}$ via protolytic cracking (PC); one C_4 and $C_{4=}$ via hydrogen transfer (HT); and two $C_{4=}$ via dehydrogenation (DH). Based on this assumption, the molar contribution to $C_{4=}$ production from PC, HT, and DH can be obtained using the following equations:

$$mol\ of\ C_{4=}\ from\ PC = mol\ C_1 \quad (1)$$

$$mol\ of\ C_{4=}\ from\ HT = mol\ C_4 \quad (2)$$

$$mol\ of\ C_{4=}\ from\ DH = total\ mol\ C_{4=} - PC\ mol\ of\ C_{4=} - HT\ mol\ of\ C_{4=} \quad (3)$$

Once the $C_{4=}$ contribution from DH pathway is known, the selectivity towards PC, HT, and DH can be found according to the following equations:

$$S_{PC} = \frac{mol\ C_1}{mol\ C_1 + mol\ C_4 + \frac{DH\ mol\ of\ C_{4=}}{2}} \quad (4)$$

$$S_{HT} = \frac{mol\ C_4}{mol\ C_1 + mol\ C_4 + \frac{DH\ mol\ of\ C_{4=}}{2}} \quad (5)$$

$$S_{DH} = \frac{\frac{DH\ mol\ of\ C_{4=}}{2}}{mol\ C_1 + mol\ C_4 + \frac{DH\ mol\ of\ C_{4=}}{2}} \quad (6)$$

Note that each isooctane molecule that reacts via the dehydrogenation pathway produces two $C_{4=}$. Using these equations as a basis in rate calculations, the rates of protolytic cracking (PC), hydrogen transfer (HT), and dehydrogenation (DH) can be calculated as follows:

$$-r_{iC8} = F_{iC8_o}\, X_{iC8} \quad (7)$$

$$r_{PC} = -r_{iC8}\, S_{PC} \quad (8)$$

$$r_{HT} = -r_{iC8}\, S_{HT} \quad (9)$$

$$r_{DH} = -r_{iC8}\, S_{DH} \quad (10)$$

Therefore, the distribution of the converted isooctane that went through each pathway can be calculated as:

$$\%\, PC = \frac{r_{PC}}{-r_{iC8}} \times 100\% \quad (11)$$

$$\%\, HT = \frac{r_{HT}}{-r_{iC8}} \times 100\% \quad (12)$$

$$\%\, DH = \frac{r_{DH}}{-r_{iC8}} \times 100\% \quad (13)$$

The experimental data can now be reported on a ternary plot, consisting of the protolytic cracking, hydrogen transfer, and dehydrogenation rate contributions to the overall isooctane conversion rate. This plot provides a quantitative description of the effect of different catalyst compositions and reaction conditions on the relative rates of the three reactions.

2.3 Results and Discussion

Table 1 summarizes the density of Bronsted acid sites (BAS) density for the parent Y15 zeolite and for those titrated with Na, Ca, and Co. The values were determined by the temperature-programmed desorption (TPD) of adsorbed isopropylamine. Additionally, the table includes the Si/Al ratio and the metal cation to Al ratio obtained from elemental analysis. The extent of titration has been kept at a low level to minimize the potential effects of subsequent reactions on the different cations. In fact, it can be observed that only about 10-20 % of the original BAS have been titrated. The BAS measurement by isopropylamine-TPD agrees with the theoretical BAS density determined using elemental analysis. **Figure 4** shows the XRD patterns of the Y15 zeolite samples used in this study. The patterns show that the titration of Y15 with the various cations does not alter the crystallinity of the parent zeolite. Similarly, the SEM images of the parent Y15 sample and the titrated zeolites (**Figure 5**) show no changes in either shape or average size of the particles, showing that the modifications made on these samples are strictly related to acid density rather than zeolite morphology. These properties are crucial in investigating monomolecular and bimolecular alkane cracking as they have been shown to be dependent on crystal sizes and intracrystalline gradients.

Table 1. Bronsted acid site density and elemental analysis of Y15, Y15Na, Y15Ca, and Y15Co.

Catalyst	BAS density (mmol H^+/g_{cat})	Si/Al	M/Al	Theoretical BAS density (mmol H^+/g_{cat})[a]
Y15	0.37 ± 0.01	16.7	-	0.37
Y15 Na	0.33 ± 0.01	16.6	0.084	0.34
Y15 Ca	0.29 ± 0.01	16.6	0.095	0.30
Y15 Co	0.33 ± 0.02	16.5	0.125	0.28

a) Using Y15 BAS as a basis, the theoretical BAS was calculated on the assumption that Na titrate one BAS, while Ca and Co titrate two BAS.

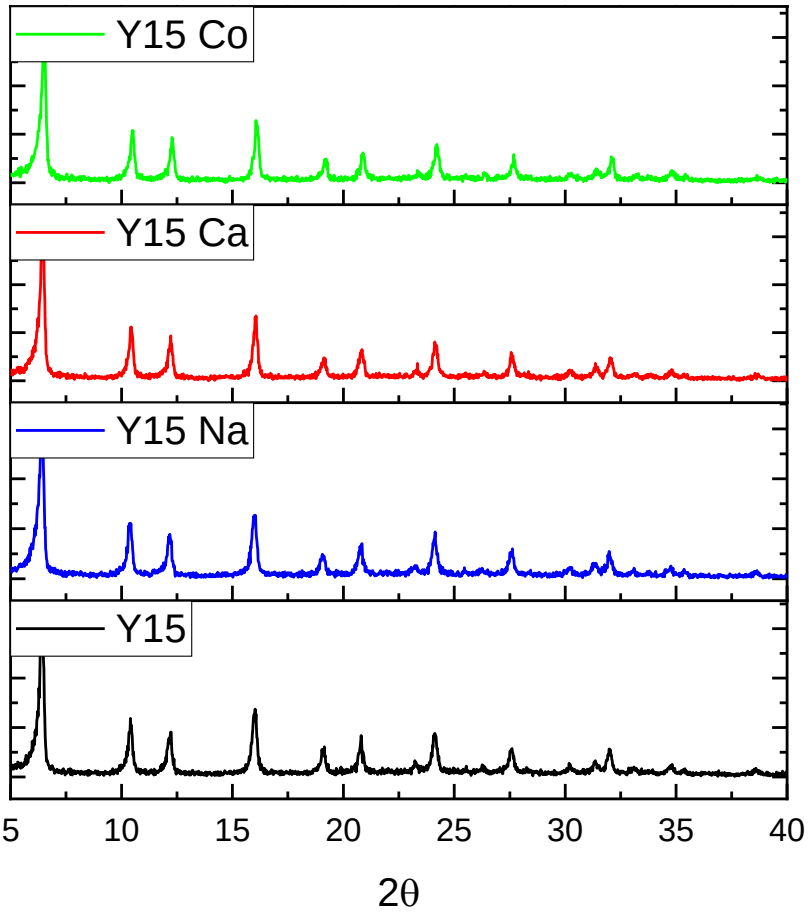

Figure 4. XRD patterns of Y15, Y15 Na, Y15 Ca, and Y15 Co.

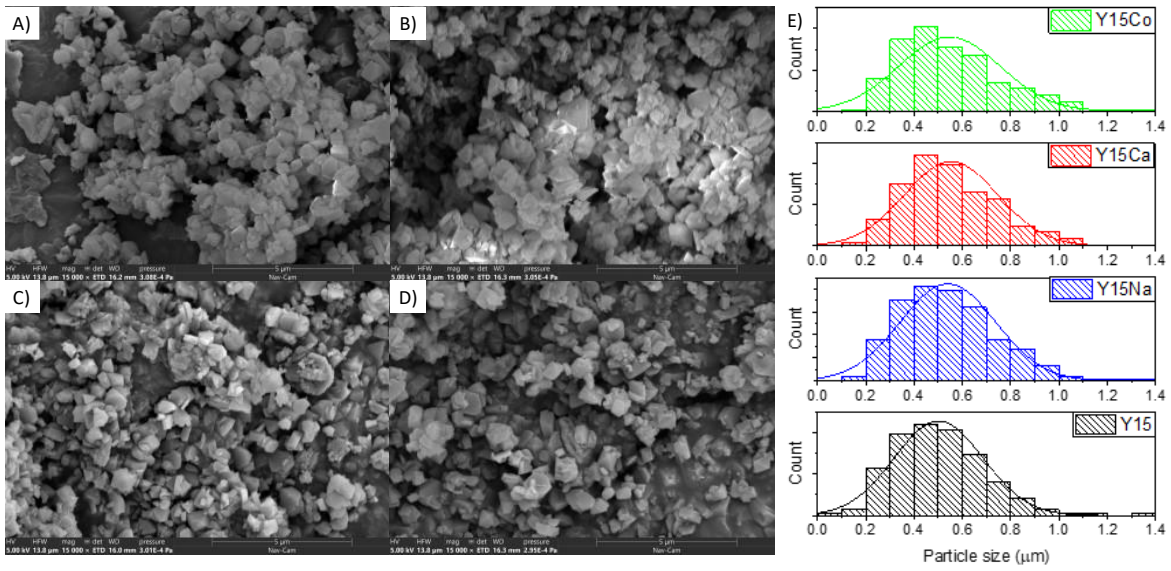

Figure 5. SEM images of Y15 (A), Y15 Na (B), Y15 Ca (C), Y15 Co (D), and the particle size distributions (E).

2.3.2 Isooctane Cracking Reaction Mechanism Over Acid Sites – Hydrogen Transfer, Protolytic Cracking, and Dehydrogenation Pathways

Over acid sites, the catalytic cracking of isooctane around 400 ºC selectively produces methane (C_1), propylene ($C_{3=}$), n- and iso-butane (C_4), and n- and iso-butene ($C_{4=}$), where the iso-isomers are predominant in C_4, and $C_{4=}$ products. Under the reaction conditions of this work, other products such as C_2, C_3 alkane, C_5, C_6, C_7, and C_8+ were only found in negligible amounts. Other works have found significant amount of these products [83, 84, 86], but this work's reaction conditions are operating at a higher temperature, lower isooctane partial pressure, and lower isooctane conversion, resulting in a cleaner, simpler products.

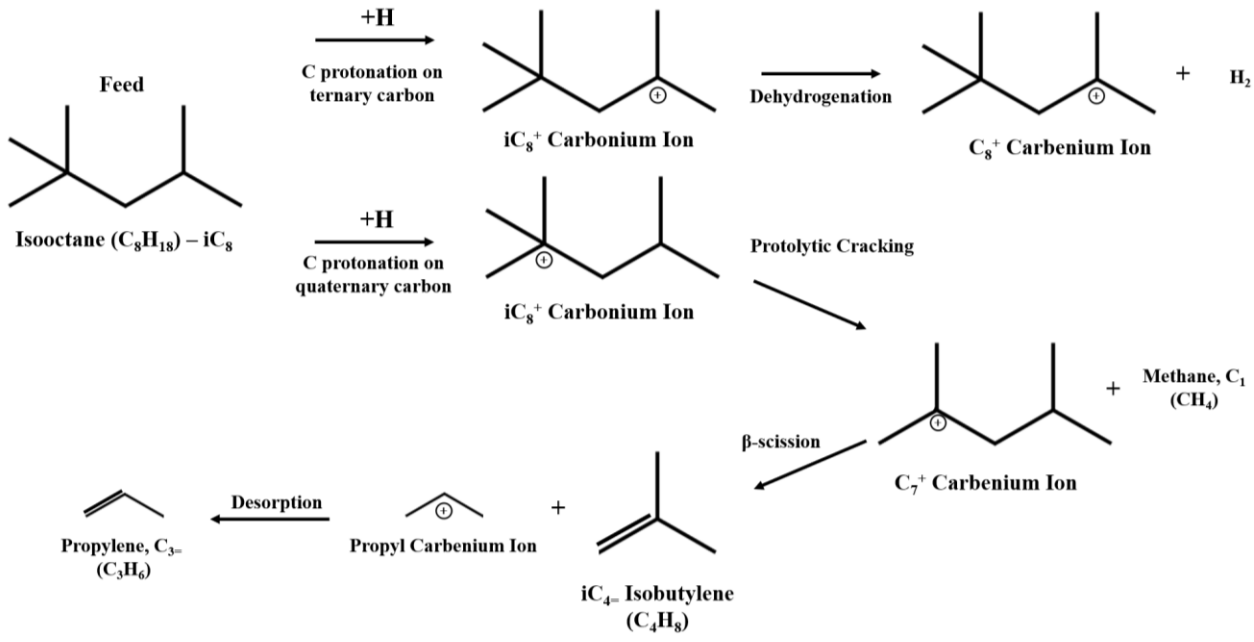

Scheme 5. Isooctane cracking over acid sites through protolytic cracking pathway via iC8 carbonium ion formation.

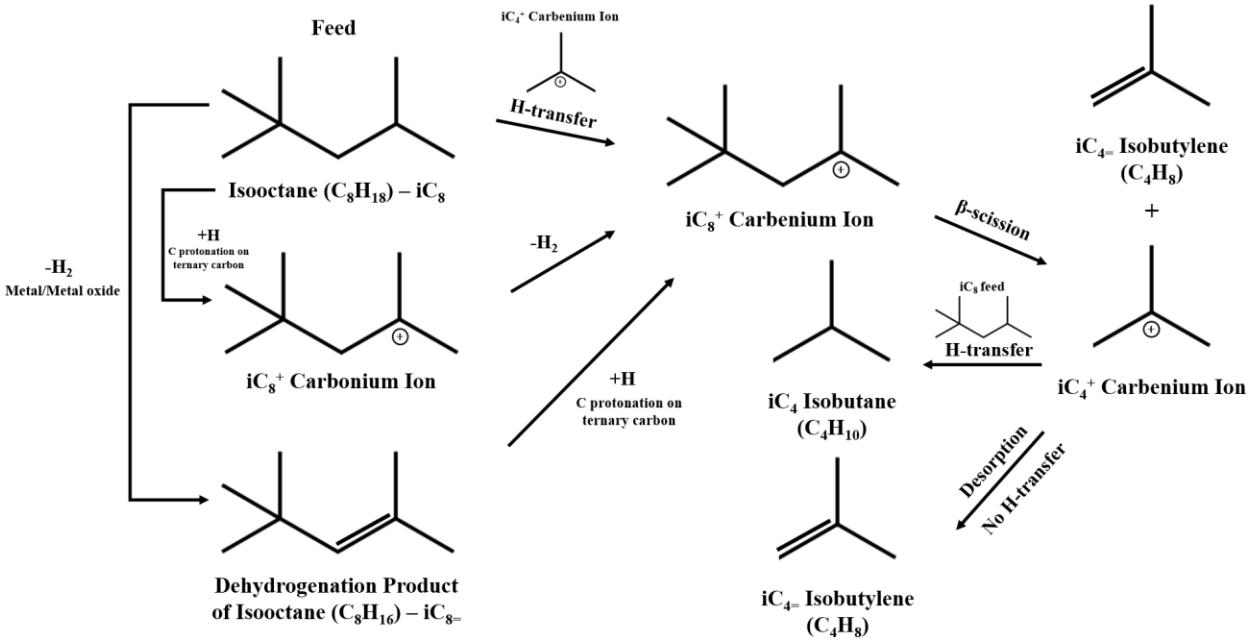

Scheme 6. Isooctane cracking over acid sites through hydrogen transfer pathway and dehydrogenation pathway via iC8 carbenium ion formation.

It is widely accepted that two major pathways lead to the formation of a transition state iC_8 carbocation. The first one occurs via a penta-coordinated carbonium ion, formed by direct protonation of the isoalkane (**Scheme 5**) [77]. This carbonium ion can further react via dehydrogenation or protolytic cracking. The former produces H_2 and a carbenium ion while the latter causes the cleavage of the C-C bond. In principle, this cleavage can occur on any C-C bond in the molecule. However, under our conditions (400ºC, low conversions) the only PC fragment observed is methane. Moreover, we found that this methane is produced exclusively from bond breaking at the quaternary carbon. This conclusion is supported from separated cracking measurements conducted at 400ºC and low conversions on three other molecules, isobutane, 2-methylhexane and 2,5-dimethylhexane over the same Y15 zeolite. All these molecules contain a terminal tertiary carbon, replicating the tertiary carbon present in the isooctane molecule, but no quaternary carbon. In the case of isobutane cracking over Y15 zeolites, the dominant products were all the $C_{4=}$ alkene isomers (64 mol%) produced via dehydrogenation, with much lower

amounts of C_1 (14 mol%) and $C_{3=}$ (14 mol%) produced via protolytic cracking. Similarly, 2-methylhexane only produced insignificant quantities of C_1 (<1%, see **Figure 6)** compared to the C_3 and C_4 products, confirming the hypothesis that, under these mild conditions, protolytic cracking in the iC_8 only occurs at the quaternary carbon. More importantly, under the same conditions, the cracking of these three molecules without a quaternary carbon yielded much less C_1 (2 orders of magnitude) than that obtained from isooctane cracking that contains one quaternary carbon, further suggesting that most of the C_1 produced from isooctane cracking cannot come from the terminal tertiary carbon.

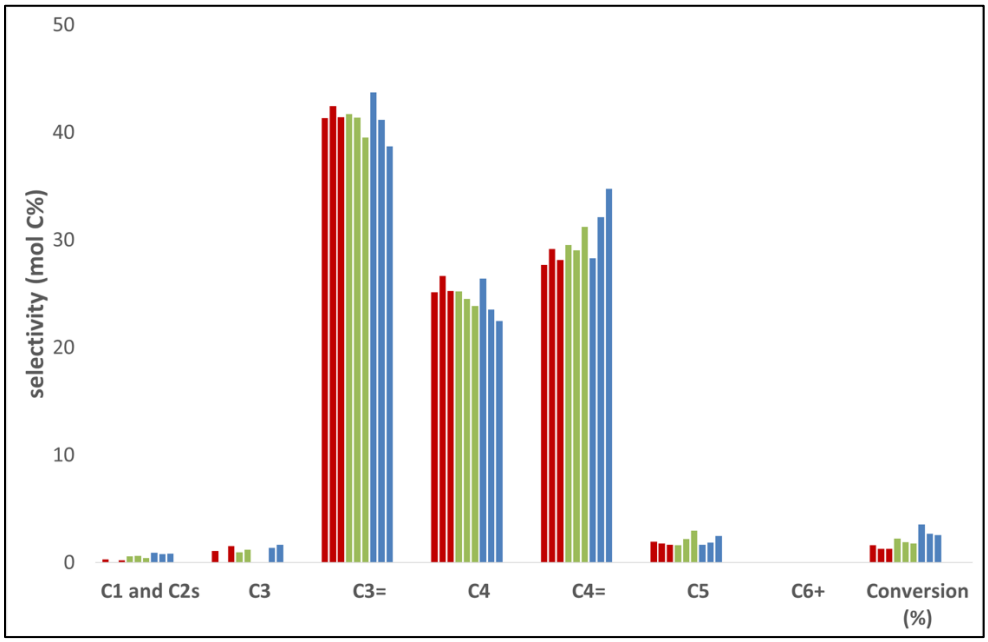

Figure 6. Products distribution and conversion of 2-methylhexane cracking over Y15 zeolite in flow mode. Red bars: 400 °C, green bars: 410 °C, blue bars: 420 °C. Subsequent bar of a given color represents various iC8 feeding rate: 0.4, 0.6 and 0.8 mL/hr. Reaction conditions: 50 mg, 80 mL/min of He flow. Pretreatment under He flow at 300 °C for 2 hours.

In agreement with this conclusion, when comparing the cracking of isobutane (tertiary carbon) and neopentane (quaternary carbon) over solid acids, Engelhardt and Hall observed that C_1 yield in neopentane cracking was significantly higher than that from isobutane cracking, since

the only possible reaction pathway for neopentane is demethylation, producing C_1 and $C_{4=}$, while isobutane preferentially goes through dehydrogenation, producing H_2 and $C_{4=}$ [87].

In summary, protonation of the tertiary carbon in isooctane preferentially yields dehydrogenated products, resulting in iC_8 alkene ($iC_{8=}$) and hydrogen gas, H_2. In addition, it is worth noting that $iC_{8=}$ was not detected in any of these runs. It is most likely that it remains protonated as a surface iC_8 alkoxide and then it goes through carbenium ion chemistry (**Scheme 6**).

On the other hand, the PC step that yields methane forms a heptyl carbenium ion (C_7^+) in the transition state, which then goes through a β-scission step, resulting in C_3 alkoxide and $C_{4=}$ as products. Due to the highly branched nature of the transition state, the heptyl carbenium ion are allowed to proceed to β-scission, while minimally desorbed as a C_7 alkene (<0.01% mol selectivity). Under the reaction conditions of this study, almost all the C_3 alkoxide desorbs as a $C_{3=}$, via a propyl carbenium ion (C_3^+) transition state which is a much poorer hydrogen acceptor compared to the isobutyl carbenium ion (C_4^+) transition state [39]. The important conclusion from this analysis is that the isooctane cracking initiated via protolytic cracking route will form equimolar amounts of C_1, $C_{3=}$ and $C_{4=}$ as products.

The second major mechanism is the formation of the iC_8 carbenium ion (**Scheme 6**) [35, 40, 42, 88]. This can be formed either from the iC_8 alkane reactant via H-transfer to a surface C_4 alkoxide (HT pathway), or from the protonation of the dehydrogenated iC_8 (DH pathway). In turn, the dehydrogenated iC_8 can be formed either via carbonium ion chemistry (**Scheme 5**), or via dehydrogenation catalyzed by metals/metal oxide species. The resulting iC_8^+ carbenium ion in the transition state undergoes β-scission, forming $C_{4=}$ and C_4 alkoxide. Depending on the environment around the active site, the C_4^+ from the C_4 alkoxide can either desorb as a $C_{4=}$ (no HT, DH pathway)

or receive a hydride from a nearby iC_8, forming the C_4 alkane (HT pathway). The latter results in a transition state iC_8^+ carbenium ion which continues the catalytic cycle. Further protolytic cracking of the C_4 alkane is disregarded due to the high activation barrier of the C_4 alkane cracking under the conditions of these experiments. Therefore, the only products coming out of this mechanism are C_4 and $C_{4=}$. That is, in the hydrogen transfer pathway, one isooctane cracking event produces one C_4 and one $C_{4=}$; while in the case of the dehydrogenation pathway, one isooctane cracking event produces two $C_{4=}$.

Since out of the three major reaction pathways, C_1 and $C_{3=}$ are only produced from the protolytic cracking pathway, while the alkane C_4 is only produced from the hydrogen transfer pathway, we can use the product distribution to quantify the contributions from each path. That is, while C_1 (or $C_{3=}$) can be used as an indicator of protolytic cracking, C_4 can be used as an indicator of hydrogen transfer. Thus, we can illustrate the relationship between protolytic cracking, hydrogen transfer and dehydrogenation pathway by using a plot of C_4 alkane selectivity vs. C_1 selectivity. We expect that on one extreme, if the reaction conditions resulted in a case in which 100% of the reacted isooctane undergoes protolytic cracking, the product will only be an equimolar mixture of C_1, $C_{3=}$ and $C_{4=}$ products with no alkane species present. In this case, on the C_4 selectivity vs. C_1 selectivity plot, the point of 100% PC will be at the point of 33% C_1 selectivity, and 0% C_4 selectivity. On the other hand, in the case of 100% hydrogen transfer pathway, without PC, the resulting product distribution will be an equimolar mixture of C_4 and $C_{4=}$. Thus, this point (100% HT) will be at 0% C_1 selectivity, and 50% C_4 selectivity. When both protolytic cracking and hydrogen transfer occur at varying percentages, one will expect that all these points will fall on a straight line from (0, 50%) to (33%,0). This line is illustrated in **Figure 7** as the proposed mechanisms line. Further, if produced olefins readsorb along the diffusion path or within the

catalyst bed, they will produce the same outcome. Readsorption will result in a carbenium ion that will either desorb again as an olefin in the absence of a hydride donor, or as a paraffin if hydride transfer is more prevalent.

As shown below, this is in fact the observed experimental trend. Most points fall on this line. There are only two scenarios that can cause a deviation from this straight line. The first scenario is when the transition state iC_8 carbenium ion is formed via the dehydrogenation route. This will cause the C_4 alkane to be replaced by $C_{4=}$, resulting in a C_4 alkane selectivity lower than that predicted by the straight line. The second scenario that would cause a departure from the straight line would be due to the presence of an external hydrogen donor, either from a gas phase molecule or from coke. This will cause the C_4 selectivity to go above the dotted line due to enhanced HT.

In good agreement with this analysis, the experimental data reflect the proposed behavior. **Figure 7** shows a graph of the C_4 alkane selectivity vs. C_1 selectivity at 400 °C on the parent and cation-titrated Y15 zeolites, obtained in both micropulse and flow modes at isooctane conversions in the range 0-10 %. Despite the changes in catalyst formulation and reaction conditions, almost all the data points lie on the straight line derived above considering the interplay between hydrogen transfer and protolytic cracking. In other words, nearly all the product distributions for this reaction, including those where the olefin to paraffin ratio was markedly different at identical conversion levels, can be explained by a simple balance of protolytic cracking and hydride transfer reaction rates.

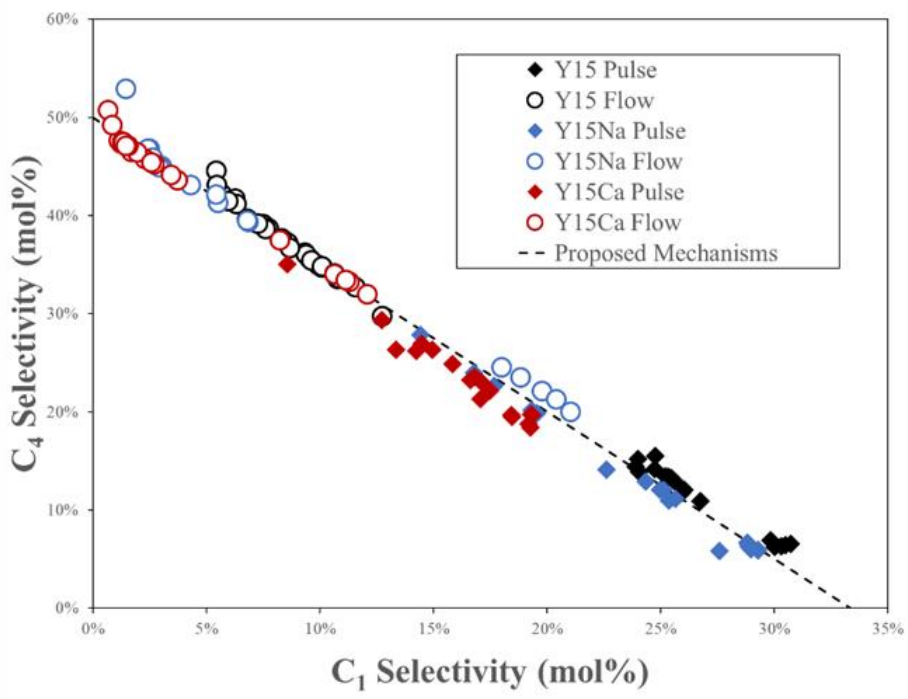

Figure 7. Experimental data of parent, Na and Ca titrated Y15 for both pulse mode and flow mode reactor at various conversion, along with the proposed correlation. Reaction conditions: Both, in the feed to the continuous flow reactor and the injection loop to the micropulse reactor the isooctane partial pressure was 1.7 kPa; in both cases, the carrier gas flow rate was 100 mL/min, at 400ºC and 1 atm. The conversion was varied by changing the catalyst mass in the range 5-30 mg.

Instances where a dehydrogenation pathway and an external hydrogen donor influence the position on the C_4 vs C_1 plot will be discussed in the following section. As summarized in **Table 2**, it can be observed that the enhanced selectivity towards HT exhibited by the Na- and Ca-titrated samples is not due to a higher HT rate but rather to a lower PC rate. The significant decrease of isooctane cracking turnover frequency (TOF) will be discussed in the future section.

Table 2. Turnover frequency (TOF) of protolytic cracking and hydrogen transfer for Y15, Y15Na and Y15Ca. Reaction conditions: pulse mode, isooctane partial pressure was 1.7 kPa, the carrier gas flow rate was 100 mL/min, at 400ºC and 1 atm. Reaction for all catalysts under similar range of isooctane conversion (8-10%).

TOF (hr^{-1})	Y15	Y15Na	Y15Ca
Protolytic cracking	52.8 ± 6.4	15.5 ± 3.2	2.5 ± 0.7
Hydrogen Transfer	27.2 ± 3.9	19.8 ± 1.0	19.2 ± 2.8

2.3.3 Enhanced Dehydrogenation Pathway by Cobalt Titration and Gas-Phase Hydrogen Donation from 2,3-Dimethylbutane

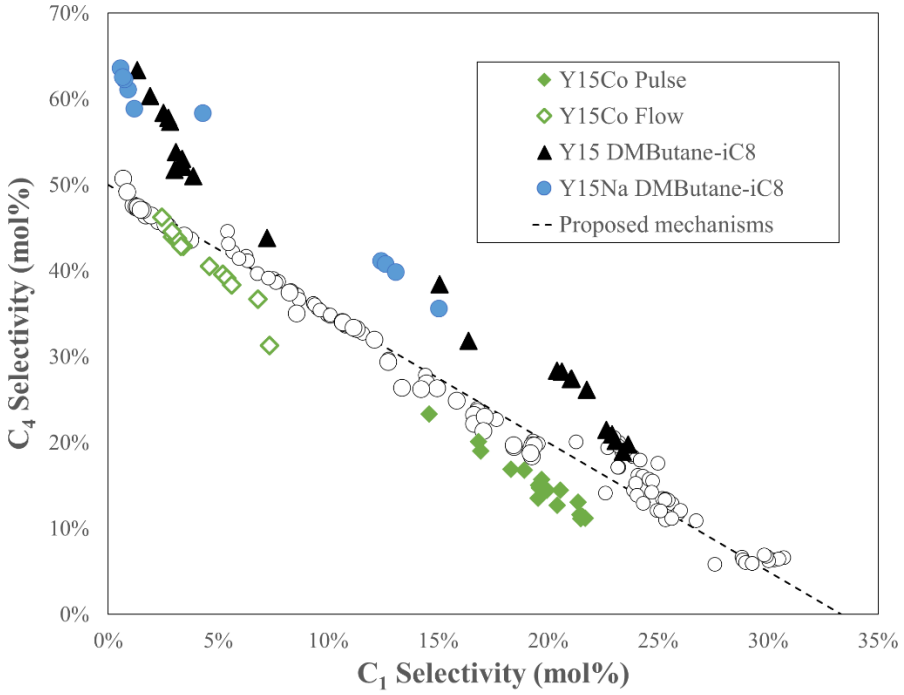

Figure 8. C4 vs C1 selectivity plot of Co titrated Y15, and isooctane cofed with dimethylbutane over Y15 and Y15Na. Reaction conditions: Both, in the feed to the continuous flow reactor and the injection loop to the micropulse reactor the isooctane partial pressure was 1.7 kPa; in both cases, the carrier gas flow rate was 100 mL/min, at 400ºC and 1 atm. The conversion was varied by changing the catalyst mass in the range 5-30 mg. DMButane was cofed at 1.2 kPa.

In Section 3.1, it was noted that the dehydrogenation pathway involving the tertiary carbon of isooctane is also a feasible route, resulting in the formation of two $C_{4=}$ molecules. Consequently, if dehydrogenation contributes significantly to the rate the data points on the C_4 vs C_1 selectivity plot will tend to be lower than the protolytic cracking-hydrogen transfer interplay line, as C_4 is being compensated by $C_{4=}$ instead. Examining Figure 8, the Co-titrated Y15 data falls below this line, indicating that Y15Co undergoes partial dehydrogenation pathway during isooctane cracking. The deviation from the line is more prevalent when Y15Co is operating in pulse mode. **Figure 2** also highlights instances where the data points surpass the protolytic cracking-hydrogen transfer

interplay line, particularly with the introduction of 2,3-dimethylbutane (DMButane) in the gas phase alongside isooctane. This phenomenon is observed for both parent Y15 and Y15Na zeolites. Under these conditions, DMButane serves as a hydrogen donor to the surface butoxide, leading to the formation of C_4 and dimethylbutyl alkoxide on the surface. Consequently, the production of C_4 extends beyond the protolytic cracking-hydrogen transfer line, as it does not rely on isooctane to donate hydrogen for C_4 formation. DMButane was selected due to its tendency, under these reaction conditions, to yield propylene as the major product. This is primarily resulting from the least energy-intensive form of β-scission of the dimethylbutyl carbenium ion transition state [89]. As a result, only minimal amounts of C_1 and C_4 products are generated from DMButane, and this approach effectively eliminates the contribution of C_4 products from DMButane in the analysis of isooctane products. In section 3.5, the discussion explores the effects of reaction modes (pulse vs. flow) and the role of Co in enhancing the dehydrogenation pathway.

2.3.4 Shortcomings of using $C_4/C_{4=}$ ratio as an indicator of hydrogen transfer activity in isooctane cracking

Traditionally, the product alkane/alkene ratio has been used as an indicator of hydrogen transfer activity. In the case of isooctane, after the beta-scission step, produces an isobutyl carbenium on the surface [64]. The ratio of C4 alkane to alkene ($C_4/C_{4=}$ ratio) which then used as a hydrogen transfer index since this ratio reflects the fate of the butyl carbenium ion on the surface, either receiving a hydride from the gas phase alkane to form butane (C_4) or desorbing from the surface to form butene ($C_{4=}$). Therefore, it is usually assumed that at a given catalytic conversion, the $C_4/C_{4=}$ ratio provides a direct quantification of the hydrogen transfer ability of different catalyst samples. However, as illustrated in **Figure 9**, this may not always be the case. The figure shows the $C_4/C_{4=}$ ratio at varying catalytic conversions of isooctane for different samples, including Na-,

Co-, and Ca-titrated HY zeolites. Based on the results summarized in the figure and on the assumption described above, one would conclude that the addition of cations (particularly Na or Ca) to zeolite Y improves the hydrogen transfer activity of the zeolite, which would be against any common knowledge. It is well established that Na and Ca simply titrate or remove acid sites within the zeolite, but should not improve the intrinsic HT activity [90, 91]. From this work, it was found that this ratio is influenced by the protolytic cracking pathway, since $C_{4=}$ is a product. This will result in a higher $C_4/C_{4=}$ when protolytic cracking rate is suppressed, leading to erroneous conclusions pertaining to hydrogen transfer activity.

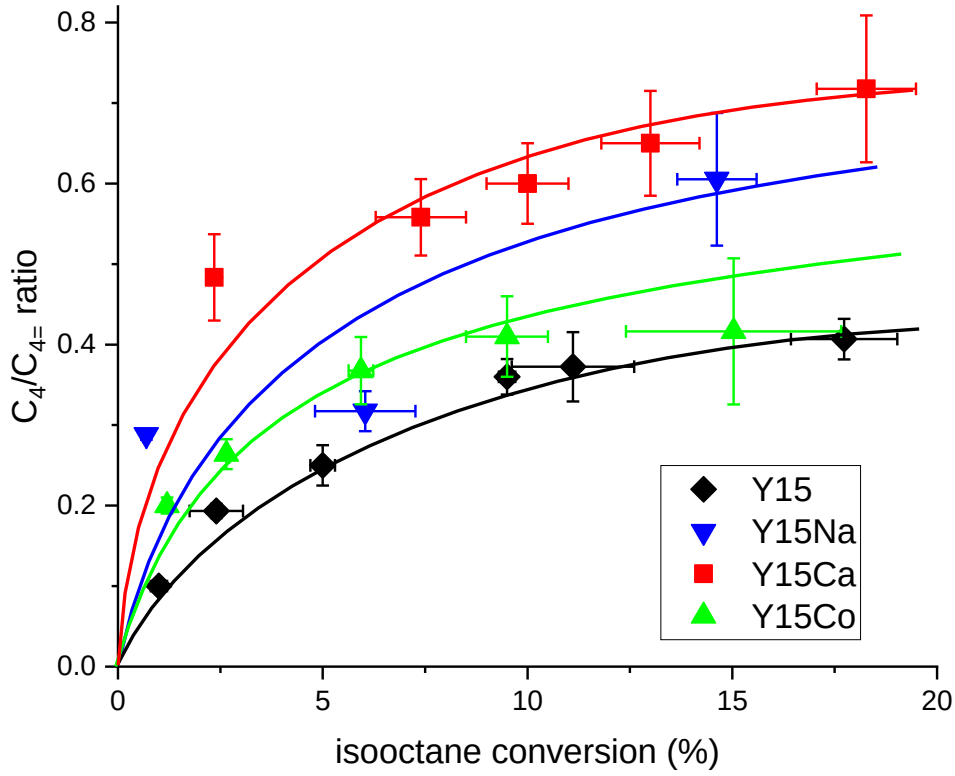

Figure 9. C4/C4= ratio of varying isooctane conversion over parent (◆), Na- (▼), Ca- (■), and Co- (▲) titrated Y15 zeolite. Reaction conditions: micropulse mode reactor at 1.7 kPa of isooctane partial pressure, 100 mL/min of carrier gas flow, 400ºC, 1 atm. The conversion was varied by changing the catalyst mass, 5-30 mg. Error bars are the deviation of six subsequent pulses of isooctane.

2.3.5 Role of synergistic sites– varying Na titration level in Y15 zeolite

As shown in **Table 2,** after the titration of Bronsted acid sites with Na and Ca, the total TOF in isooctane cracking decreases significantly. To further investigate this observation, Y15 zeolite was titrated at varying levels of Na to vary the Bronsted acid concentration.

Figure 10 shows the relationship between isooctane cracking and the fraction of BAS titrated by Na. The cracking of isooctane decreases significantly with 10% of sites titrated by Na, and the activity remains relatively constant with further titration. Similar observation with Ca titrated Y15 where the titration of approximately 20% of the sites resulted in a decrease more than twofold of the cracking activity.

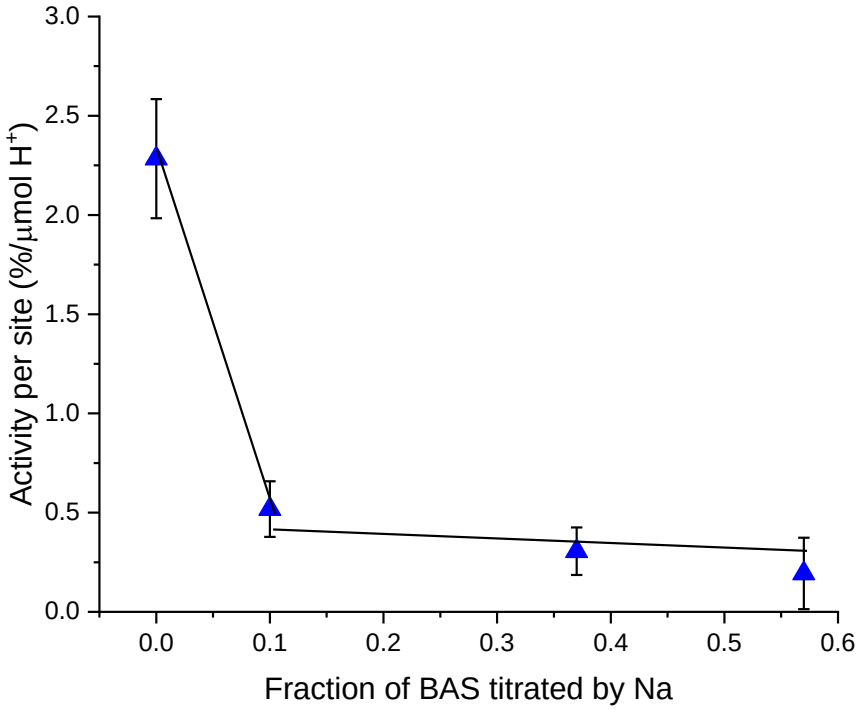

Figure 10. Conversion of isooctane per Bronsted site over Y15 at various level of Na titration. Reaction conditions: 400ºC, 3.5 mg, flow mode, 250 min time on stream. Error bars reflect the deviation in activity over the whole time on stream.

In zeolites, surface features, including site proximity, EFAl, and partially coordinated species, can modify the local environment of the Bronsted acid site [23, 24, 92-94]. It was previously shown where Na has a preferential titration towards these Bronsted sites (synergistic

sites) [24]. Furthermore, these sites have shown to lower the activation enthalpy in hexane cracking over MFI zeolites [24, 93]. Via DFT calculations, it was also reported that the presence of EFAl around the sodalite cage in Y zeolites altered the activity of the supercage's Bronsted sites in performing propane cracking [95, 96]. The isooctane cracking results are consistent with these works, and the decrease in TOF is due to Na preferentially titrates these synergistic sites.

2.3.6 Y15 and titrated Y15 Analysis using Ternary Plots

Using the experimental data points obtained from the isooctane cracking on different titrated zeolites samples, the distribution of protolytic cracking, hydrogen transfer, and dehydrogenation can be plotted on a ternary diagram. **Figure 11** shows the data for the parent zeolite and the cation (Na, Ca, Co) - titrated Y15 at similar extent of isooctane conversion.

The plot reveals several interesting trends. First, when comparing data for all catalysts obtained in the pulse and flow modes, the former tends to favor protolytic cracking, while the latter tends to favor hydrogen transfer. This is a reflection of the characteristics of the different reactant concentration profiles in the two methods of reactant introduction. In the flow mode, the catalyst is continuously exposed to the partial pressure of the feed. By contrast, as mentioned before, in the pulse mode, only the injection loop has the inlet partial pressure of 1.7 kPa. As a micropulse is injected into the carrier gas, the plug of reactant passes through the reactor, and the catalyst is exposed for a short period of time to a similar or lower partial pressure, depending on the degree of axial mixing. More importantly, the lifetime of reactants on the surface of the catalyst may greatly outlast the lifetime of a perpetual concentration of reactants in the gas phase.

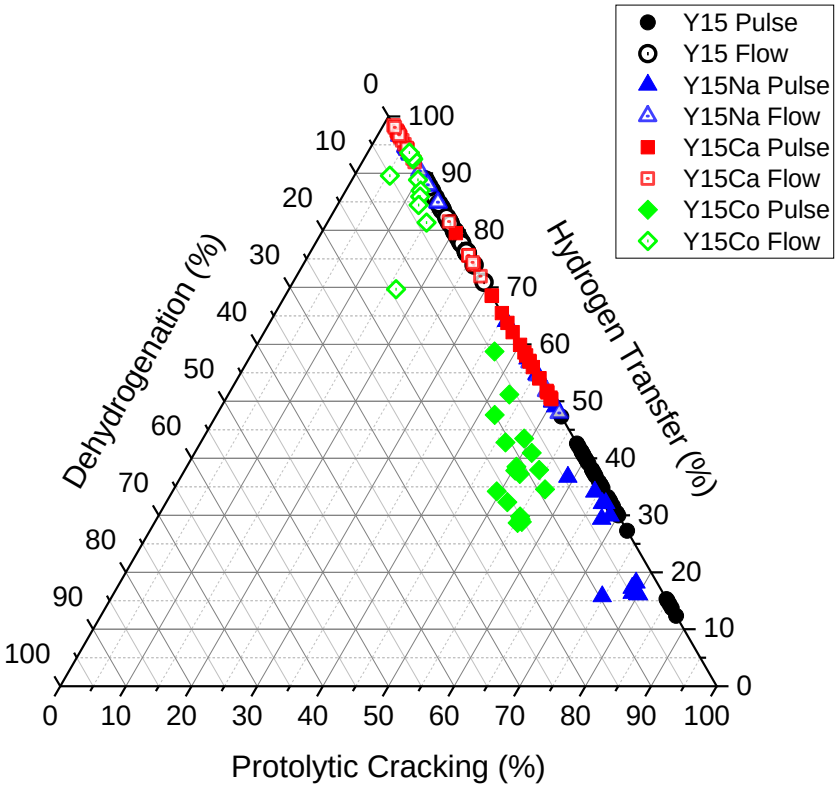
Y15 Pulse
Y15 Flow
Y15Na Pulse
Y15Na Flow
Y15Ca Pulse
Y15Ca Flow
Y15Co Pulse
Y15Co Flow
Dehydrogenation (%)
Hydrogen Transfer (%)
Protolytic Cracking (%)

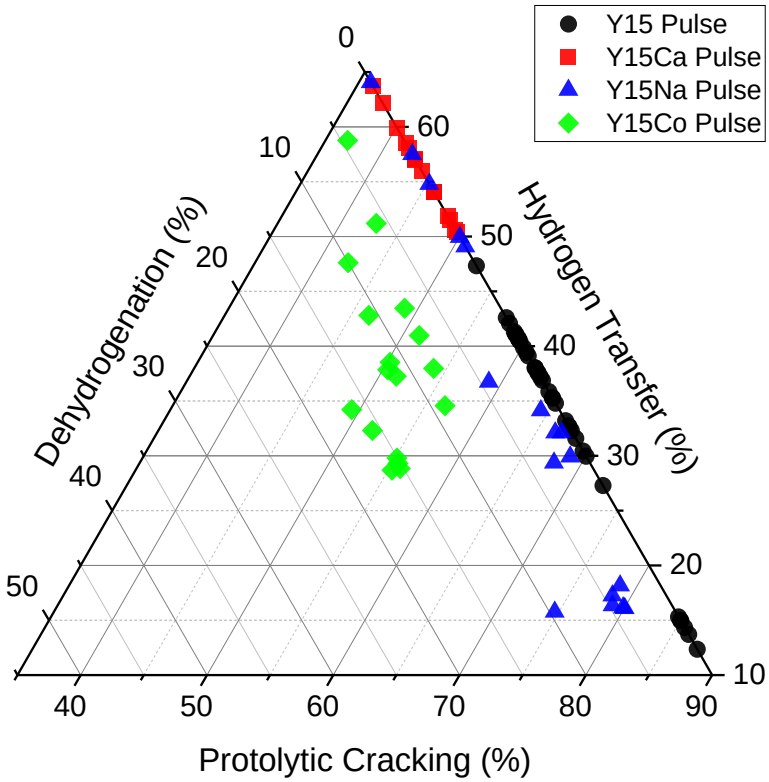
Y15 Pulse
Y15Ca Pulse
Y15Na Pulse
Y15Co Pulse
Dehydrogenation (%)
Hydrogen Transfer (%)
Protolytic Cracking (%)

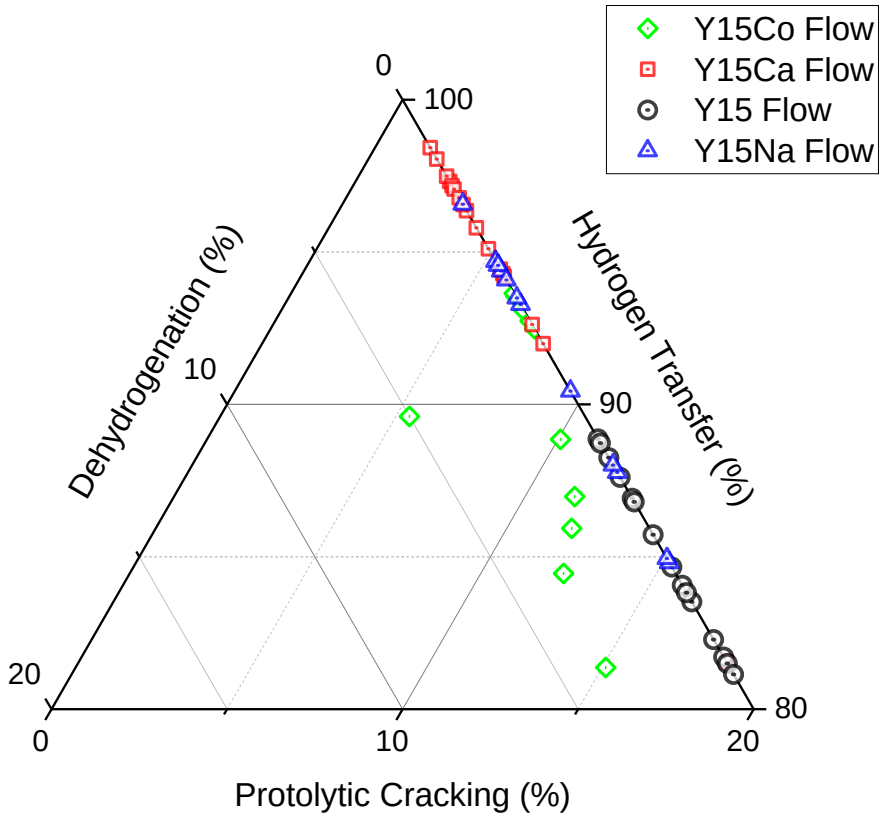

Figure 11. A) Ternary Plot of various titrated Y15 samples for both flow mode and pulse mode, B) Pulse mode region, C) Flow mode region.

Hydrogen transfer is a bimolecular reaction, requiring a butyl alkoxide species on the surface, which in the transition state (carbenium ion) acts as H^- acceptor and the gas phase isooctane molecule, which participates as H donor. On the other hand, protolytic cracking is a monomolecular reaction, in which the isooctane molecule is protonated, and C-C cracked directly by an acid site. Therefore, it is reasonable that HT is favored at the higher isooctane partial pressures of the flow mode, while PC is favored at the lower partial pressures and short exposure times present in the pulse mode [35, 42, 77]. It is also observed that the addition of Na and Ca causes shifts in the cracking reaction towards the hydrogen transfer region in both pulse and flow mode. This is due to the suppression of the PC pathway caused by the blocking of acid sites rather than an increase in HT. As mentioned above, the enhanced $C_4/C_{4=}$ ratio does not necessarily reflect

a direct increase in hydrogen transfer, but rather a decrease in protolytic cracking. Co-titrated Y15 results in a higher extent of dehydrogenation relative to other catalysts, and this is more prevalent in the pulse mode region. In previous studies Co have been shown to increase alkane dehydrogenation, which reflected in enhanced isooctane cracking [97-99]. Since the dehydrogenation reaction is also a monomolecular reaction, a catalyst with higher degree of dehydrogenation will show an enhancement in dehydrogenation rate at lower partial pressures. In summary, isooctane cracking is a useful probe reaction to quantify the distribution of different reaction pathways under cracking conditions.

2.3.7 Case study: Understanding the role of Lanthanum in alkane cracking using isooctane cracking as a probe reaction.

Lanthanum-modified Y zeolites serve as an industrially relevant catalyst that can be used as case-study to test the validity of the isooctane cracking as a probe to quantify the contributions of each reaction. Lanthanum is widely used as an additive in FCC catalysts, due to its ability to preserve the zeolitic structure under hydrothermal conditions, as well as improving hydrogen transfer rates. The improvement in hydride transfer activity has been ascribed to the ability of La to retain or/and increase the Bronsted acid density of the catalyst [100] or to directly enhance the intrinsic rate of hydrogen transfer [28, 32, 67, 101]. One of the proposed mechanisms of hydrogen transfer enhancement is the polarization of secondary and tertiary alkane C–H bonds by the isolated La^{3+} cations in the supercage of the Y zeolite, which allows a more stable generation of carbenium ions [29]. Furthermore, the incorporation of La into X and Y zeolites has been proposed to enhance the dehydrogenation of branched alkanes. This improvement has been ascribed to a stronger polarization of the alkane C-H bonds by the La cation that facilitates the hydride

abstraction, which then combines with the acidic proton, forming H_2 in the dehydrogenation step [29, 102, 103].

Table 3 summarizes the density of BAS of the parent Y2.6 zeolite and La titrated Y2.6, as determined by TPD of adsorbed isopropyl amine. It appears that the addition of La into Y2.6 zeolite increases the Bronsted acid density. Similar increases in acid density have been observed before, and the main causes for this enhancement have been highly debated in the literature. Some works attributed it to the lanthanum's ability to increase the hydrothermal stability of the zeolite structure, thus preserving the acid sites from dealuminating when exposed to a higher temperature processes [64, 104]. Others have argued that this enhancement is due to the presence of hydroxylated lanthanum species in the supercage that exhibit acidic behavior [29, 67, 102]. For the purpose of this work, both possibilities are considered, and using isooctane cracking may be a key probe to investigate La-containing faujasites, where hydrogen transfer is expected to improve due to a higher BAS density [67].

Table 3. Bronsted acid site density of Y2.6 and LaY2.6.

Catalyst	**BAS density* (mmol H^+/g_{cat})**
Y2.6	0.79 ± 0.02
LaY2.6	1.34 ± 0.04

Figure 12 shows the variation of the $C_4/C_{4=}$ ratio as a function of isooctane conversion over both Y2.6 and LaY2.6 catalysts. It is clear that the addition of La into Y2.6 improves the alkane/alkene ratio. As previously mentioned, based on conventional practice [28, 32, 67, 100, 101], one may be tempted to conclude that this result reflects an increased hydrogen transfer ability due to the presence of the La species. However, the effects of La on the competing protolytic cracking and dehydrogenation reactions have not been specifically quantified, and they can

influence the resulting $C_4/C_{4=}$ ratio, as shown here. Thus, by using isooctane cracking as a probe reaction, the effects of the presence of La in zeolite Y in performing these reactions at various reaction conditions can be better understood and precisely measured.

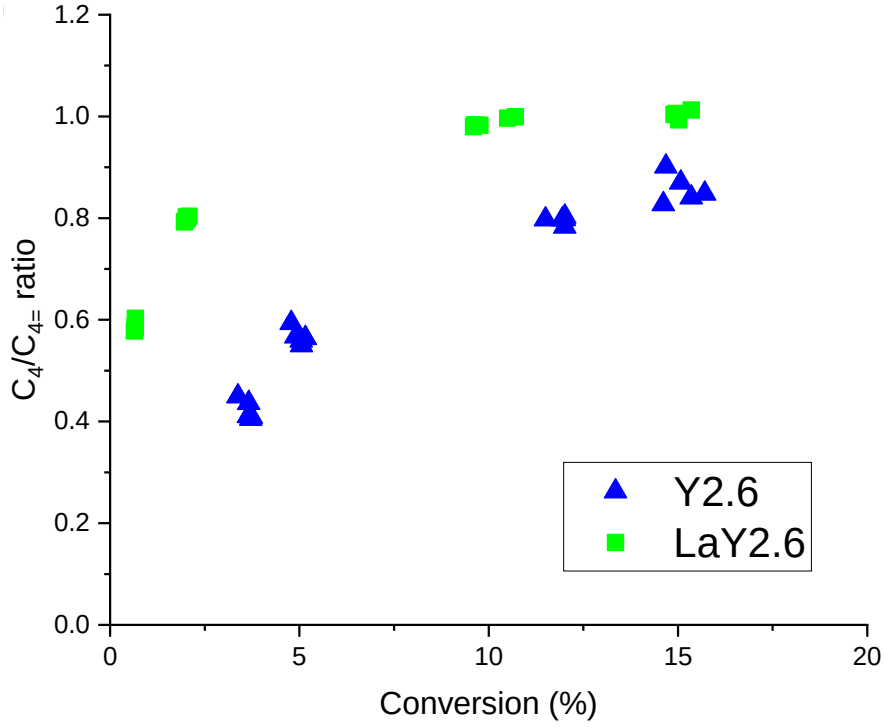

Figure 12. C4/C4= ratio of Y2.6 (▲) and LaY2.6 (■) at various catalytic conversions. Reaction conditions: continuous flow reactor at 2.4 kPa of isooctane partial pressure, 80 mL/min of carrier gas flow, 400ºC, 1 atm. The conversion was varied by changing the catalyst mass, 10-75mg.

Figure 13 shows the ternary plots for the parent zeolite (Y2.6) and the La-exchanged zeolite (LaY2.6) at various isooctane conversions in a similar overall conversion range (0-20%) for the two catalysts. The conversion was varied by varying catalyst mass and time on stream. The plot clearly illustrates that the incorporation of La into the Y2.6 zeolite enhances the hydrogen transfer activity while simultaneously diminishing the high protolytic cracking activity exhibited by the original zeolite. Furthermore, for a given percentage of hydrogen transfer activity, LaY2.6 slightly favors dehydrogenation over the protolytic cracking pathway when compared to Y2.6, indicating

an enhanced degree of dehydrogenation activity by the La species incorporated in the zeolite, as previously suggested [29, 102, 103]. When evaluating the catalytic pathways as a function of conversion at different masses, both catalysts appear to increase the hydrogen transfer distribution, while lowering protolytic cracking as the conversion increases. This behavior is due to the bimolecular nature of hydrogen transfer between the gas phase isooctane and the surface isobutoxide. At higher catalytic conversion, the isobutoxide coverage will be higher due to a higher concentration of isobutene formed from subsequent reactions [42]. This will then result in an increased hydrogen transfer activity. Additionally, as the TOS increases, the distribution towards protolytic cracking increases while hydrogen transfer decreases. This behavior was observed for both catalysts. This is most likely due to the increasing amount of coke buildup inside the catalyst that causes a loss in the density of Bronsted acid sites. The hydrogen transfer activity will decrease since both higher acid density [66, 100] and closer site proximity [105] have been reported to improve hydrogen transfer activity.

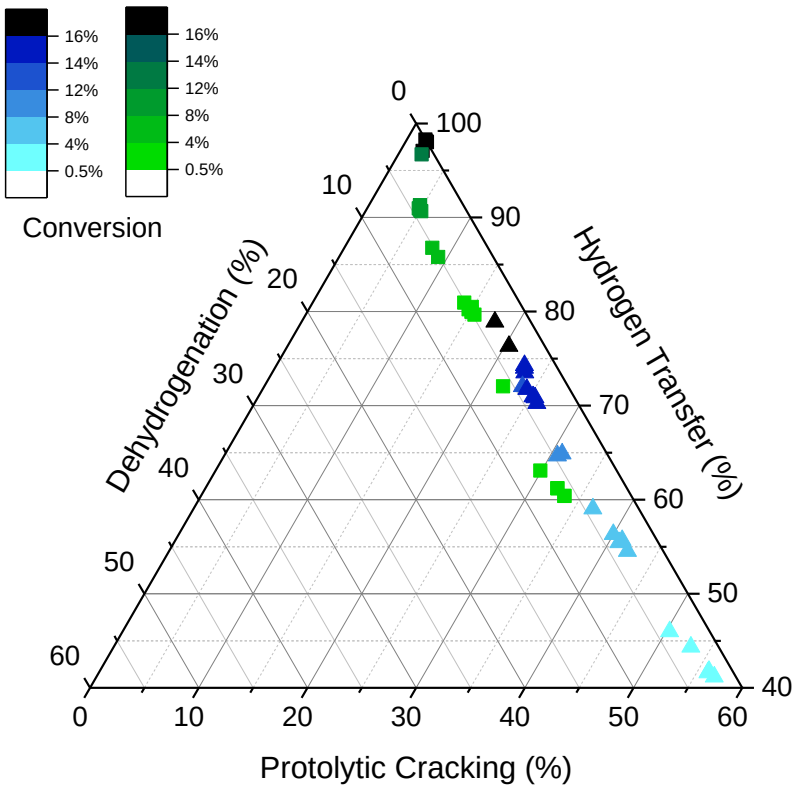

Figure 13 Ternary plot of Y2.6 (▲) and LaY2.6 (■) at various catalytic conversions. Reaction conditions: continuous flow reactor at 2.4 kPa of isooctane partial pressure, 80 mL/min of carrier gas flow, 400ºC, 1 atm. The conversion was varied by changing the catalyst mass, 10-75mg, and time on stream, 15-135 mins.

It is important to compare the absolute turnover frequencies of HT, PC and DH to determine whether the presence of La decreases PC or increases HT, or both. **Figure 14 A, B and C** compare the TOF of the three reactions pathways on the parent zeolite (Y2.6) and the La-exchanged zeolite (LaY2.6), as a function of isooctane conversion. The plots indicate that the incorporation of La into the Y2.6 zeolite enhances the intrinsic rate of hydrogen transfer and simultaneously diminishes the high protolytic cracking activity exhibited by the original zeolite. It has been reported that the presence of hydroxylated lanthanum species in the supercage polarizes the incoming branched alkane, resulting in a better stabilization of the transition state during the hydrogen transfer step between the surface carbenium ion and the gas-phase isooctane [29], which could explain the observed HT rate enhancement. Another explanation could be the higher BAS

density exhibited by the La-containing zeolite (see Table 3), as proposed by Sanchez-Castillo et al [100].

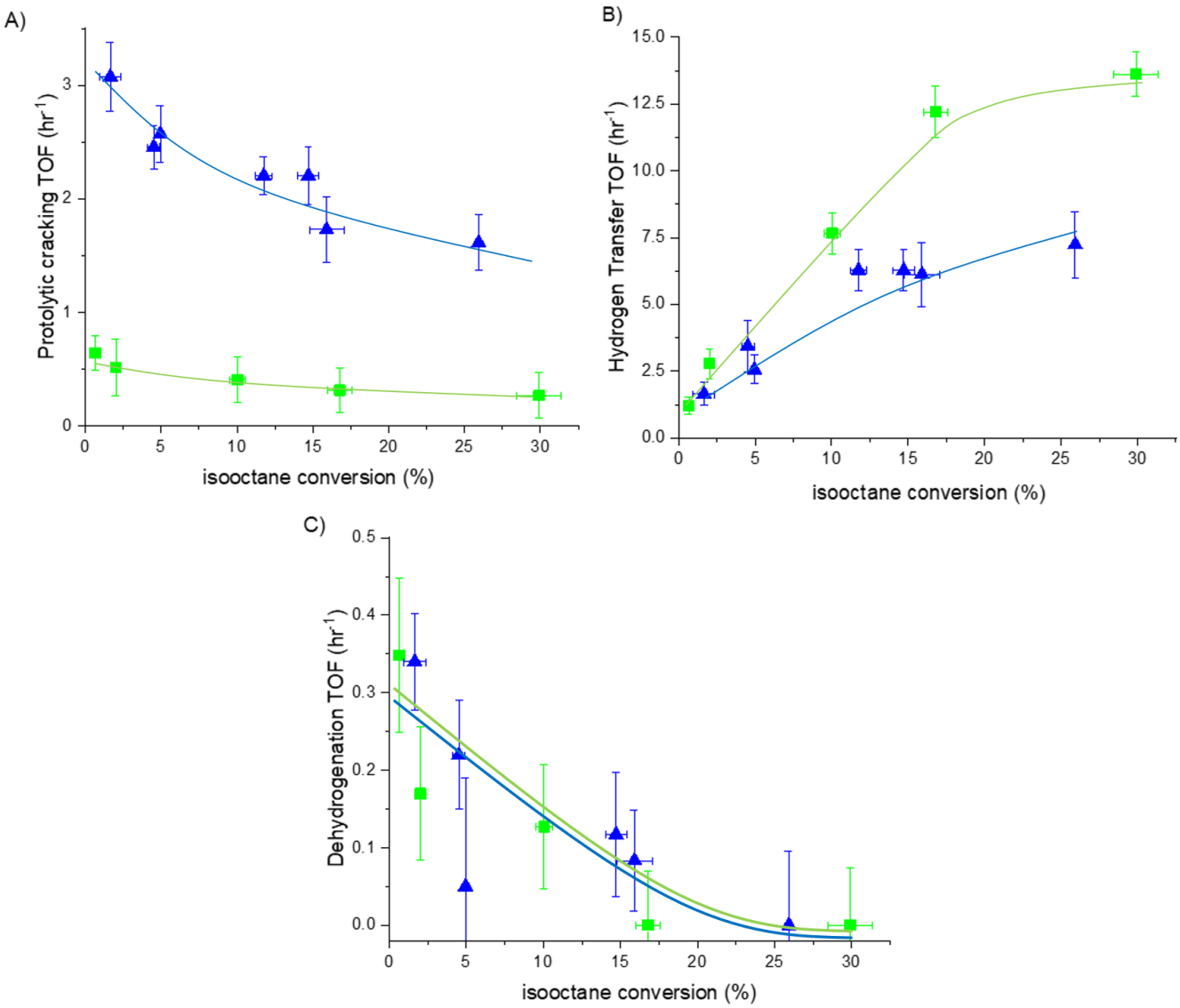

Figure 14. Turnover frequency (TOF) of Y2.6 (▲) and LaY2.6 (■) at various isooctane conversion. A) protolytic cracking, B) hydrogen transfer, C) dehydrogenation. Reaction conditions: continuous flow reactor at 2.4 kPa of isooctane partial pressure, 80 mL/min of carrier gas flow, 400ºC, 1 atm. The isooctane conversion was varied by changing the catalyst mass, 10-150 mg.

To further investigate the shifts in the distribution of protolytic cracking and hydrogen transfer with the presence of La, we conducted further runs at various isooctane partial pressures. The

results are summarized on **Figure 15, Figure 16**, and **Figure 17** for isooctane cracking over Y2.6 and LaY2.6. These figures reveal key trends regarding the influence of La in Y2.6 on isooctane cracking. It is observed that LaY2.6 exhibits a high percentage of hydrogen transfer at high partial pressures, while Y2.6 maintains a significant protolytic cracking selectivity.

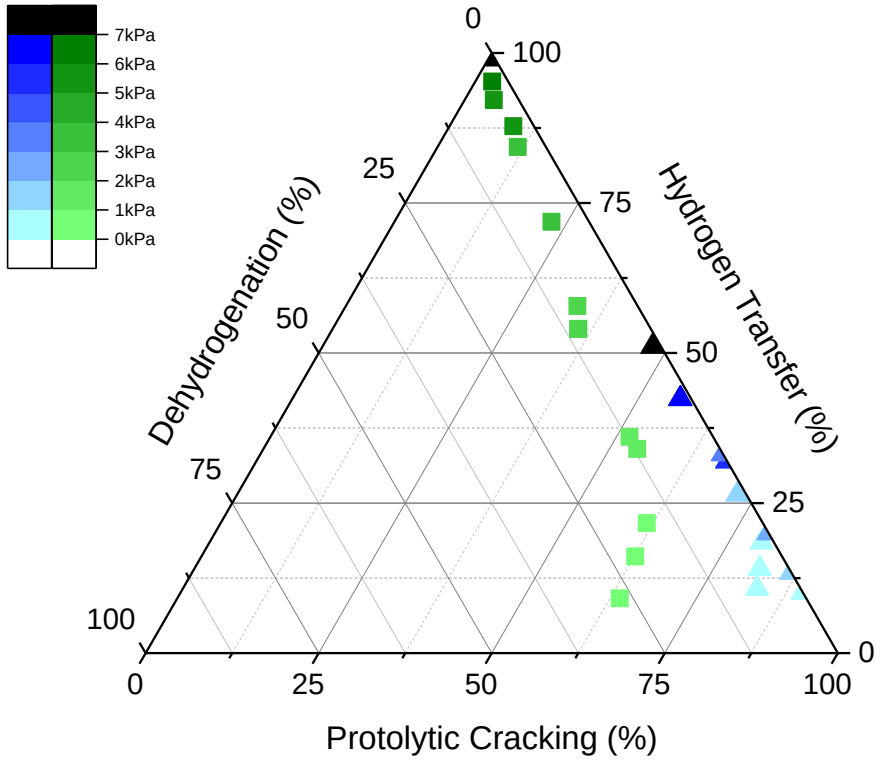

Figure 15. Isooctane cracking over Y2.6 and LaY2.6 at various isooctane partial pressure. Y2.6 (▲) ternary plot; B) LaY2.6 (■) ternary plot. Reaction conditions: continuous flow reactor at 0.3-7.2 kPa of isooctane partial pressure, 30 mg catalyst, 80 mL/min of carrier gas flow, 400ºC, 1 atm.

Figure 16A, B and C compare the three turnover frequencies, based on measured density of Bronsted acid on the parent zeolite (Y2.6) and the La-exchanged zeolite (LaY2.6), as a function isooctane partial pressure. For the whole partial pressure region, it seems that the additional of lanthanum enhances dehydrogenation activity while diminishing protolytic cracking activity (**Figure 9 and 10**). Interestingly, the enhancement in hydrogen transfer activity appears to be a lot more significant in the higher partial pressure region, when compared to protolytic cracking and

dehydrogenation. To further understand this behavior, **Figure 10** shows the plot of the natural log of isooctane cracking rate versus the natural log of isooctane partial pressure, which can be used to obtain the reaction orders on the two partial pressure regions.

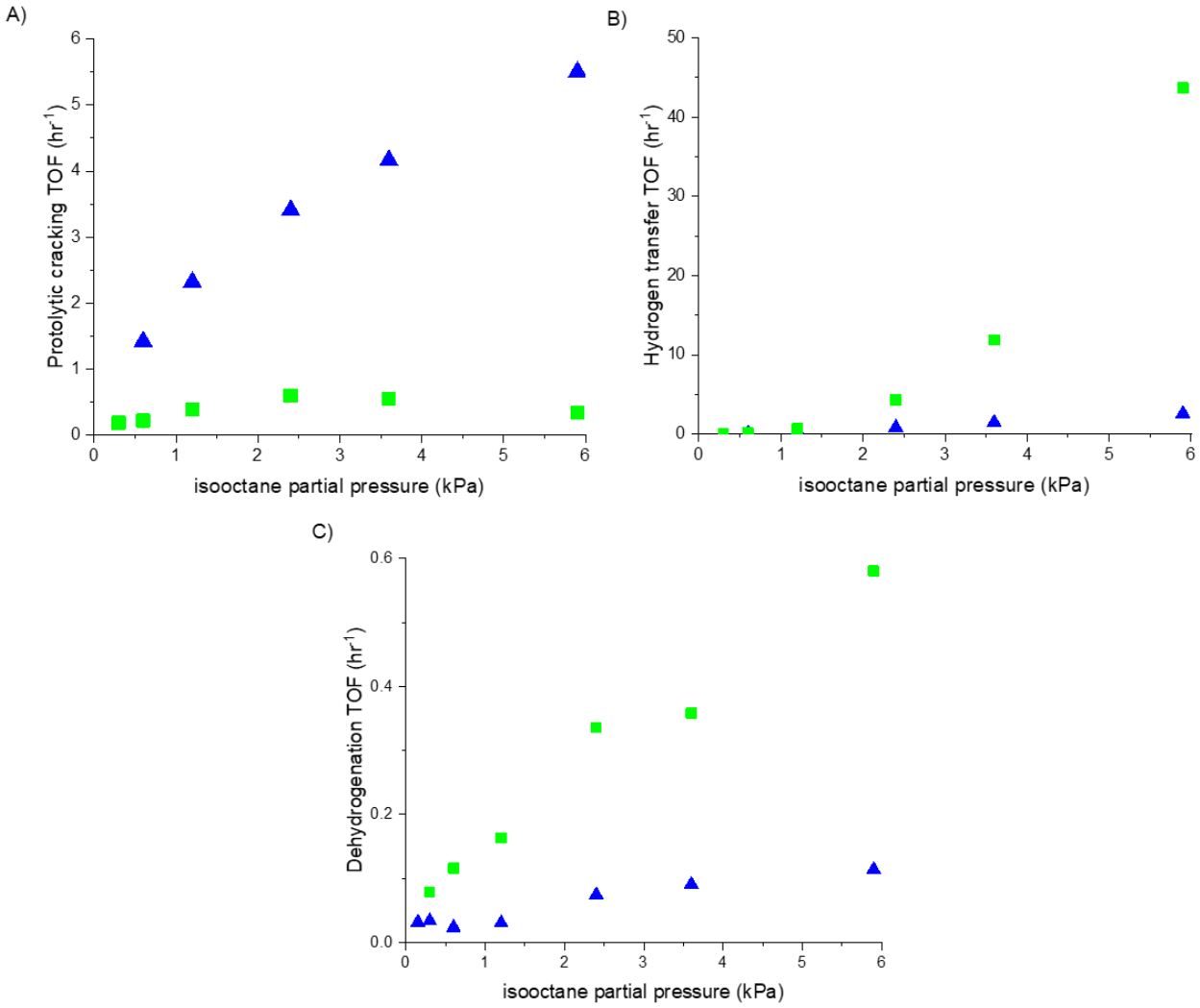

Figure 16. Turnover frequencies (TOF) of Y2.6 (▲) and LaY2.6 (■) at various isooctane partial pressure. A) protolytic cracking, B) hydrogen transfer, C) dehydrogenation. Reaction conditions: continuous flow reactor at 0.3-7.2 kPa of isooctane partial pressure, 30 mg catalyst, 80 mL/min of carrier gas flow, 400ºC, 1 atm.

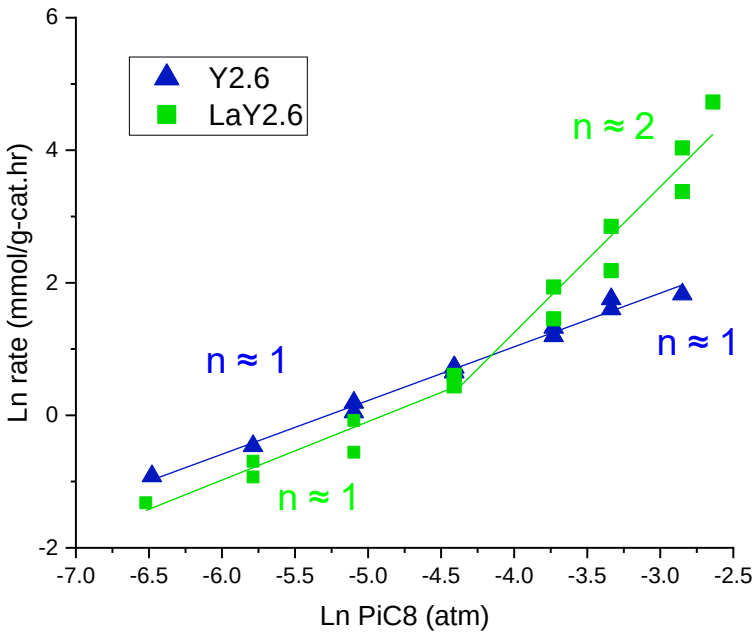

Figure 17. Natural log of overall isooctane cracking rate versus natural log of isooctane partial pressure. Reaction conditions: continuous flow reactor at 0.3-7.2 kPa of isooctane partial pressure, 30 mg catalyst, 80 mL/min of carrier gas flow, 400ºC, 1 atm. While the observed reaction order is about 1 for the parent Y2.6 zeolite in the entire range, the LaY2.6 sample exhibits two regimes, first order at low partial pressures and second order at high partial pressures.

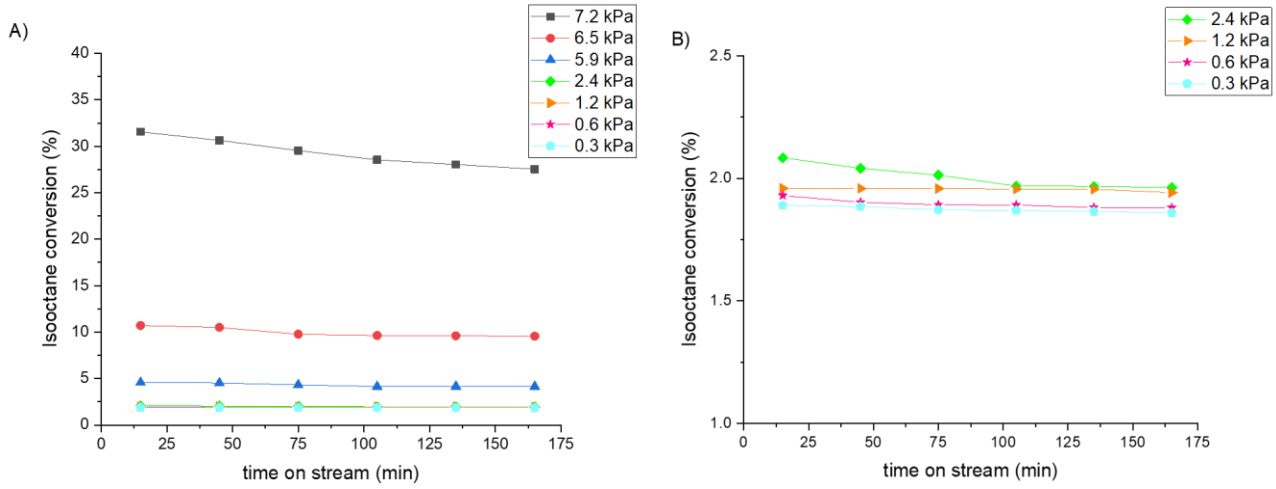

Figure 18. Isooctane conversion as a function of time on stream over LaY2.6 at A) varying isooctane partial pressure and B) first order partial pressure region. Reaction conditions: continuous flow reactor, 80 mL/min of carrier gas flow, 400ºC, 1 atm, 50mg.

As shown in **Figure 17**, the reaction order differs between the two catalysts: Y2.6 shows a constant first order, whereas LaY2.6 exhibits a transition from first order at low partial pressures to second order at high partial pressures. At high partial pressure, isooctane cracking over LaY2.6

follows a second order, bimolecular hydrogen transfer reaction, while Y2.6 remains first order, reflecting a predominant monomolecular protolytic cracking pathway. We must note that fast deactivation in catalytic cracking has been shown to yield falsified reaction orders, for example increasing apparent orders [106]. However, we have shown here that in our conditions, even at high partial pressure, the isooctane cracking activity for LaY2.6 is stable (**Figure 18**); thus, the change in observed order is not due to catalyst deactivation, but rather the intrinsic kinetics. At low partial pressures, both catalysts demonstrate first order kinetics, indicating the dominant monomolecular reactions. Interestingly, in this range, LaY2.6 favors dehydrogenation while Y2.6 favors protolytic cracking. Additional experiments with various lanthanum loadings in Y30 zeolites further clarify the role of lanthanum in enhancing the dehydrogenation rate, as depicted in **Figure 19**.

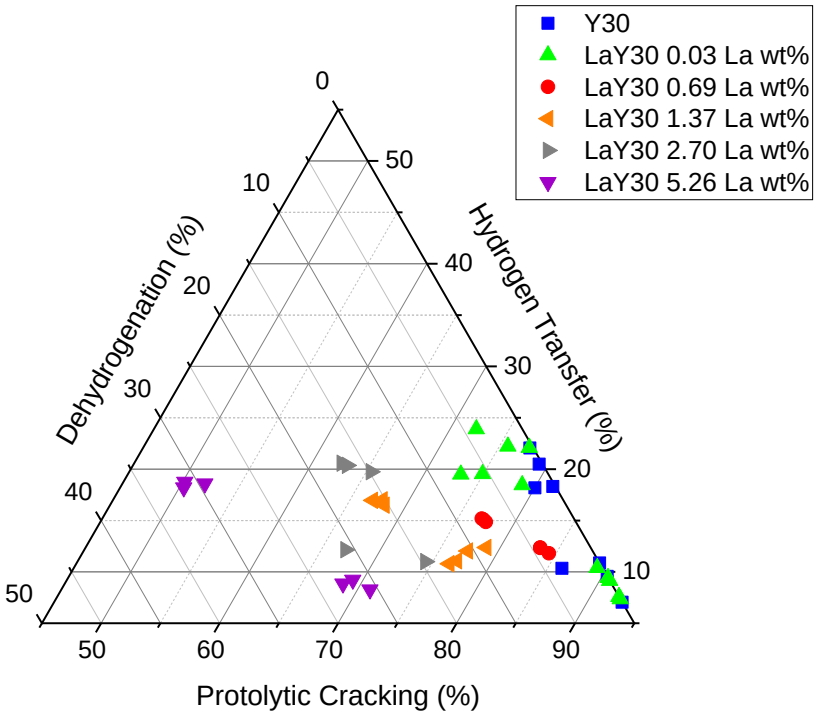

Figure 19. Ternary plot of isooctane cracking over Y30 zeolites with various lanthanum loadings and isooctane conversion. Reaction conditions: continuous flow reactor at 2.4 kPa of isooctane partial pressure, 80 mL/min of carrier gas flow, 20-120 mg catalyst, 400ºC, 1atm. All reactions are below 3% isooctane conversion to minimize sequential reactions.

The Y30 zeolite was chosen as a parent zeolite to study the various La loadings due to the lower Bronsted acid site density to maximize monomolecular reactions and better compare the predominance of protolytic cracking or dehydrogenation pathways under conditions of low hydrogen transfer activity. As shown in **Figure 19**, the addition of La into the zeolites increases the percentage of dehydrogenation, while decreases the protolytic cracking. The enhancement in the dehydrogenation pathway appears to increase with the La loading. Since these zeolites are impregnated samples, the observed enhancement in dehydrogenation activity may be due to the presence of occluded lanthanum oxide clusters, rather than exchanged isolated lanthanum cations. These species become dominant at higher lanthanum loadings, which may be responsible for the increased isooctane dehydrogenation rates. This is a remarkable result revealing how this simple probe molecule can be used to discriminate a catalyst's ability to carry out competing monomolecular reactions such as protolytic cracking and dehydrogenation. By modifying partial pressures of reactants, one can also discriminate the ability to truly enhance hydride transfer from simply decreasing rates of protolytic cracking, which are difficult to distinguish by simply contrasting olefin to paraffin ratios at isoconversion. This makes this reaction a particularly compelling probe reaction to assess catalyst performance for these important reactions.

2.5 Conclusion

Isooctane cracking over Bronsted acid sites provides insight into catalyst characteristics related to hydrogen transfer, protolytic cracking, and dehydrogenation. This is possible by the unique characteristics of the isooctane molecule, containing both ternary and quaternary carbons that allow appreciable rates of the three competing reaction pathways under moderate reaction conditions. By plotting C_4 alkane selectivity against C_1 selectivity, the experimental data align well with the proposed reaction pathways. Most data points from different catalysts and experimental conditions fall along the line derived from the stoichiometry of the proposed reactions, which reinforces the validity of the proposed pathways. The high protolytic cracking rate in the parent Y15 is attributed to the presence of synergistic sites, which are prevalent in most zeolites. Analyzing the distribution of protolytic cracking, hydrogen transfer, and dehydrogenation on a ternary diagram provides a concise understanding of catalyst characteristics and the impact of reaction conditions. Finally, we have shown that isooctane cracking can be used to understand and quantify the role of lanthanum incorporation into zeolite Y by measuring the distribution of hydrogen transfer, protolytic cracking, and dehydrogenation reactions.

Chapter 3

Lanthanum-Incorporated Zeolite Y: Impact of La on Physical and Acid Properties of the zeolite and its Influence on Isooctane Cracking Performance

The incorporation of Lanthanum (La) as an additive in zeolite Y has been widely employed in FCC catalysts. It has led to significant progress in FCC performance, by improving product selectivity, catalyst stability, and catalyst intrinsic activity. However, the exact role of La in contributing to this improvement is still a matter of extensive investigation. In this work, the impact of La incorporation on the physical and acidic properties of the parent zeolite and its effect on isooctane cracking performance was investigated. A series of Y zeolites with various La loadings was synthesized via ion-exchange at various $La(NO)_3$ concentration and exchange number. A small amount of La was found to significantly improve the structural integrity of the Y zeolite. The presence of lanthanum inside the zeolite structure potentially increases the activation barrier for water attack at high temperature as well as ambient conditions, providing additional stability. The addition of La also increases the Bronsted acid density of the zeolite, by retaining the original Bronsted sites as well as introducing new Bronsted sites in the form of La-OH. During the isooctane cracking reaction, only a small amount of La required to increase the protolytic cracking activation energy, as La is preferentially titrating the synergistic sites due to the presence of EFAl and/or paired sites. On the other hand, La improve the intrinsic hydrogen transfer rate during isooctane cracking by increasing the Bronsted acid density of the zeolites. This work provides a deeper understanding on La impacts on zeolite Y, offering insights for a better catalyst synthesis for hydrocarbon transformation and FCC reactions.

This work is a working manuscript

3.5 Introduction

Fluid Catalytic Cracking (FCC) has been one of the most important processes in oil refineries, key in producing valuable products and chemicals. The process transforms heavy feed such as crude oil into lighter products, including gasoline, liquified petroleum gas (LPG), diesels, and olefins for various purposes such as transportation fuels and chemical feedstocks [13, 26, 72]. With the rise in efforts of CO_2 reduction and alternative feedstocks, a better understanding and continuous improvement in the FCC processes will always be key challenges. Striking the right balance between product octane number, catalyst activity, and coking rates is essential for an FCC unit. Acid zeolites have been the key catalyst in FCC processes, particularly zeolite Y, due to high tunability and controllable properties that allow various flexibilities in designing the catalyst to achieve the desired balance criteria. One of the various ways in modifying zeolite Y is the incorporation of rare-earth (RE) metals, such as Lanthanum (La) and Cerium (Ce). This modification has led to a substantial improvement in the FCC process, as it improves the activity, selectivity and stability of the catalyst. Many works have explored the role of La incorporation into zeolite Y and USY. The universally accepted role of La in zeolite Y is to improve the zeolite stability against harsh hydrothermal conditions [27, 28, 32, 100, 104, 107], which is an important feature for FCC catalysts as they are exposed to high temperature steam during the regeneration process that can cause framework dealumination. The area that remains controversial is the impact of La on the acid modifications on the parent Y zeolite. For instance, several works have found that the addition of La increases the total Bronsted acid density of the zeolite. However, the precise nature of these additional Bronsted sites remains the subject of extensive investigation. Dumesic et al. suggested that the increase in Bronsted acids is attributed to La's ability to retain the original Bronsted acids during high-temperature treatment [100]. Conversely, Lercher et al. argue that these additional sites are formed due to the presence of La-OH species [29, 67, 102]. Additionally, other

studies have observed changes in Bronsted acid strength, indicating that the incorporation of La leads to a higher relative distribution of acid strength [104, 108-110]. Consequently, more Bronsted sites become active, enhancing their participation in catalytic reactions. On the other hand, some works argued that La reduces the Bronsted acid density and Bronsted acid strength, resulting in a more stable catalyst against coking during hydrocarbon transformation processes [32, 111]. Additionally, the addition of La has shown to have a pronounced improvement in hydrogen transfer ability. This improvement is primarily attributed to the strong correlation of this reaction with the physical and acid properties of the zeolite.

In our recent work, we have established the uses of isooctane cracking as a reaction probe that can be used to investigate the catalyst performance in performing protolytic cracking, hydrogen transfer, and dehydrogenation. We showed that La-incorporated Y enhances both hydrogen transfer and dehydrogenation pathways. Thus, this work aims to characterize the La incorporated Y zeolites and understand the effects of La addition, at different loading, on the physical and acid properties of the zeolite. From these results, this work attempt to understand and explain the isooctane cracking performance of LaY, and its ability in suppressing protolytic cracking and enhancing hydrogen transfer activity.

3.7 Experimental and Methodologies

3.7.2 Materials and Catalysts Synthesis.

The parent Y zeolite that was used for all samples in this study has a Si/Al ratio of 2.6 (CBV 300), obtained from Zeolyst International. Ammonium nitrate, NH_4NO_3 (>99%), Lanthanum(III) nitrate hexahydrate (99.999% trace metals basis) were obtained from Sigma-Aldrich, and were used directly. Each sample used in this study undergoes a series of modifications, starting with CBV300 as the initial material. **Table 4** illustrates the naming conventions that indicate the modification history of the parent zeolite. For instance, in synthesizing sample 1N1X1C, CBV300 undergoes steps 1N, 1X, and 1C in sequence. **Table 5** shows the simplified name for some of the samples. These samples were used extensively for most of the characterizations and catalytic reactions. The naming notations are mostly applicable to XRD study at different stages of synthesis (**Figure 23**)

Table 4. Zeolite synthesis step and history notation

Notation	Synthesis step/history
1N	Ion exchanged with 0.1 M of ammonium nitrate, NH_4NO_3 solution at room temperature for 24 hours to ensure that starting zeolite is in NH_4-form [112]. The solids were then washed with excess DI water, filtered, and dried under vacuum oven at 80 C, overnight.
1C	Calcination of the sample under constant, 150 ml/min of synthetic air, using the following temperature ramping program: 5C/min to 90C, holds at 90C for 1 hour, increase to

	350C at 0.5/min, increase to 550C at 2C/min, and hold at 550C for 4 hours
αX	Ion exchanged with 0. **α** M of lanthanum nitrate, $La(NO_3)_3$ solution at 80 C for 1 hour. The solids were then washed with excess DI water, filtered, and dried under vacuum oven at 80 C, overnight.

Table 5. Simplified name of some of the samples used in this work.

Sample	Simplified name
1N	NH_4-Y
1N1C	HY
1N0.1X1C	0.1LaY
1N0.5X1C	0.5LaY
1N1X1C	1.0LaY
1N1X1C1X1C	1.0+1.0LaY

3.7.3 Catalyst Characterizations

3.7.3.1 Elemental analysis

The elemental analysis to quantify Si, Al, La weight % in each sample was provided by Galbraith Laboratories (Knoxville, TN) using GLI Procedure ME-70.

3.7.3.3 BET pore analysis

The BET surface area and pore analysis to quantify the macropore and micropore of the samples was provided by MSE Analytical (Tucson, AZ) using Micrometrics ASAP 2020. N_2 physisorption was carried out at -198 ºC, and the sample was degassed at 300 ºC for 3 hours under a vacuum to remove adsorbed water. The pore size distribution was calculated using Horvath-Kawazoe (HK) method for the micropore region and Barrett-Joyner-Halenda (BJH) method for the mesopore region.

3.7.3.4 Isopropylamine Temperature Programmed Reaction/Decomposition (IPA-TPD)

Temperature-programmed decomposition (TPD) of adsorbed isopropylamine was used to quantify the density of BAS. In each TPD measurement, 50 mg of catalyst was pretreated mirroring the treatments employed in reaction runs. After pretreatment, the catalyst was cooled to 100 °C under 20 sccm of He and exposed to ten consecutive 2 μL pulses of IPA. After flushing under He for 12 h at 100 °C to remove weakly adsorbed IPA, a 10 °C/min linear heating ramp was applied up to 600 °C. The desorbed products were analyzed and quantified on a Microvision Plus MS, scanning over a 1–60 m/z range at a speed of 26 cycles/min. Via Hoffman elimination, each Bronsted acid site will decompose one isopropylamine into ammonia and propylene. Thus, the amount of propylene evolved is equal to the amount of Bronsted acid within the catalyst bed. To quantify the BAS density, the propylene signal (m/z = 41) was calibrated with 500 μL propylene pulses.

3.7.3.5 Ammonia Temperature Programmed Desorption, NH_3-TPD.

Temperature-programmed desorption (TPD) of adsorbed ammonia was used to quantify the total acid density. In each TPD measurement, 50 mg of catalyst was pretreated mirroring the

treatments employed in reaction runs. After pretreatment, the catalyst was cooled to 100 °C, and exposed to 20 sccm of 2% NH_3 in He. After flushing under He for 12 h at 100 °C to remove weakly adsorbed NH_3 , a 10 °C/min linear heating ramp was applied up to 800 °C. The desorbed products were analyzed and quantified on a Microvision Plus MS, where ammonia (m/z=16) was tracked. To quantify the BAS density, the ammonia signal was calibrated with 500 μL 2% NH_3 in He pulses.

3.7.3.6 X-Ray Diffraction (XRD).

Powder X-ray diffraction (XRD) was performed on a Rigaku Ultima IV diffractometer (Cu Kα radiation, λ =1.5406 Å) in the 2θ range of 5–70° under an operating voltage of 40 kV and a current of 44 mA. Each sample was pretreated in a vacuum oven at 80 °C to remove moisture.

3.7.3.7 FTIR Spectroscopy.

In-situ diffuse reflectance infrared Fourier transform spectroscopy (DRIFTS) was performed in a high-temperature cell (Harrick Scientific). The in-situ cell was mounted inside a Praying Mantis diffuse reflectance accessory (Harrick Scientific) paired with a Thermo Scientific Nicolet iS10 FTIR spectrometer equipped with a HgCdTe (MCT) detector. Potassium bromide, KBr, was used as a background scan for all samples. For a given catalyst analysis, a mixture of 30 mg catalyst and 150 mg KBR was prepared by thoroughly grided them in a crucible. Then, approximately 100 mg of the grinded mixture was loaded into the cell and pretreated at 300 ºC for 1 hour to remove adsorbed water. Then, the spectra for each sample were collected at 300 ºC. All spectra were collected with a resolution of 4 cm^{-1} by merging 64 scans to minimize spectral noise. Measurements were made while purging the FTIR with dry He gas to remove desorbed water and to minimize atmospheric gas interference with the beam path. The purge line was connected to a column of Drierite as a water adsorber.

3.7.3.8 Isooctane heat of adsorption calorimetry.

The heat of adsorption of isooctane over HY and 1.0 LaY was measured using a Setaram C80 Calvet calorimeter, coupled with Micromeritics ASAP 2020 as a dosing system. For these analyses, 300 mg of catalyst were utilized. The sample underwent vacuum heating up to 300°C at a rate of 2.5°C/min and was maintained for 3 hours on the ASAP 2020 degas ports. Subsequently, the sample was heated at 2.5°C/min to the analysis temperature of 100°C. The heat flow signal was stabilized at the analysis temperature for approximately 3 hours.

3.7.3.9 Catalytic Test

The catalyst ability in performing protolytic cracking, hydrogen transfer, and dehydrogenation was probed using isooctane cracking, which has been demonstrated in previous chapter. This work also utilized two different modes of introducing isooctane to the catalyst bed: continuous flow mode and micropulse mode. In a typical run, isooctane cracking was carried out in a gas-phase continuous flow reactor using N_2 as a carrier gas. The pelletized catalyst (0.25 mm- 0.40 mm) was loaded and pretreated at 300 ºC for 1 hour to remove adsorbed water under 100 mL/min of N_2 flow. The reactor was then heated to 400 ºC and was kept stabilizing for at least 1 hour. The isooctane partial pressure was kept at 2.7 kPa in a continuous flow mode. In investigating the activation energy of the catalysts in performing protolytic cracking and hydrogen transfer reactions, the reaction conditions are adjusted in order to maximize each reaction pathway. For protolytic cracking, the reaction was conducted in micropulse mode at 400-430 ºC, 5 mg catalyst, 0.56 kPa isooctane, and 100 ml/min N_2 carrier flow. As for hydrogen transfer, the reaction was conducted in continuous flow mode at 160-180 ºC, 5-12mg catalyst, 1.11 kPa of isooctane partial pressure, and 100 ml/min N_2 carrier flow.

3.8 Results

Table 6 shows the lanthanum loading for each catalyst, as well as the Si/Al and La/Al ratio from elemental analysis. It can be observed that the amount of La incorporated into the zeolite increases across the series of samples used in this study. Furthermore, the bulk Si/Al ratio also remains consistent, suggesting that minimal amount of Si or Al loss from the bulk zeolite sample during the exchange process. It is also noteworthy that the La/Al ratio increases with higher La loading, and the ratio does not exceed 1. This indicate that the lanthanum is introduced via ion exchange and well dispersed within the zeolites, assuming a maximum of 1:1 ratio to compensate for the negative charge of the Al center.

Table 6. Lanthanum loading and the bulk SI/Al ratio

	La weight%	**Si/Al**	**La/Al**
HY	-	2.68	-
0.1LaY	1.89%	2.66	0.04
0.5LaY	8.46%	2.65	0.17
1.0LaY	10.30%	2.63	0.21
1.0 + 1.0LaY	14.70%	2.77	0.33

3.8.2 Effects of La on the physical and structural properties of zeolite Y

Table 7 summarizes the effects of La addition via ion exchange on the surface area and the pore volume of the parent zeolite. When compared to the original NH_4-Y, La slightly reduces the pore volume, but not significant enough to conclude that the pore is being plugged by the lanthanum species. Interestingly, the addition of La retains most of the pore volume of the original NH_4-Y zeolite, while the pore volume for HY is reduced significantly, despite La ion exchange

process was carried at an elevated temperature. From the pore volume, the pore size distribution is mainly in the micropore region, which is expected for a low Si/Al ratio zeolite.

Table 7. BET surface area and pore volume of HY and LaY samples.

Sample	Surface Area (m^2/g)	Pore volume (cm^3/g)	Micropore volume (cm^3/g)	Mesopore volume [a] (cm^3/g)
NH_4-Y	804	0.333	0.297	0.036
HY	390	0.180	0.144	0.036
0.1 LaY	717	0.295	0.265	0.030
0.5 LaY	756	0.314	0.277	0.037
1.0 LaY	783	0.333	0.288	0.045
1.0 + 1.0 LaY	755	0.314	0.277	0.037

a) Calculated based on the difference between total pore volume and micropore volume

Figure 20A shows the nitrogen adsorption-desorption isotherms of the zeolite samples, indicating Type I isotherms, characteristic of a typical microporous material. However, a small hysteresis loop is present for all samples, indicating a minor fraction of mesopores, consistent with the findings in **Table 7**. **Figure 20B** shows the differential pore size distribution of the lanthanum incorporated zeolites using Horvath-Kawazoe method for the micropore region (< 1 nm) and Barrett-Joyner-Halenda for the mesopore region (>1 nm), to investigate the effects of La on the micropore distribution. For all samples, the range of the pore width distribution is typical of those CBV 300, where most of the samples are primarily in the microporosity range [113]. Additionally, the pore size distribution remains unchanged with varying amounts of La incorporated into the zeolites, despite the lanthanum loading being up to 10 wt%. The BET analysis results indicate that La is well dispersed within the zeolitic structure, with minimal formation of La clusters or

agglomerations. This is critical for minimizing mass transfer limitations associated with the presence of La clusters, especially with zeolites that are mainly in the micropore region.

To further elucidate the effect of La on the physical properties of zeolite Y, **Figure 21** shows the XRD patterns of the zeolite samples. Even after the inclusion of La into the zeolite, the samples retain the zeolitic characteristic peaks of the parent Y zeolite. Notably, no characteristic peaks corresponding to lanthanum phases appear in the XRD patterns of the La-modified zeolites,

indicating that La is well dispersed within the zeolite framework and no separate La phase exists. This finding is consistent with the BET results.

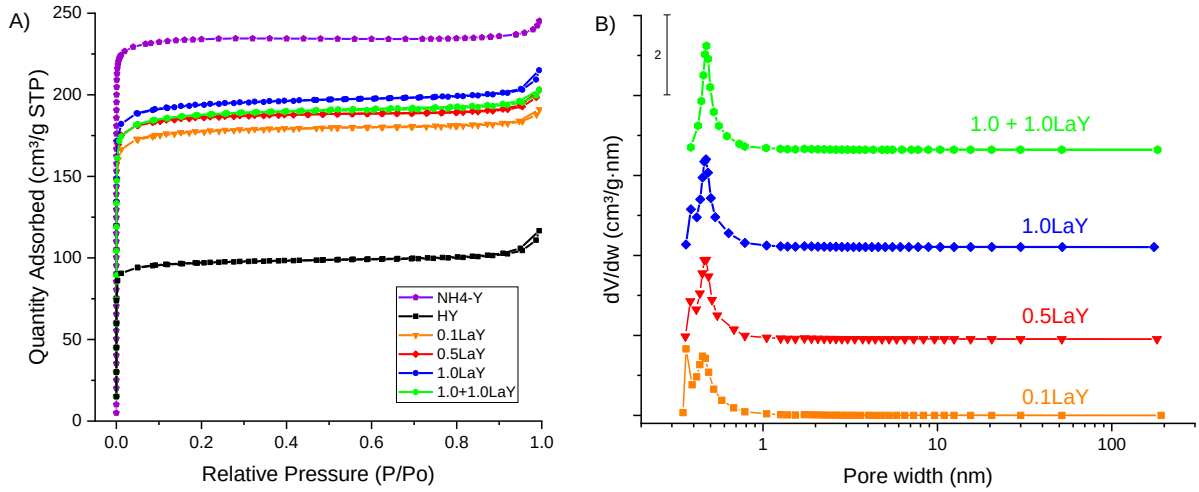

Figure 20. A) Nitrogen adsorption-desorption isotherms; B) the HK pore size distribution of the various La samples. Size <1.0 nm was calculated using HK method (micropore). Size >1.0 nm was calculated using BJH method (mesopore)

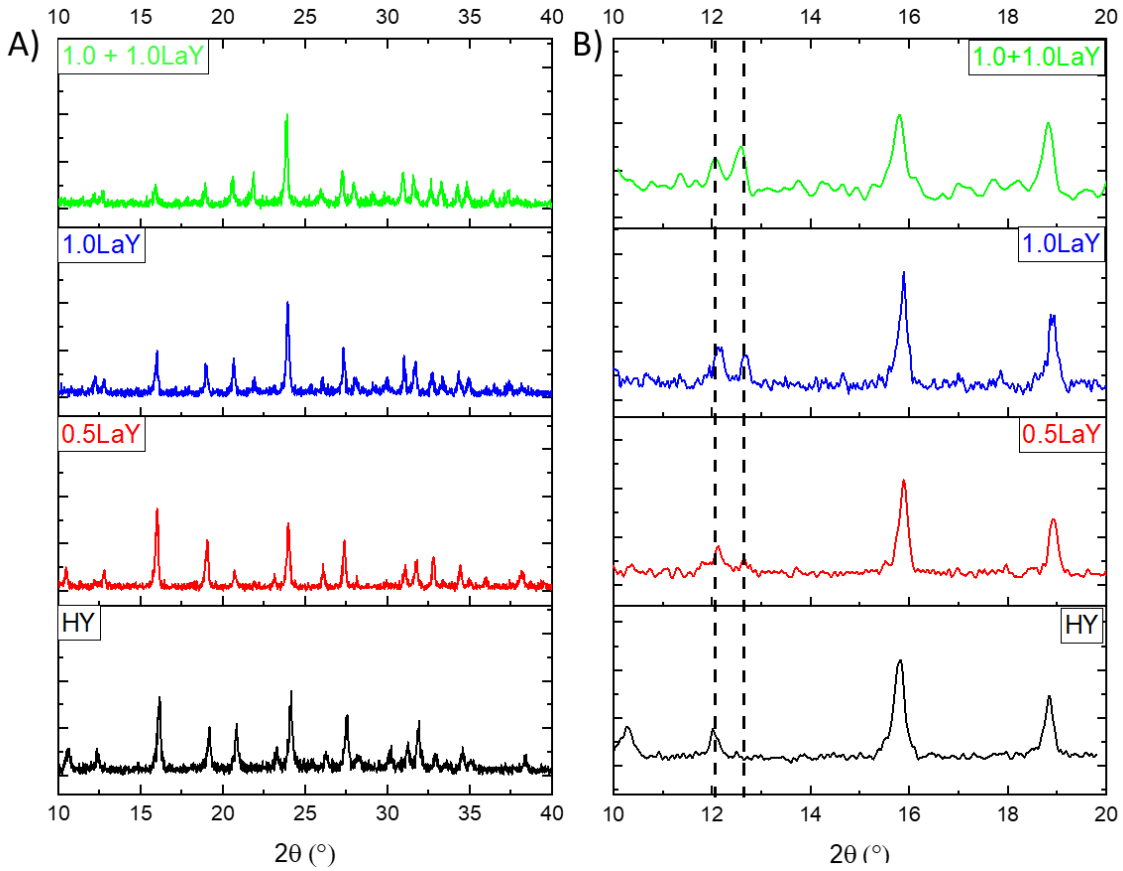

Figure 21. A) XRD patterns of 2θ between 10º and 40º for HY and LaY samples. B) Amplified XRD patterns between 10º and 20º for HY and LaY samples.

Figure 21B presents the X-ray diffraction (XRD) patterns of HY and LaY samples in the 10º to 20º range, focusing on two peaks of interest at 11.9º and 12.4º. Previous studies have identified these peaks as corresponding to the (311) and (222) planes, respectively, during the introduction of rare earth (RE) elements into Y zeolites [114-116]. The regular HY zeolite initially does not contain a (222) characteristic peak. With the introduction of La into the zeolite, the (222) peak emerges, indicating that this peak is caused by the La species that is present within the

zeolites. Interestingly, as the La loading increases, the relative intensity of the (311) peak decreases, while that of the (222) peak increases (**Figure 22**).

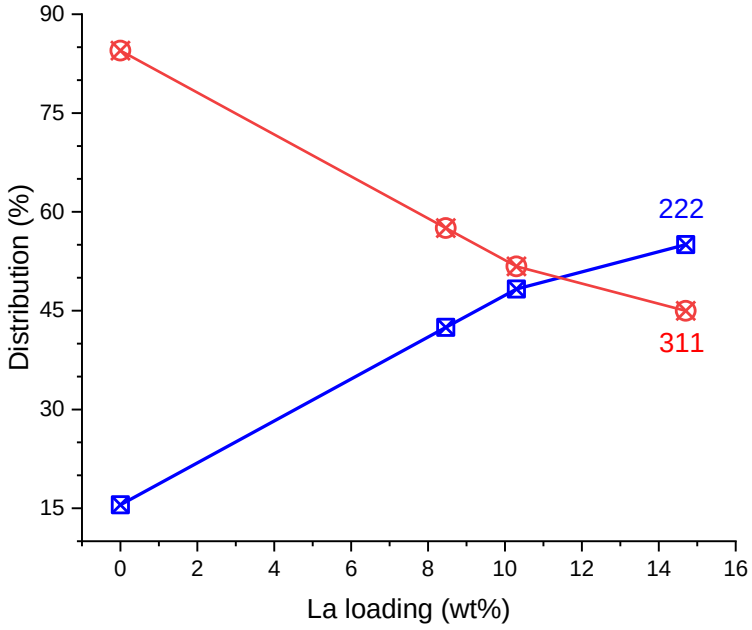

Figure 22. Percent distribution of (311) peak and (222) peak as a function of La loading

To further elucidate this relationship, **Figure 23** illustrates the XRD patterns of the 1.0 + 1.0 sample at each synthesis stage (ion exchange, calcination). Interestingly, for every ion exchange step, the (311) peak disappears completely indicating that the presence of the La species after the ion exchange process causes a complete destructive interference on the (311) peak. After the calcination step, the (311) peak reappears at a slightly lower peak intensity when compared to the 1N sample. During the second exchange, the (311) peak once again disappears, indicating that the La species within the zeolite prior to calcination causes this peak to disappear. After the second calcination, this peak reappears but at much lower intensity. This result is in complete agreement with the observation from Wang et al [114]. The possible explanation is after the ion exchange, the La species are primarily in the form hydrated La^{3+} cations, $[La(H_2O)_n]^{3+}$. During ion exchange, this La species is only allowed to exchange with the supercage sites, as the cation species is too

big to enter the much smaller sodalite cage and hexagonal prism. The presence of the $[La(H_2O)_n]^{3+}$ inside the supercage causes a destructive interference with the (311) peak. During calcination, the initial La species inside the supercage begins to dehydrate, resulting in a smaller La^{3+} species that is easier to migrate through the small six-membered ring windows and enter the sodalite cage [29-31]. This process resulted in the reduction in size of the bulky hydrated La^{3+} species inside the supercage, allowing the reemergence of the (311) peak [114]. Thus, the relative intensity of the (311) peak suggests the amount of La^{3+} species within the supercage. In the case of Ce in Y zeolite, other works have attempted to find a quantifiable relationship between the (311) peak and the (222) peak, suggesting that the ratio of the peak intensity can be used as an indicator of the relative ratio of Ce within the sodalite cage relative to supercage [115, 116]. However, this work suggests that using the ratio is not a straightforward indicator, as this work and the work from Wang et al. have shown that this ratio highly depends on the hydration state of the zeolites [114]. Rather, this

ratio may be a good indicator of La loading within the zeolites, as the presence of La generate the (222) peak and higher loading will further diminish the (311) peak intensity.

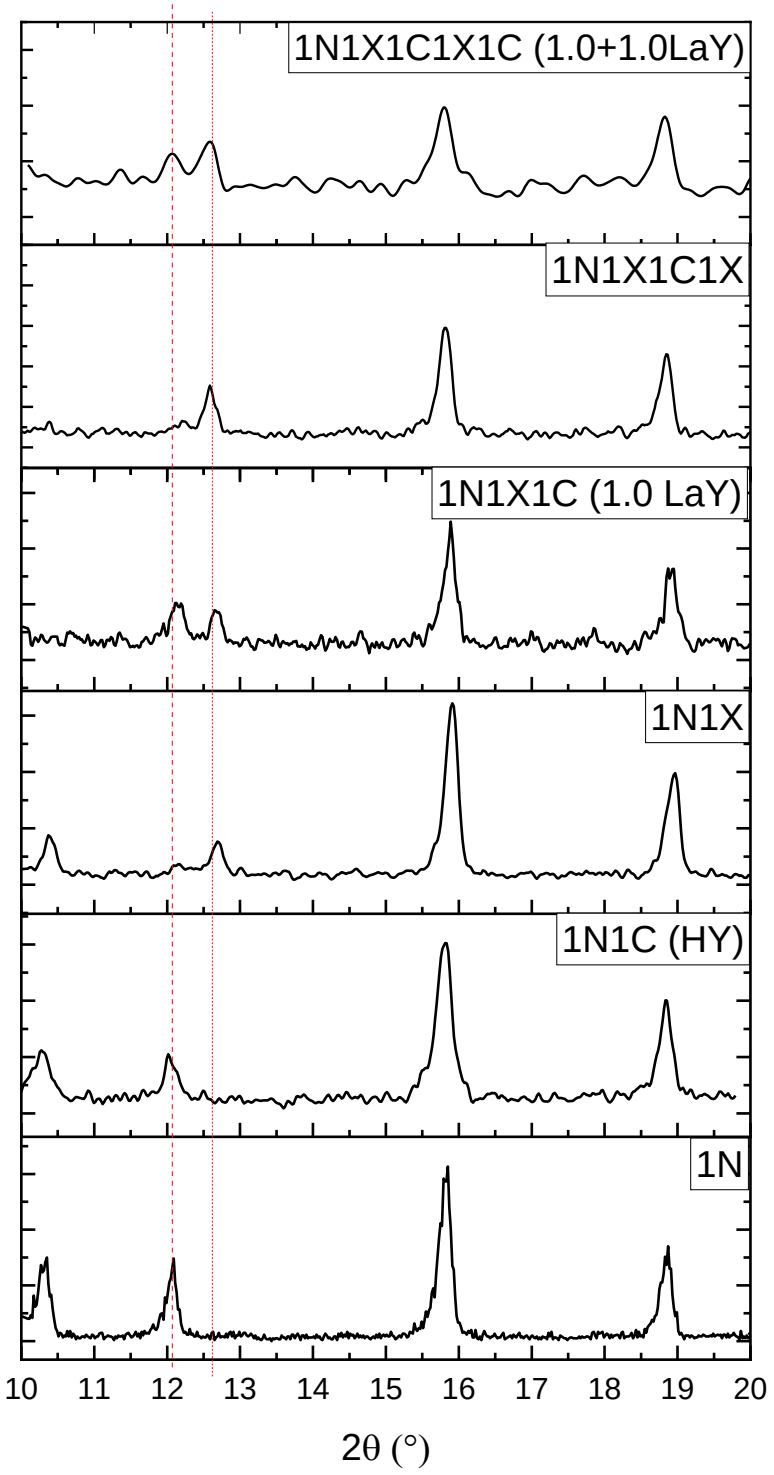

Figure 23. XRD patterns of LaY samples at varying stages of synthesis

3.8.3 Effects of La on the acid properties of zeolite Y

To assess the impact of La incorporation at various loadings on the acid properties of zeolite Y, NH_3-TPD and IPA-TPD were performed. NH_3-TPD provides information on the total acidity (Bronsted and Lewis acids), while IPA-TPD specifically elucidates the Bronsted acidity. **Figure 24** shows the desorption profiles from NH_3-TPD and IPA-TPD for the various zeolite samples. **Table 8** shows the total acid density, Bronsted acid density, and the fraction of Bronsted acid via IPA/NH_3-TPD and middle peak deconvolution of NH_3-TPD. There are three characteristic peaks from the NH3-TPD profile deconvolution. The first peak is centered around 180 ºC. This peak is associated with strongly physiosorbed ammonia or the extremely weak acid sites. The second peak, centered around 250-350 ºC, while the third peak is centered around 430 ºC. In the case of IPA-TPD, there are two characteristic peaks: one main peak centered around 350-365 ºC, and one small peak around 390 ºC, which is more prominent at higher La loadings.

Based on the NH_3-TPD and IPA-TPD profiles, several observations can potentially elucidate the impact of La on the acid properties of zeolite Y. First, the addition of La appears to suppress the high temperature peak in NH_3-TPD. This suggests that the addition of La into zeolite Y eliminates a specific type of acid site that are strongly bound with ammonia. Furthermore, considering there is only one main characteristic peak for all samples during IPA-TPD, this suggests that the high temperature peak in NH_3-TPD is not due to framework Bronsted acids. This is also indicated by the increase in Bronsted acid density as the La loading increases, while the high temperature peak of the NH_3-TPD is suppressed. This indicates that the addition of La into Y zeolite causes either the La species to titrate or eliminate these strong acid sites, which are not Bronsted in nature. Furthermore, the addition of La enhances intensity of both the middle peak in the NH_3-TPD, and the propylene peak in the IPA-TPD. When comparing the fraction of this peak

to the overall NH_3-TPD (**Table 8**), the middle peak correlates well with the fraction of Bronsted acid found from IPA-TPD. This implies that the middle peak from the NH3-TPD is directly related to the Bronsted acid peak from IPA-TPD. The addition of La increases the Bronsted acid density of the Y zeolite, and this enhancement is magnified with further La loading until a maximum density is achieved for 0.5LaY sample. **Figure 25** shows the total acid density and Bronsted acid density as a function of La loading.

A possible explanation is that the high temperature peak acid sites in NH_3-TPD are related to Lewis acids sites. As the amount of La increases, the amount of Lewis acids decreases and Bronsted acid increases. Bronsted acids is associated with the framework tetrahedral aluminum species, Si-OH-Al sites while Lewis acid is associated with the coordinatively unsaturated Al^{3+} ions, formed from the dehydration of a Bronsted site and removal of Al from the framework forming EFAl [117]. There are two possible roles of La. First, due to the compensation nature between Bronsted acid and Lewis acid in zeolites, the addition of La preserved the original Bronsted framework from dehydration and dealumination during high temperature treatment or excess moisture. As a result, the original Bronsted acid density is retained by preventing dealumination, resulting in a lower Lewis acid density. Another possibility is that La species titrates the Lewis acid sites, while simultaneously generating new Bronsted acid sites. This possibility is also supported by the new characteristic peak formed around 390 ºC during IPA-TPD, especially at higher La loadings, suggesting that La species is creating a new Bronsted site that can decompose IPA. The phenomenon of creating a new type of Bronsted acid sites is also observed in previous works, where the incorporation of various metals including Co, Zn and, Mo into H-ZSM5 zeolites created new characteristic peaks in the higher temperature region during IPA-TPD. [118, 119]. However, it is important to acknowledge that the high-temperature peak in

the NH_3-TPD may not strictly be due to Lewis acid sites. It is also possible that some of it is due to inaccessible Bronsted acid sites during IPA-TPD, since NH_3 is much smaller than IPA, allowing better access to sites inside the small sodalite cage.

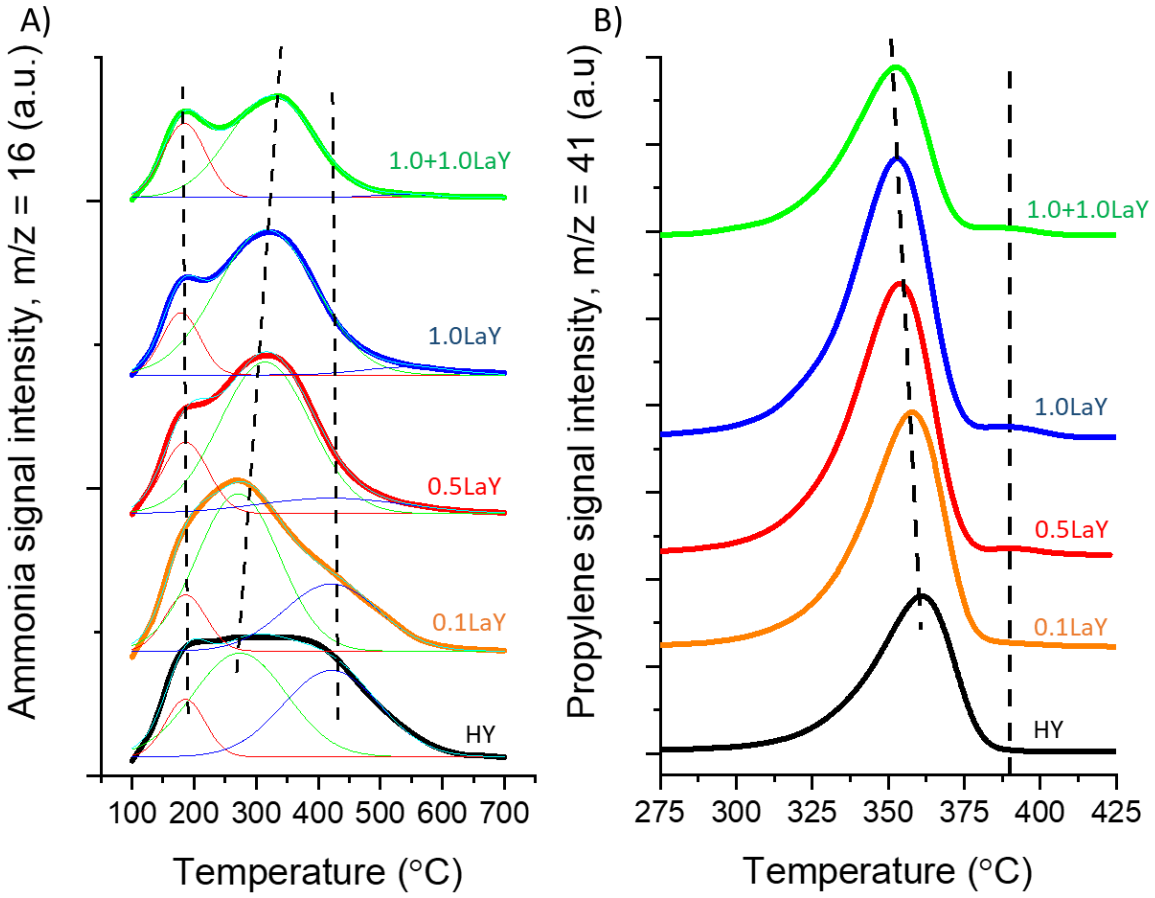

Figure 24. NH_3-TPD and IPA-TPD for all samples. A) Ammonia profiles from NH_3-TPD with peak deconvolution B) Propylene profiles from IPA-TPD

Table 8. Total acid density, Bronsted acid density, and the fraction of Bronsted acid density from NH3-TPD and IPA-TPD.

	Total acid density [a] (mmol/g)	Bronsted acid density [b] (mmol/g)	Fraction of Bronsted acid to total acid density	Fraction of middle peak from NH_3-TPD peak deconvolution
HY	1.81	0.79	0.44	0.48
0.1LaY	1.96	1.06	0.54	0.60
0.5LaY	1.70	1.38	0.81	0.85
1.0LaY	1.56	1.34	0.86	0.84
1.0 + 1.0LaY	1.17	0.91	0.78	0.72

a) From NH_3-TPD
b) From IPA-TPD

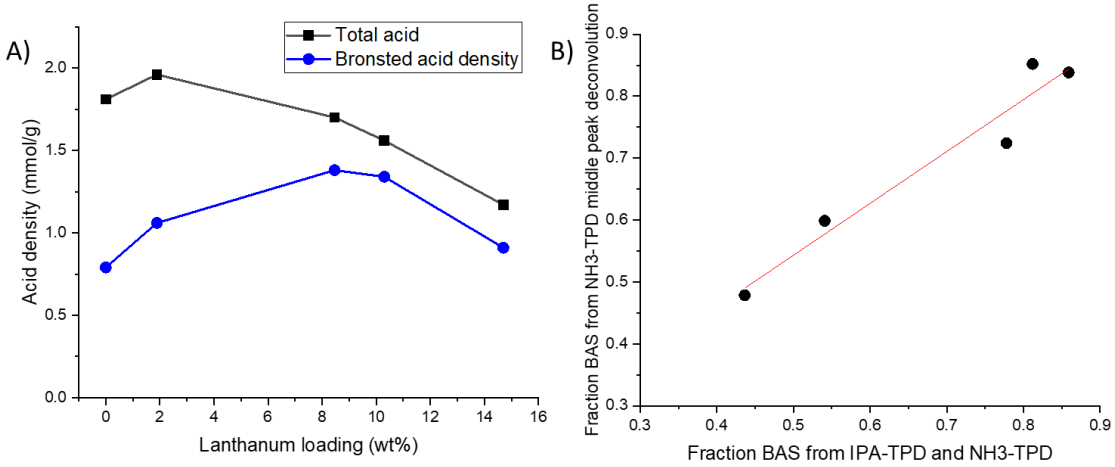

Figure 25. A) Total acid density and Bronsted acid density at various La loadings via NH_3-TPD and IPA-TPD. B) Fraction of the middle peak in NH_3-TPD versus fraction of Bronsted from IPA-TPD to total acid from NH_3-TPD

Additionally, the peak position of the Bronsted peak in both NH_3-TPD and IPA-TPD is shifted as the amount of La loading increases. In the case of NH_3-TPD, the Bronsted peak shifted to a higher temperature, while in IPA-TPD, the propyelene peak shifted to a lower temperature. Both results indicate that the strength of the Bronsted acids in the La modified zeolites is higher than the regular HY, and the strength appears to correlate well with the amount of La incorporated. The role of La modifying the strength of Bronsted has been highly debated in literature, where La

has been shown to increase, decrease, and retain the Bronsted acid strength [29, 32, 104, 110]. In this work, however, it is crucial to exercise caution when analyzing acid strength based solely on the peak position, as previous studies have demonstrated that adsorbate-adsorbate competition, adsorption energies at varying coverage, and subsequent readsorption can cause changes in the desorption peak temperature [120, 121].

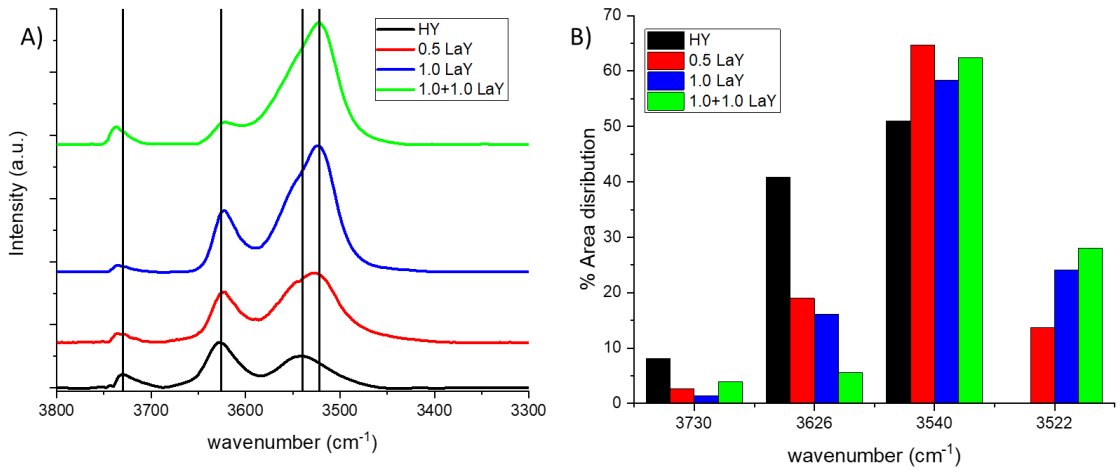

Figure 26. A) FTIR spectra of HY and LaY samples at varying La loadings in the hydroxyl region. B) Distribution of area under the peak for the four bands found from the FTIR spectra for the various zeolite samples. All spectra were recorded at 300 °C.

To understand the nature of Bronsted sites and the hydroxyl groups of La modified zeolites, **Figure 26** shows the FTIR spectra of HY and LaY samples in the hydroxyl region. At 300 °C, four hydroxyl IR bands are observed, centered around 3730 cm^{-1}, 3626 cm^{-1}, 3540 cm^{-1}, and 3522 cm^{-1}. 3730 cm^{-1} band is related to terminal silanols (Si-OH). The 3626 cm^{-1} and 3540 cm^{-1} bands have been ascribed to bridging hydroxyl groups (Si-OH-Al) in the supercage and sodalite cage, respectively. Finally, 3522 cm^{-1} band, only appears after the addition of La, is related to hydroxylated La species [67]. There are several conclusions that can be drawn from the FTIR results. First, the addition of La reduces the silanol peak intensity, a further indication that La

preserved the structural integrity of the zeolite. Interestingly, the band related to hydroxylated La species increases strongly with La loading. Lercher et al. have attributed this characteristic band to the La-OH species [29, 67, 102].

3.8.4 Effects of La on activity, selectivity, and activation energy during isooctane cracking

The previous chapter discussed how isooctane cracking serves as an effective method for measuring the rates and distribution of protolytic cracking, dehydrogenation, and hydrogen transfer reactions. As an industrial relevance example, La-incorporated Y zeolite was used as a catalyst and compared to the parent Y zeolite. The findings indicated that La suppresses the protolytic cracking pathway while enhancing the hydrogen transfer and dehydrogenation pathways. This work aims to further explore and understand these results by varying the amount of La incorporated to elucidate the role of La in altering the relative rates of these reaction pathways. To ensure that the rate of isooctane cracking is not influenced by the heat of adsorption of isooctane, **Figure 27** shows the heat of adsorption of isooctane over HY and 1.0LaY at varying isooctane coverage. At 100 ^{o}C, the heat of adsorption appears to be similar for both HY and 1.0LaY, which is around 88 kJ/mol. Furthermore, Denayer et al. reported that the heat of adsorption of isooctane over NaY (no Bronsted acid sites) is around 57 kJ/mol [122], suggesting that the heat of adsorption of isooctane over HY and LaY is also chemisorption, and not strictly physisorption. These results suggests that the changes in the apparent activation barrier of a reaction pathway during isooctane cracking is also a reflection in the changes in the intrinsic barrier.

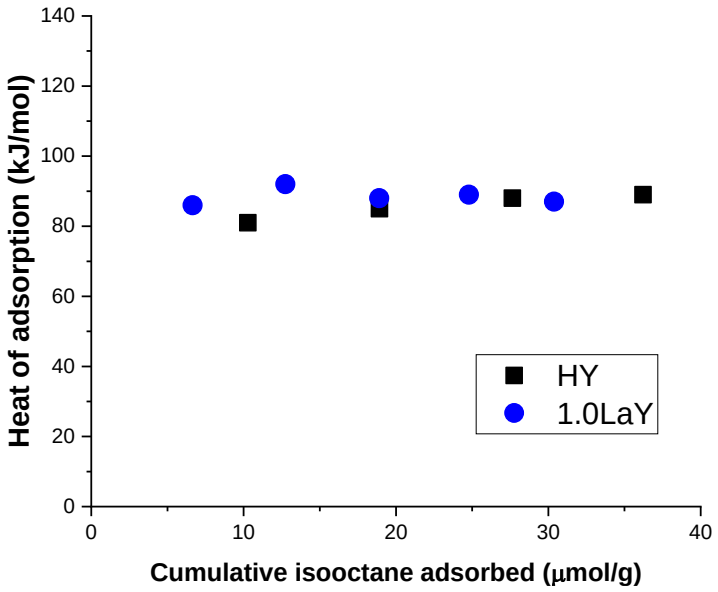

Figure 27. Isooctane heat of adsorption over HY and 1.0LaY at varying isooctane coverage. Adsorption conditions: 300 mg, 100 °C.

Figure 28 shows the TOF of isooctane cracking for all the catalyst samples at two different catalyst loadings: 10 mg and 25 mg. For both masses, it appears that the addition of La reduces the selectivity towards methane, while increasing the selectivity towards butane (**Figure 28A and B**). This suggests that the addition of La changes the reaction pathway of iscootane cracking. This trend continues until a maximum butane selectivity is achieved with the 1.0LaY sample. **Figure 28C** shows the difference in TOF between 10 mg and 25 mg runs for all samples. In the case of HY, the turnover frequency over the two catalyst masses remains relatively the same. Furthermore, the product selectivity remains relatively unchanged over the two masses for HY. Remarkably, when La is incorporated, the TOF over 25 mg increases significantly, especially for 0.1LaY and 0.5LaY. This change is also accompanied by the drastic changes in product selectivity, where methane selectivity is significantly suppressed while butane selectivity is significantly enhanced when the catalyst mass increases from 10mg to 25mg. In the previous chapter, we have shown that

methane and butane are related to protolytic cracking and hydrogen transfer product, respectively. The change in both TOF and product selectivity when increasing lanthanum loadings and catalyst mass is an indicator that the main reaction mechanism in isooctane cracking is shifting from protolytic cracking to hydrogen transfer.

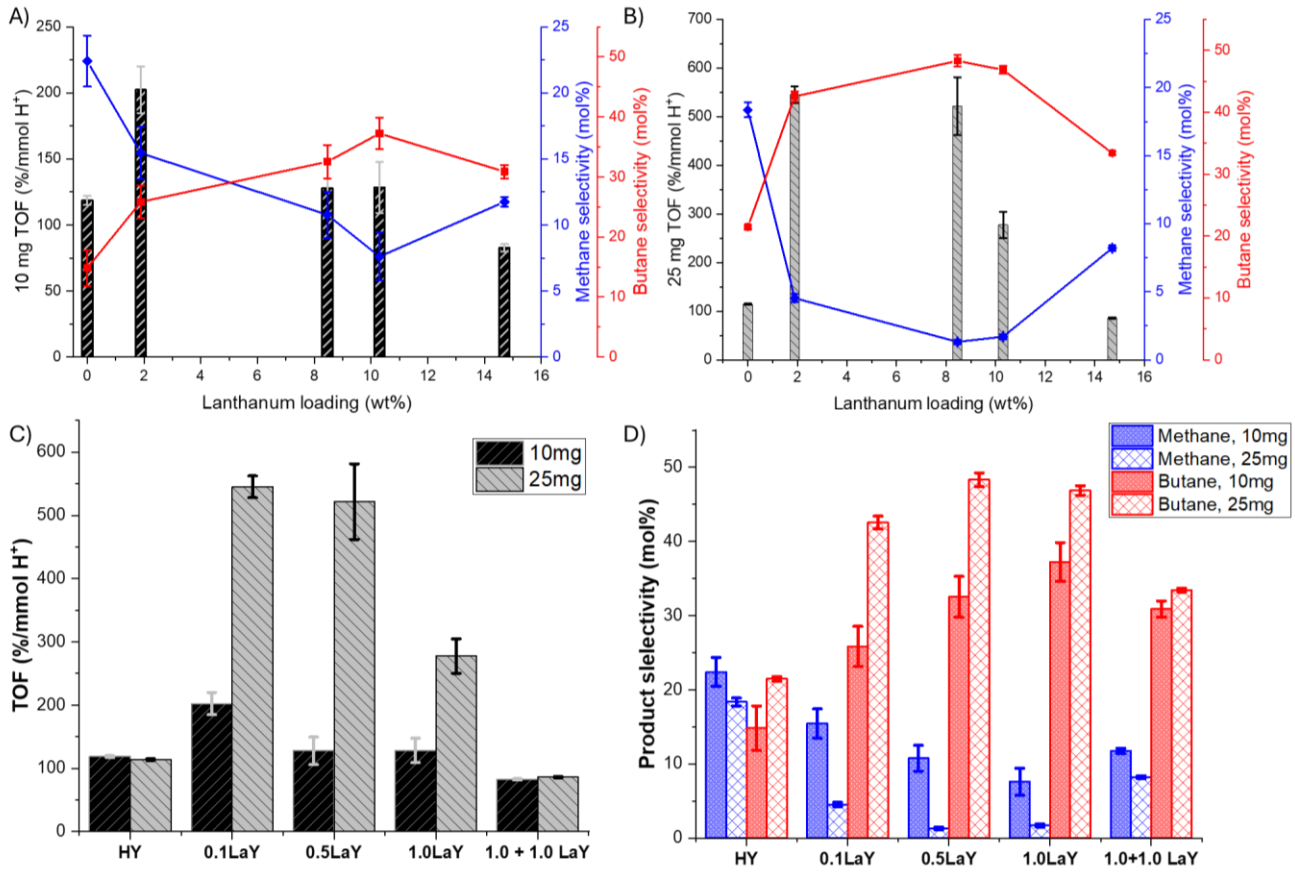

Figure 28. A) Isooctane cracking TOF, methane selectivity, and butane selectivity over 10mg of various La loading. B) Isooctane cracking TOF, methane selectivity, and butane selectivity over 25mg of various La loading. C) Isooctane cracking TOF comparing 10mg and 25mg loading of the various samples. D) Methane and butane product selectivity over 10mg and 25mg loading of the various samples.

In the previous chapter, it was also found that by varying mass, the TOF of isooctane cracking over LaY increases significantly as well (**Figure 14**). This phenomenon appears

consistent for La-incorporated Y zeolites. To explain the changes in TOF as mass increases for LaY, a series of reaction equations involving protolytic cracking and hydrogen transfer pathway during isooctane cracking over Bronsted acid site was developed. **Table 9** illustrates the reaction schemes of isooctane cracking, alongside the simplified rate expression for isooctane and butene adsorption/desorption equilibrium, protolytic cracking, and hydrogen transfer pathway. These reaction mechanisms of isooctane cracking are the simplified version of those in the previous chapter (**Scheme 2.1** and **Scheme 2.2**). There are several assumptions that were made in developing the rate expressions:

1) Gas phase isooctane is in equilibrium with isooctane available for protolytic cracking (iC8 + site). The equilibrium constant is the same for any catalyst and catalyst mass.

2) All butene isomers from the cracking product is in equilibrium with isobutyl alkoxide and the equilibrium constant is independent of catalyst mass.

3) Only isooctane and butyl alkoxide compete for sites

4) Minimal catalyst deactivation, $k_d = 0$.

5) Hydrogen transfer is an Eley-Rideal mechanism (gas phase isooctane reacts with surface alkoxide) [123].

Table 9. Series of reactions in the cracking of isooctane over Bronsted acid sites via protolytic cracking and hydrogen transfer.

Reaction	Scheme	Rate expression
Isooctane gas-phase to zeolite pore/sites equilibrium	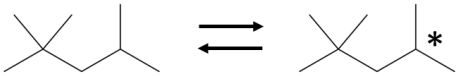	$K_{iC_8} = \frac{C_{iC_8}}{P_{iC_8}}$
Butene gas-phase to isobutoxide equilibrium	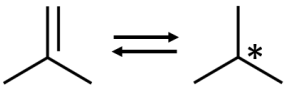	$K_{iC_{4=}} = \frac{C_{C_{4*}}}{P_{C_{4=}}}$
Protolytic cracking	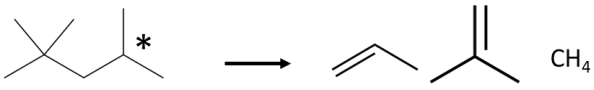	$r_{PC} = \frac{k_{PC} K_{iC_8} P_{iC_8}}{1 + K_{iC_8} P_{iC_8}}$
Hydrogen Transfer	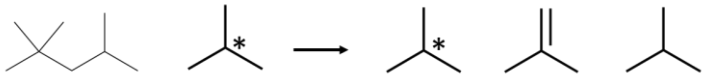	$r_{HT} = \frac{k_{HT} P_{iC_8} K_{C_{4=}} P_{C_{4=}}}{1 + K_{iC_8} P_{iC_8} + K_{C_{4=}} P_{C_{4=}}}$

With the series of reactions and rate expressions now established, the isooctane conversion and TOF can be simulated by varying the relative ratio of protolytic cracking and hydrogen transfer rate constants. **Figure 29A and B** show the isooctane conversion and isooctane TOF as a function of mass by varying k_{HT}, while keeping k_{PC} constant. Figure C) and D) show the isooctane conversion and isooctane TOF as a function of mass by varying k_{PC}, while keeping k_{HT} constant. Based on the model, the increase of TOF at higher mass is possible when the intrinsic rate of hydrogen transfer increases. This is due to the bimolecular nature of hydrogen transfer reaction, which allows the rate to increase with catalyst mass due to subsequent reactions of the butene produced from the early stage of the catalyst bed. On the other hand, a change in protolytic

cracking rate constant does not cause the TOF to change over the catalyst bed. This is due to the monomolecular nature of protolytic cracking, where the reaction rate is strictly due to isooctane partial pressure and does not require products concentration to initiate the reaction.

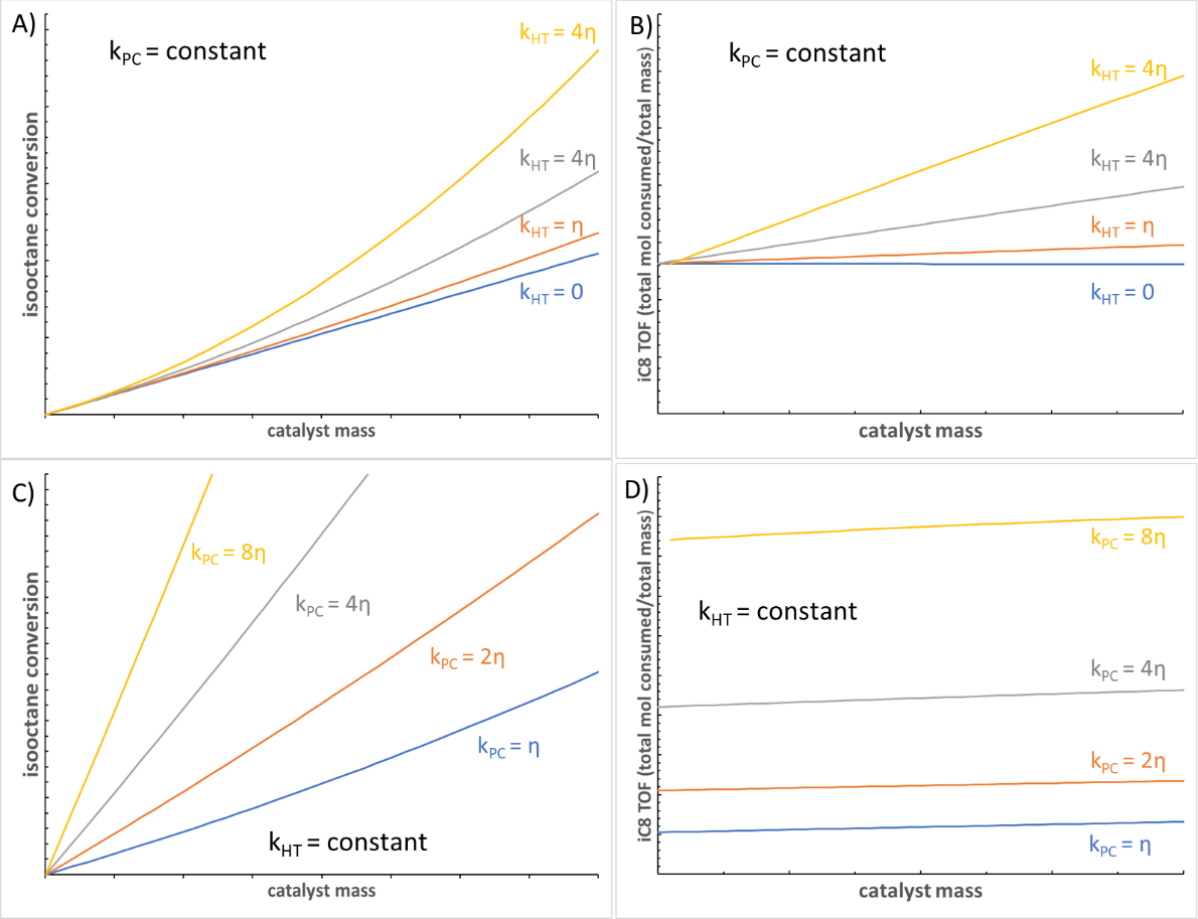

Figure 29. Simulated isooctane conversion and isooctane TOF as a function of catalyst mass using series of reaction equations from **Table 9**. A) Isooctane conversion versus catalyst mass by changing k_{HT}. B) Isooctane TOF versus catalyst mass by changing k_{HT}. C) Isooctane conversion versus catalyst mass by changing k_{PC}. D) Isooctane TOF versus catalyst mass by changing k_{PC}.

By running isooctane cracking reaction over HY and 1.0LaY at varying catalyst masses, the isooctane cracking reaction constants can be found. **Figure 30** and **Table 10** show that the

addition of La into Y zeolite enhances the hydrogen transfer rate constant, while simultaneously suppress protolytic cracking rate constant.

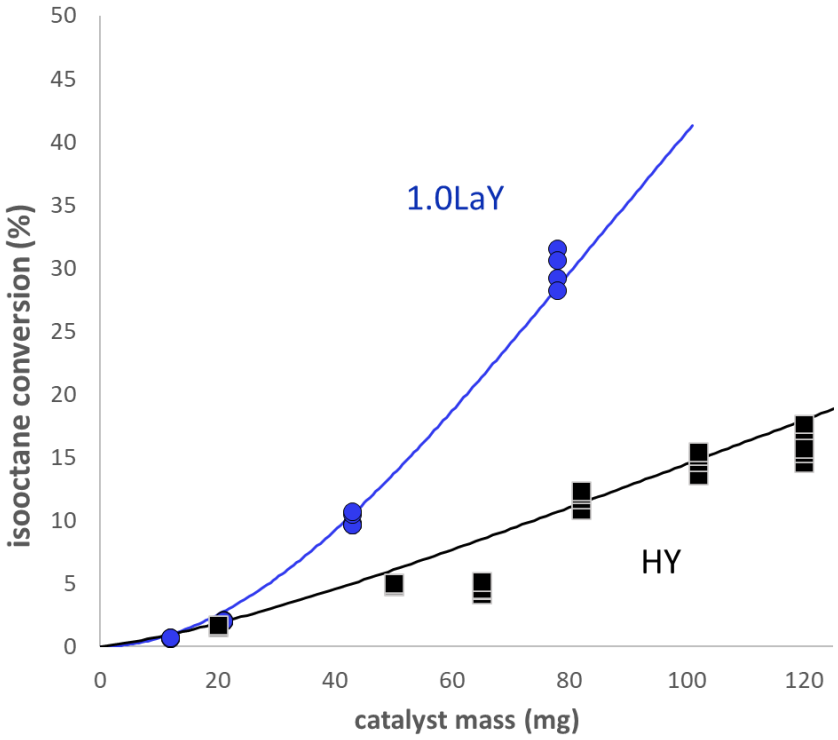

Figure 30. Isooctane conversion as a function of catalyst mass for HY and 1.0LaY. Solid lines represent the model using the reaction constants. Reaction conditions: continuous flow reactor at 2.4 kPa of isooctane partial pressure, 80 mL/min of carrier gas flow, 400ºC, 1 atm.

Table 10. Rate constants for HY and 1.0LaY during isooctane cracking. . Reaction conditions: continuous flow reactor at 2.4 kPa of isooctane partial pressure, 80 mL/min of carrier gas flow, 400ºC, 1 atm.

Constants	**HY**	**1.0LaY**
k_{PC} (hr^{-1})	2.68×10^{-2}	4.12×10^{-3}
k_{HT} (L/mmol.hr)	3.45×10^{-3}	6.96×10^{-2}
K_{iC8} (mmol/L)	0.0217	
$K_{iC4=}$ (mmol/L)	5.18	

Under similar isooctane conversion, the reaction pathways distribution can be plotted in a ternary plot to investigate how the addition of La changes the pathway selectivity. **Figure 31** shows the ternary plot of the various zeolite samples at isoconversion of isooctane. As the amount of La incorporated increases, the selectivity towards hydrogen transfer also increases while decreasing protolytic cracking selectivity. These results further show that La increases the intrinsic hydrogen transfer rate during isooctane cracking. The enhancement continues with increasing loading, until it reaches a maximum, as further addition of La via double exchange (1.0+1.0LaY) does not increase the hydrogen transfer selectivity but rather enhances dehydrogenation. To further illustrate the role of La in altering protolytic cracking and hydrogen transfer pathways, **Figure 32** shows that activation energy for protolytic cracking pathway and hydrogen transfer pathways for HY and LaY samples. As previously mentioned, considering the heat of adsorption of isooctane is similar for both HY and LaY1.0, the change in the apparent rate barrier is also an indication in the change of the intrinsic barrier. For protolytic cracking, the introduction of La into Y zeolite significantly increases the activation energy, even after a very low loading. Interestingly, further increases in La loading appear to not significantly change the protolytic cracking activation energy, within the range of uncertainty. On the other hand, the activation energy for hydrogen transfer pathway decreases with the addition of La. The addition of La progressively reduces the activation

barrier until a high loading of La, as seen in the 1.0+1.0LaY sample, which resulted in a slight increase in the barrier.

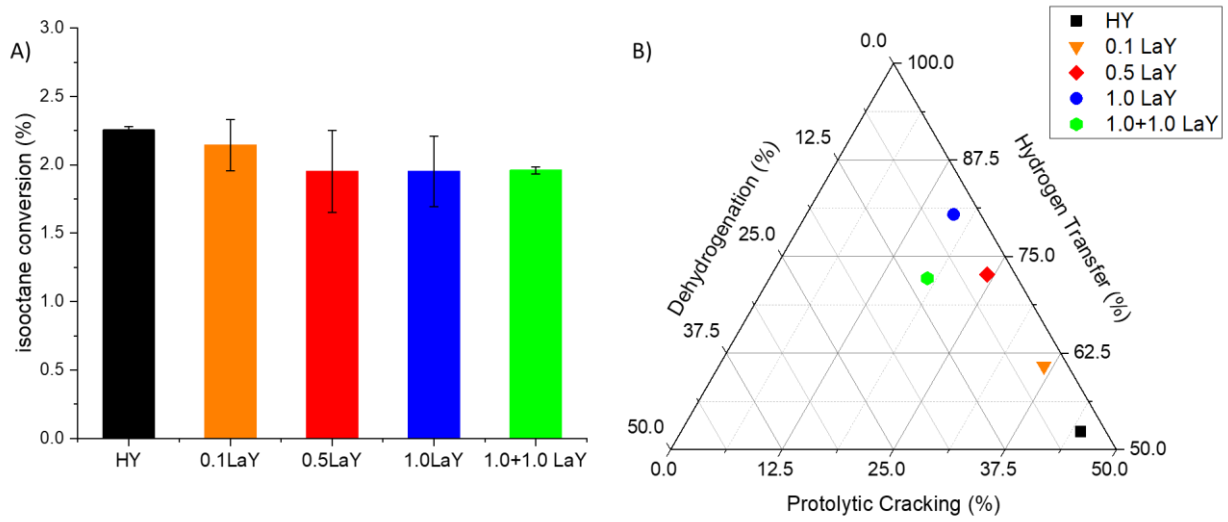

Figure 31. A) Isooctane cracking over various zeolite samples at isooconversion B) Reaction pathway distribution. Reaction conditions: Reaction conditions: 400 C, 10-25mg cat, 1.7 kPa, continuous flow mode. Error bars reflect the deviation in activity over 220 min t.o.s.

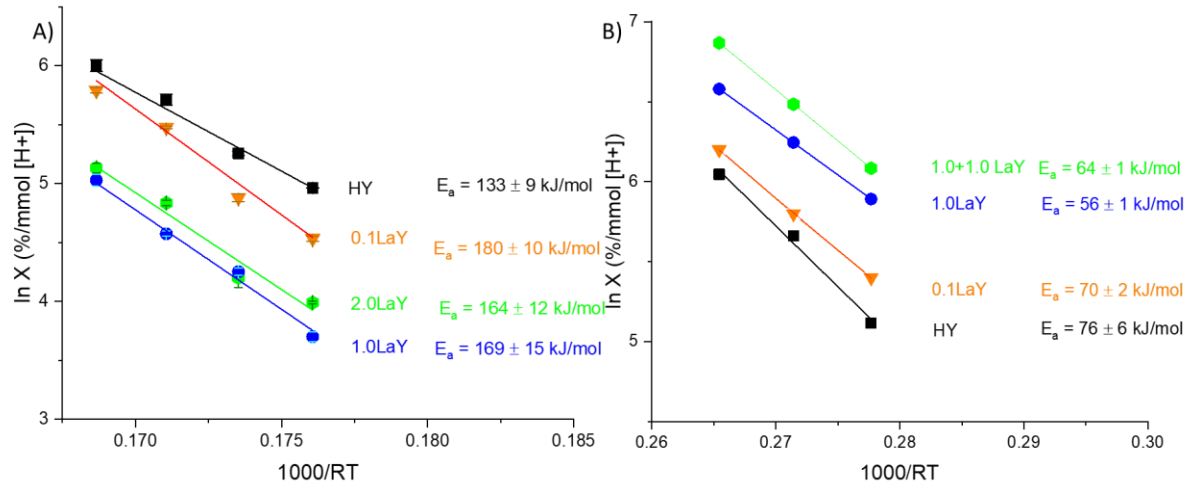

Figure 32. Apparent activation energy for A) protolytic cracking pathway and B) hydrogen transfer pathway for HY and LaY samples. PC reaction conditions: Pulse mode. 5 mg catalyst. 0.56 kPa. 100 mL/min N2 carrier flow. 400-

430 ºC.HT reaction conditions: Continuous flow mode. 5-12 mg catalyst. 1.11 kPa. 100 mL/min N2 carrier flow.

160-180 ºC.

3.10 Discussions

From the BET and XRD results of the calcined lanthanum samples, lanthanum clusters such as La_2O_3 and $La(NO_3)_3$ are not present within the calcined lanthanum samples. This suggests that the La species are solely the La cationic species, including $La(OH)_2^+$, $La(OH)^{2+}$, La^{3+} and hydrated La^{3+}, and these species are introduced in the zeolite framework during the ion exchange process. In this process, the La^{3+} ions exist as the sterically bulky $[La(H_2O)_n]^{3+}$ species and are only allowed to exchange within the supercage [29, 31, 114]. During the calcination process, the La species becomes more dehydrated, resulting in a smaller cation and allowed to migrate to the sodalite cage and leave the supercage. Once in the sodalite cage, the La^{3+} stabilizes the zeolitic framework and makes it less susceptible to dealumination [29, 30, 111, 114, 124]. As a result, the La incorporated Y maintained the structural integrity of the original Y zeolite during higher temperature conditions [27, 28]. It is noteworthy that none of the samples in this study was exposed to extreme hydrothermal conditions, which has been attributed to the main cause of structural collapse during FCC processes. Our recent findings indicate that the proton form of low Si/Al Y zeolite is prone to framework collapse when exposed to moisture, even under gentle temperature ramp and vacuum conditions to reach the desired reaction temperature. [112]. Hence, the presence of La inside the zeolite structure potentially increases the activation barrier for the water attack during dehydration process, as well as lowering the amount of water being adsorbed at ambient conditions.

There are various effects of La on the acidic properties of the parent zeolite. First, the addition of La increases the Bronsted acid density of the zeolites. This can further indicate that La role in preserving the structural integrity of the original zeolite, ensuring the retention of the Bronsted acids [100]. Furthermore, La introduces new Bronsted acid sites in the form of La-OH groups [29, 67], indicated by the emergence of La associated characteristic band at 3522 cm^{-1} in

FTIR, as well as high temperature peak around 390 °C from IPA-TPD. These newly created sites have the potential to actively participate in IPA decomposition and isooctane cracking, thus altering the overall Bronsted acid density of the zeolite. The role of higher Bronsted density in the isooctane cracking activity and selectivity will be discussed later. Results from NH_3-TPD and IPA-TPD suggest that the addition of La also increases the Bronsted acid strength.

During isooctane cracking, the addition of La appears to shift the reaction selectivity towards hydrogen transfer, while simultaneously suppresses protolytic cracking. Interestingly, a small addition of La strongly suppresses the PC pathway, suggesting that La has a preferential titration on the synergistic sites that have been shown to reduce the activation energy in protolytic cracking pathway. In zeolites, surface features, including site proximity, EFAl, and partially coordinated species, can modify the local environment of the Bronsted acid site [23, 24, 92, 93]. These sites have been shown to lower the activation barrier of protolytic cracking. There are two possible explanations on how La removes these synergistic sites. First, the synergistic sites associated with EFAl species was reduced with the presence of La. Liu et al. investigated the Bronsted acidity and catalytic reactivity of faujasite zeolite via periodic DFT, and they found the presence of multinuclear EFAl within the sodalite cage promotes protolytic cracking rate during propane cracking [95]. Thus, with the addition of La, the amount of EFAl within the sodalite cage is reduced by La displacing these species from the sodalite or/and lowering the amount of EFAl clusters formed by La lowering the dealumination rate of the zeolite. The second possibility is La titrate the Bronsted acids that are in pairs. Via ^1H double-quantum NMR spectroscopy experiments, Schroeder et al. identified two pairs of Bronsted acid sites in Y zeolite, located in the supercage and in the sodalite cage. Since La can exist as $La(OH)^{2+}$, these paired sites can be titrated by La, reducing the synergistic sites concentration.

The addition of La also improves the hydrogen transfer activity during isooctane cracking, shown by the enhancement of isooctane TOF at higher catalyst loading, ternary plot at isoconversion, and the reduction in hydrogen transfer activation energy. It is widely accepted that a higher Bronsted acid density improves the intrinsic hydrogen transfer activity [35, 58, 100, 125-128]. **Figure 33** shows the relationship between the relative TOF of isooctane cracking between 25 mg and 10 mg as a function of Bronsted acid density for all samples. This suggests that the Bronsted acid density plays a crucial role in enhancing the hydrogen transfer activity of the zeolite, regardless of the La content.

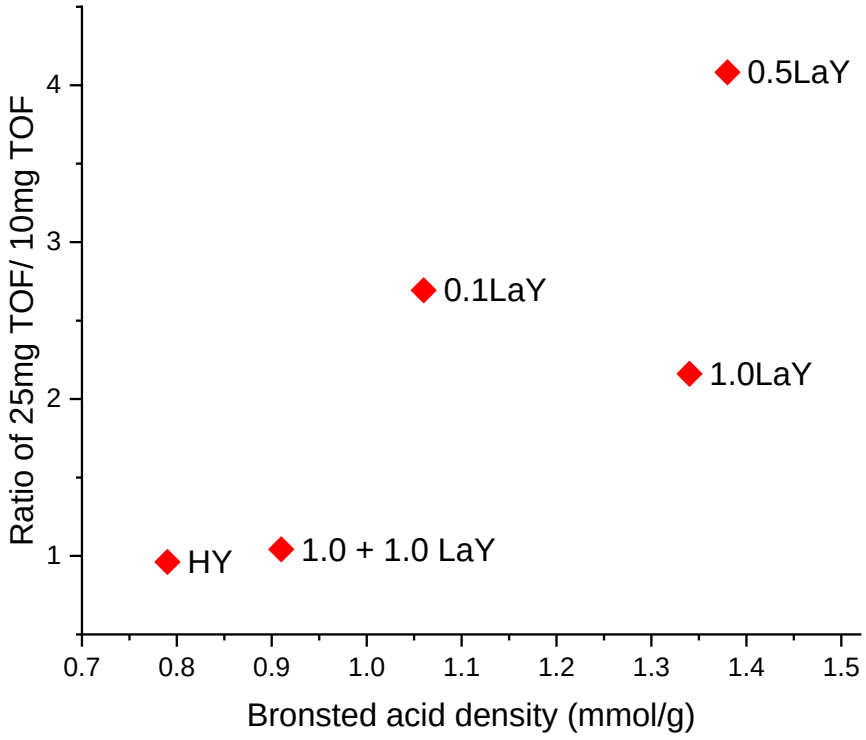

Figure 33. Ratio of TOF of isooctane cracking over 25mg and 10mg catalyst loading as a function of Bronsted acid density.

However, the exact role of La that contributes to the enhancement in hydrogen transfer activity remains controversial. This is related to the nature of the Bronsted acid sites with the presence of La. As previously mentioned, the first explanation in the higher Bronsted acid density is due to La

ability in retaining the original Bronsted sites. Dumesic et al. suggested that a higher Bronsted density within Y zeolite increases the stabilization of the carbenium ion transition state during the hydrogen transfer step via polarization of the transition state species by the neighboring framework Bronsted site. Thus, by retaining the Bronsted acids from dealumination, La modified Y zeolites [100]. Another possibility is due to the presence of La-OH within the supercage with the introduction of La. Lercher's group indicated that the La-OH species within the zeolites promotes strong polarization of the C-H bond of bi- and tri-branched alkanes, resulted in a lower activation energy of hydrogen transfer step [29, 67, 102, 103]. This work showed that both explanations are possible. At low La loading, the addition of La drastically improves the structural integrity of the zeolite, shown by BET, IPA-TPD, lowering silanol signal from FTIR, and significant increase in protolytic cracking activation energy. As a result, the retainment of the zeolite Bronsted density improves the hydrogen transfer selectivity during the isooctane cracking. However, it is worth noting that the activation energy towards hydrogen transfer pathway lowered only slightly. Additionally, further addition of La does not further improve the structural integrity of the zeolites from BET and FTIR. Furthermore, from FTIR, the further increase in the La-OH associated band shows the increase in La-OH species in the zeolite. Hence, the La-OH species within the zeolite is also crucial in increasing the intrinsic hydrogen transfer activity during isooctane cracking, shown by the ternary plot at isoconversion and further reduction in hydrogen transfer activation energy.

It is noteworthy that at high La loading (1.0 + 1.0LaY), the isooctane cracking selectivity favors dehydrogenation pathway, rather than further enhancement towards hydrogen transfer. This observation is further reflected by the slight increase in hydrogen transfer activation energy for this sample. These results can be explained in the reduction of the Bronsted density of the zeolite with higher La concentration, leading to favoring monomolecular pathway of dehydrogenation

reaction as opposed to the bimolecular, hydrogen transfers reaction. Interestingly, even under conditions that enhance monomolecular pathway, the presence of La favors dehydrogenation as opposed to protolytic cracking. The possible explanation due to the polarization of the C-H bond of the ternary carbon of the isooctane by the La-OH species, resulting a more stable transition state [29].

3.11 Conclusion

In this chapter, a series of La incorporated Y zeolite at various La loadings were prepared via ion exchange, using NH_4-Y zeolite as the starting material. From XRD and BET, the La species is well dispersed within the zeolite, and only exists as cationic species. From FTIR and BET, the incorporation of lanthanum into the Y zeolite maintains the structural integrity of the original zeolite, even under higher temperature conditions. This is crucial, as the proton form of low Si/Al Y zeolite is known to be susceptible to sodalite cage opening due to water attack, even at room temperature. The presence of lanthanum inside the zeolite structure potentially increases the activation barrier for water attack at high temperature as well as ambient conditions, providing additional stability. The addition of lanthanum also affects the acidic properties of the zeolite, increasing the Bronsted acid density by retaining the original Bronsted and introducing new Bronsted acid sites in the form of La-OH groups. La also increases the Bronsted acid strength. During isooctane cracking, lanthanum shifts the reaction selectivity towards hydrogen transfer while suppressing protolytic cracking. This effect is attributed to lanthanum's titration of synergistic sites that reduce the activation energy in the protolytic cracking pathway. The improvement in hydrogen transfer pathway has been attributed to the higher Bronsted acid density in the La modified zeolites. At high La loading, the monomolecular pathway is favored towards dehydrogenation as opposed to protolytic cracking, indicating La ability in performing alkane dehydrogenation reaction.

Chapter 4

Incorporation of Lanthanum in H-MOR Zeolite to Improve Shape Selectivity and Stability Against Coke Formation during Toluene Alkylation with Isopropanol

Acidic zeolites are attractive alkylation catalysts due to their high activity, stability, and tunable shape-selectivity. An optimal alkylation catalyst should have two main characteristics: shape selectivity towards desirable products and stability against coke; these characteristics can be achieved in zeolites by introducing suitable chemical additives. The use of lanthanum (La) as an additive has been extensively implemented in the petrochemical and oil refining industry. Despite the wide usage of La as an additive in zeolites, its exact role is still a matter of extensive investigation. This work investigates the effects of La incorporation in H-MOR and focuses on the shape selectivity and catalysts' stability against coking in alkylating toluene and isopropanol. Lanthanum-doped mordenite (La-MOR) catalysts were synthesized via incipient wetness impregnation with varying $La(NO_3)_3$ concentrations, then calcined. The alkylation reaction was carried out in a liquid-phase batch reactor and a gas-phase continuous flow reactor at varying catalyst mass and reactants' concentrations. The catalysts were characterized by IPA-TPD, BET, XRD, TGMS, and ^{13}C-NMR. During the alkylation of toluene with isopropanol, the presence of La inside the MOR zeolite was found to enhance para-selectivity while suppressing ortho-selectivity. It is proposed that La restricts the zeolite pores, favoring the diffusion of the para-isomer compared to the ortho and meta-alkylated products, which are kinetically bulkier. In addition, La incorporation was found to improve the catalyst resistance to coke formation by decreasing the rate of propylene oligomerization. La-MOR not only produces less coke than H-MOR, but also the coke that is formed in the La-containing catalyst appears to burn off more easily than that on H-MOR, as reflected by a lower combustion temperature. Moreover, TGMS and ^{13}C-NMR reveal that the coke deposits in La-MOR have a higher H/C than that on H-MOR, explaining its higher reactivity towards combustion. The increase in catalyst stability by the presence of La can be attributed to its ability to promote H transfer from coke to the surface carbenium ion, as well as the titration of Bronsted acid sites, which suppresses the oligomerization rate.

This work is a completed manuscript waiting for submission

4.5 Introduction

The alkylation of aromatic compounds by an alkylating agent is a widely employed process within the petrochemical and oil refining sectors. Benzene, toluene, and xylene (BTX) are typical aromatic feedstocks, while olefins and short alcohols represent common types of alkylating agents. Alkylated intermediates, such as ethylbenzene (EB), cumene, para-diethylbenzene (para-DEB), para-and meta-diisopropylbenzene (para-and meta-DIPB), linear alkylbenzenes (LAB), para-ethyltoluene, and para-and meta-cymene, are then used to produce other valuable products such as polymers, paints, detergents, medicines, agricultural products, and explosives [43, 44]. Recently, the production of biomass-based fuels has become increasingly important as an alternative energy resource. Complex compounds such as lignin, cellulose, and hemicellulose are often broken down via pyrolysis to form aromatics and light oxygenates. These can then be used as feedstocks to produce valuable chemicals and fuels [129]. In that case, the alkylation reaction plays a vital role in converting these broken-down compounds into a bigger compound via C-C coupling and produce specific chemicals or improve fuel properties [130].

Alkylation is catalyzed by Bronsted or Lewis acid catalysts. Typical catalysts include $AlCl_3$, HF, and H_2SO_4, which can be highly corrosive, toxic, and difficult to separate from the products [131]. In contrast, solid acid catalysts are easier to handle, less prone to equipment corrosion, simpler regarding environmental disposal and toxicity, with easier separation and recycling [132]. Among the most attractive alkylation solid catalysts are acidic zeolites, known for their appealing characteristics such as tunability, high acid density, high surface area, high alkylation activity, high stability, high shape selectivity, and low toxicity [12, 133, 134]. Two main criteria should be considered when selecting an alkylation reaction catalyst: high shape selectivity toward the desired product and high catalyst stability against coking.

It is important to note that the application of the alkylated products depends on the specific isomer of the product. For instance, among the xylene products, the para-isomer has the highest demand compared to ortho-, and meta since the oxidation of the para- xylene produces terephthalic acid (TPA), a key chemical in the production of polyethylene terephthalate (PET). Similarly, in the production of cymene (isopropyl toluene), the para isomer is desirable for its utilization in the pharmaceutical industry, while ortho isomer has a lower demand due to its difficult oxidation [43, 135]. Therefore, during the alkylation process, it is important that the selectivity of the desired product is maximized. The presence of constricted pores and channels in zeolites plays a crucial role in modifying the selectivity of the alkylated products, and these pores can be modified to further improve the shape selectivity of the products. As for catalyst stability against coking, a higher tolerance to coke allows production for longer period. Furthermore, lower amount of coke produced also resulted in lower CO_2 production during catalyst regeneration.

Various studies have been conducted in the past decades to improve these characteristics, and one of the methods is introducing chemical additives into the zeolites. The roles of these additives include the tuning of acid density, acid strength, zeolite pore size, as well as stability. The addition of rare-earth metals, such as La, has shown promise in fluid catalytic cracking (FCC) processes due to its role in improving thermal stability and hydride transfer[28, 29, 32, 136].

Despite the extensive utilization of lanthanum (La) in petrochemical industries, the precise role, positioning within zeolites, and the mechanism through which it impacts chemical reactions remain subjects of thorough investigation. Moreover, the effects of lanthanum in zeolites on the alkylation of aromatics and oxygenates/olefins have not been fully explored, thus providing ample opportunity for further discourse. Therefore, in this work, we investigate the effects of La

incorporation in H-MOR zeolite, focusing on the shape selectivity and catalysts' stability improvements during the alkylation of toluene with isopropanol.

4.6 Experimental and Methodologies

4.6.2 Chemicals and Materials

Toluene (≥99.9%), isopropanol (99.9%), cyclohexane (≥99.9%), lanthanum nitrate hexahydrate (99.999% trace metals basis), ethanol (99.9%), and sodium nitrate, $NaNO_3$ (99.5%) were purchased from Sigma-Aldrich, and used without further purification. Ammonium mordenite zeolite, NH_4-MOR, with Si/Al=10 was obtained from Zeolyst (CBV 21A).

4.6.3 Catalyst Preparation

All catalysts were prepared using NH_4-MOR as the parent zeolite. The protonated form of the zeolite (H-MOR) was produced by calcining the parent zeolite in flowing air at 550 ºC, at a heating rate of 1 ºC/min, for 6 h. The lanthanum-mordenite, La-MOR, was produced by incipient wetness impregnation into the parent zeolite, using lanthanum nitrate solution in ethanol at varying concentrations. Each La-MOR xM was synthesized by impregnating xM of $La(NO_3)_3$ in ethanol. Once impregnated, the sample was dried in a vacuum oven at 80 ºC, overnight, followed by similar calcination steps as H-MOR. **Table 11** shows the weight% of La for all La-MORs used in this work. The sodium titrated MOR, Na-MOR was prepared by ion exchange one gram of NH_4-MOR with 20 mL of 0.07M of $NaNO_3$ solution at room temperature for 1 hour. The sample was then dried in a vacuum oven at 80 ºC, overnight, followed by similar calcination steps as H-MOR.

Table 11. Lanthanum weight% for all La-MOR samples

La-MOR concentrations (xM)	La wt %
0.04	0.11
0.1	0.28
0.5	1.37
1	2.70
1.25	3.36
2	5.26

4.6.4 Catalyst Characterization

4.6.4.1 BET Surface area and pore volume

N_2 physisorption was carried out at -198ºC on Micrometrics ASAP 2010. The sample was degassed at 300ºC for 3 hours under a vacuum. The surface area, pore volume, and micropore volume were determined using the Braunauer-Emmer-Teller (BET) method.

4.6.4.2 Temperature Program Desorption (TPD)

The total acid site density was quantified using temperature-programmed desorption of chemically adsorbed ammonia (NH_3-TPD). Approximately 50 mg of catalyst was inserted in a continuous gas-phase reactor, and He was used as a carrier gas at 30 mL/min flow. The outflowing gas was connected to a MKS Cirrus mass spectrometer to track m/z of 16. The catalyst was pretreated at 300 ºC for 1 h to remove moisture. After the pretreatment, the temperature was cooled to 100 ºC as a starting temperature. The catalyst was exposed to a constant 30 mL/min flow of 2 mol% of ammonia in He until a consistent m/z=16 signal was detected by the mass-spectroscopy. Then, the stream was switched back to the He carrier, and physisorbed NH_3 was removed by keeping the temperature at 100 ºC under He flow for 1 hour. The catalyst, then, was heated to 600

ºC at a 10 ºC/min heating ramp. The ammonia peak was used to determine the amount of total acid sites. The NH_3 signal was calibrated for each run using 500 μL of 2 mol% NH_3 in He pulses.

On the other hand, the density of Brønsted acid sites was quantified through the temperature-programmed desorption/reaction of isopropylamine (IPA-TPD). The catalyst mass, He carrier flow rate, and catalyst pretreatment mirrored those of NH_3-TPD. The outflowing gas was directed to the MKS Cirrus mass spectrometer to monitor m/z values of 17, 41, and 58, corresponding to ammonia, propylene, and IPA, respectively. Following pretreatment, the catalyst was subject to multiple injections of 2 μL IPA pulses until saturation; that is, when the IPA area observed via mass spectrometry was constant. Subsequently, the physically adsorbed IPA was purged by maintaining the temperature at 100 °C under a He flow for 1 h. The catalyst was then subjected to heating at a rate of 10 °C/min, reaching 600 °C. According to the Hoffman's elimination stoichiometry, the propylene peak can be utilized to ascertain the total count of Brønsted acid sites. Calibration of the propylene signal for each run was performed using 500 μL propylene pulses.

4.6.4.3 X-ray Diffraction (XRD)

Powder X-ray diffraction (XRD) was performed on a Rigaku Ultima IV diffractometer (Cu Kα radiation, λ =1.5406 Å) in the 2θ range of 5–70° under an operating voltage of 40 kV and a current of 44 mA. Each sample was pretreated in a vacuum oven at 80 °C to remove moisture.

4.6.4.4 Fourier Transform Infrared Spectroscopy (FTIR)

In-situ diffuse reflectance infrared Fourier transform spectroscopy (DRIFTS) was performed in a high-temperature cell (Harrick Scientific). The in-situ cell was mounted inside a Praying Mantis diffuse reflectance accessory (Harrick Scientific) paired with a Thermo Scientific Nicolet iS10 FTIR spectrometer equipped with a HgCdTe (MCT) detector. Potassium bromide, KBr, was

used to obtain the background scan for all samples. For a given catalyst analysis, approximately 100 mg of the catalyst was loaded into the cell and pretreated at 300 ºC for 1 hour to remove adsorbed water. Then, the spectra for each sample were collected at 300 ºC. All spectra were collected with a resolution of 4 cm^{-1} by merging 64-100 scans to minimize spectral noise. Measurements were made while purging the FTIR with dry He gas to remove desorbed water and to minimize atmospheric gas interference with the beam path. The purge line was connected to a column of dry Zeolite 4A as water adsorber.

4.6.4.5 Thermogravimetric Mass Spectroscopy (TG-MS)

Thermogravimetric mass spectroscopy (TG-MS) analysis of the spent catalysts was conducted to investigate the amount of coke, as well as the nature of coke deposited during the alkylation reaction. The analysis was conducted in NETZSCH STA Jupiter 449 F1 (TG), connected to QMS Aelos 403C mass spectrometer (MS). In a typical run, approximately 15 mg sample is loaded into an alumina crucible, which is then inserted into the TG, under a constant 40 mL/min airflow. Then, the sample is heated at a rate of 10 ºC/min until it reaches 800 ºC. The MS signals for m/z=18 and m/z=44 were tracked throughout the analysis to quantify the amount of water and CO_2 evolved during the heating process.

4.6.4.6 Solid state ^{13}C-MAS NMR

Solid-state ^{13}C-MAS NMR were performed, on the spent catalysts, at the Oklahoma State University using Bruker Neo 600 MHz Spectrometer with a 3.2 mm MAS probe.

4.6.5 Catalytic Test

4.6.5.1 Liquid phase batch reactor

The alkylation of toluene and isopropanol were conducted in a liquid-phase batch reactor. The reaction took place in a 250 mL stainless steel Parr reactor, utilizing cyclohexane as a solvent. Varying catalyst masses and reactant concentrations were employed. In each run, the catalyst was introduced into cyclohexane and dispersed using a horn sonicator (20% amplitude, 10 min). The reactor system was initially purged with 700 psig of N_2 to eliminate air and subsequently pressurized to 150 psig as the initial N_2 pressure. The reactor was then heated to the desired reaction temperature with a stirring speed of 500 rpm. Once stabilized, reactants were injected from an adjacent vessel using N2 gas. The total liquid volume for all reactions was maintained at 50 mL. The timer commenced upon injecting the reactants into the reactor. Upon completion of the desired reaction, the reactor temperature was rapidly lowered using an ice bath. The reaction solution was analyzed using an Agilent 6890 gas chromatograph equipped with a flame ionization detector (GC-FID), with Zebron ZB-5 column. Phenol was used as an external standard. Product peaks were identified using a Shimadzu QP2010S gas chromatograph-mass spectrometer (GC-MS).

To assess the relative deactivation rates among catalysts in the batch reactor, a deactivation analysis method proposed by Apesteguia et al. was employed [137, 138]. In this method, the alkylated product concentration is plotted against the catalyst mass multiplied by time (mass-cat x time) using two different amounts of catalysts. For an equivalent mass x time, a higher amount of catalyst will react in a shorter period, while a smaller amount of catalyst will react for a longer duration. For example, to achieve 2wt of mass x time, 2w amount of catalyst reacts for t amount of time, whereas w amount of catalyst will react for 2t amount of time. If the catalyst remains

active throughout the entire reaction, the plots for both catalyst amounts should overlap. However, if the catalyst deactivates, the smaller amount of catalyst will produce less alkylated product since it requires a longer time and, consequently, experiences more deactivation. Therefore, the curve with a smaller amount of catalyst will be separated from the curve with a higher amount of catalyst. The degree of separation between the two curves indicates the severity of catalyst deactivation. **Figure 34** provides a visual representation of this method at varying degrees of deactivation.

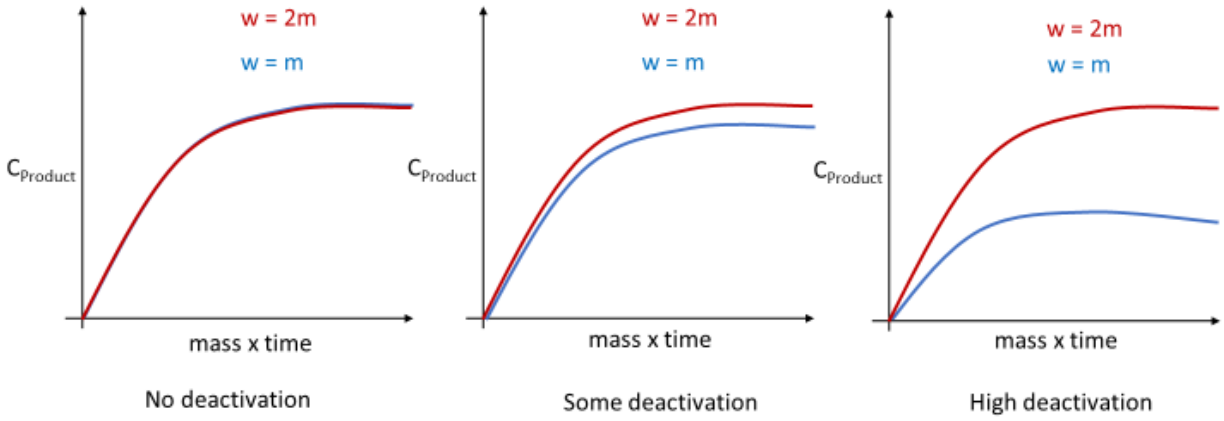

Figure 34. Visual representation of mass x time method in comparing deactivation between catalysts in a batch reactor.

To quantitatively determine the catalyst deactivation, the catalyst deactivation model used for the batch reaction is the exponential model, $\alpha = e^{-\beta_o t}$, where α is the activity coefficient, β_o is the deactivation coefficient, and t is time. The higher the β_o , the higher the catalyst deactivation [139].

4.6.5.2 Gas-phase continuous-flow reactor

4.6.5.2.1 Alkylation reaction

The alkylation of toluene and isopropanol was carried out in a gas-phase continuous flow reactor using He as a carrier gas. The pelletized catalyst (0.25 mm- 0.40 mm) was loaded and pretreated at 300 ºC for 1 hour to remove adsorbed water under 100 mL/min of N_2 flow. The reactor was then cooled down to the reaction temperature and was kept stabilizing for at least 1 hour. The reactants were fed at varying flowrate using a syringe pump (KD Scientific) and were vaporized at 130 ºC before entering the reactor. The molar ratio of toluene and isopropanol was varied by changing the molar ratio of the reactant in the injection syringe. All reactions were carried at atmospheric pressure. The outlet gas was analyzed using Hewlett Packard 6890 Series II GC-FID, using HP-Innowax column. The following deactivation function was used to quantify catalyst deactivation: $a = \frac{1}{1+\beta_o t}$, where α is the activity coefficient, βo is the deactivation coefficient, and t is time. The higher the βo, the higher the catalyst deactivation [140, 141]. Toluene conversion, X was equated as $X = \alpha X_o$, where X_o is the toluene conversion at time = 0. X_o was obtained from the deactivation function since it took some time for the flow reactor to reach a steady state.

4.6.5.2.2 Isooctane cracking reaction

The catalyst ability in performing protolytic cracking, hydrogen transfer, and dehydrogenation was probed using isooctane cracking, which has been demonstrated in **Chapter 2**. In a typical run, isooctane cracking was carried out in a gas-phase continuous flow reactor using N_2 as a carrier gas. The pelletized catalyst (0.25 mm- 0.40 mm) was loaded and pretreated at 300 ºC for 1 hour to

remove adsorbed water under 100 mL/min of N_2 flow. The reactor was then heated to the 400 ºC and was kept stabilizing for at least 1 hour. The isooctane partial pressure was kept at 2.7 kPa.

4.7 Results

4.7.2 Fresh Catalysts Characterizations

4.7.2.1 Physical Properties

Table 12 summarizes the influence of La on the parent MOR physical properties. It was found that the addition of La reduces surface area, pore-volume, and micropore volume of the zeolite structure. These results can be due to the lanthanum clusters constricting the zeolite pore or/and plugging the pore entrance, which have been previously reported [142-144]. **Figure 35A** shows the XRD spectra of H-MOR and La-MOR samples. For all La loadings, the addition of La does not modify the zeolitic structure. However, as La loading increases, the area under the diffraction peaks decreases. Similar results have been reported when La was impregnated into H-USY zeolite; the loss in area was attributed to absorption and/or different interference of the X-ray beam by the La species [145, 146]. Another possibility is that the addition of lanthanum causes the loss in crystallinity by partially dealuminating the zeolite framework. It is noteworthy that loss of crystallinity that are reported in most works introduced La via ion exchange, attributing the dealumination due to excess water exposure at elevated temperature [32]. In this work, however, we introduced La via incipient wetness impregnation, eliminating the possibility of the loss in crystallinity due to the ion exchange step [147]. Interestingly, as the La loading increases, a new characteristic peak appears at $2\theta = 20^{\circ}$, and the intensity of the peak increases with higher lanthanum loading (**Figure 35B**). This characteristic peak also appears in calcined lanthanum nitrate, indicating the presence of lanthanum nitrate/hydrate clusters inside the lanthanum incorporated zeolites.

Table 12. BET surface area and pore volume of fresh samples.

	Lanthanum weight%	BET surface area (m^2/g)	Pore volume (cm^3/g)	Micropore volume (cm^3/g)	Mesopore volume (cm^3/g)	XRD relative area under the curve (%)
H-MOR	0	409	0.249	0.186	0.063	100
La-MOR 0.04M	0.11	-	-	-	-	99.7
La-MOR 1.0M	2.70	393	0.235	0.181	0.054	85.5
La-MOR 2.0M	5.26	258	0.188	0.116	0.072	76.3

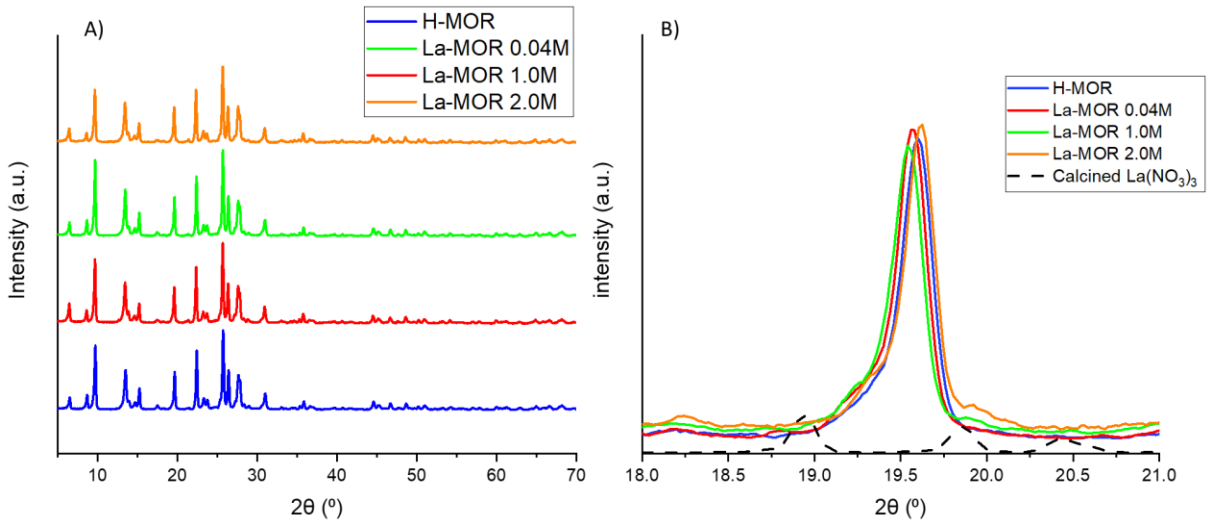

Figure 35. A) XRD spectra of H-MOR and La-MOR samples, B) XRD spectra of H-MOR and La-MOR samples at 2θ=18º-22º

4.7.2.2 Acidic Properties

Table 13 shows the total acid (Bronsted + Lewis) density. As the amount of La added increases, both Bronsted acid density and Lewis acid site density decreases. This observation was also found in other studies where the incorporation of La into zeolite β, Y, and ZSM-5 via ion exchange reduced the Bronsted acid site density [29, 32, 148-150]. Note that some studies have

reported an increase in Bronsted acid site density, particularly with zeolite Y via ion exchange due to hydration of La species [67, 151]. In this work, however, we introduced La via wetness impregnation. This potentially causes a larger La cluster, resulting in a larger ratio of the decrease in BAS masked by the clusters to the increase in BAS formed from the hydration of the lanthanum clusters. From the IPA-TPD profiles (**Figure 36**), the presence of La does not significantly alter the acid strength.

Table 13. Total acid density, Bronsted acid density, and Lewis acid density of fresh samples.

	Lanthanum weight%	**Total acid density[a] (mmol/gcat)**	**Bronsted acid density[b] (mmol/gcat)**	**Lewis acid density[c] (mmol/gcat)**
H-MOR	0	3.17	0.91	2.26
La-MOR 0.04M	0.11	2.79	-	-
La-MOR 1.0M	2.70	2.91	0.81	2.10
La-MOR 2.0M	5.26	2.13	0.69	1.44

a) NH_3-TPD
b) IPA-TPD
c) Difference between total acid density and Bronsted acid density

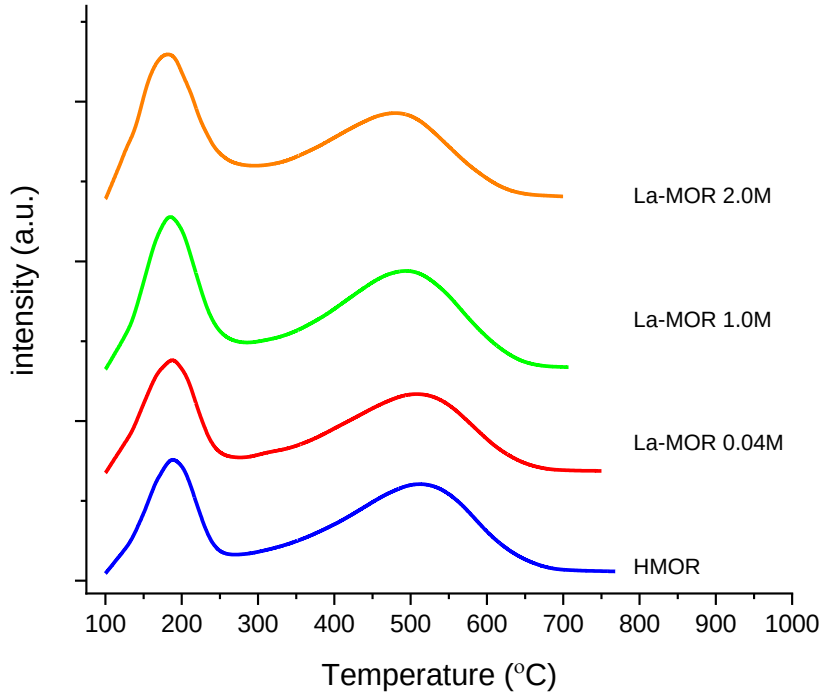

Figure 36. NH3-TPD curves of H-MOR, La-MOR 0.04M, La-MOR 1.0M, and La-MOR 2.0M

The catalysts were further characterized by FTIR; the spectra in the hydroxyl region 3300-3800 cm^{-1} are shown in **Figure 37A**. As previously reported [152-154], the small peak around 3750 cm^{-1} corresponds to terminal silanol groups. On the other hand, the large peak around 3600 cm^{-1} is associated with the acidic hydroxyl that bridges Si and Al atoms in the zeolitic framework. As lanthanum loading increases, the intensity of both 3750 cm^{-1} and 3600 cm^{-1} decreases. The decrease in intensity of the 3600 cm^{-1} peak is consistent with the decrease in Bronsted acid sites observed by IPA-TPD measurement. The 3600 cm^{-1} peak can be deconvoluted into two components: 3592 cm^{-1} and 3611 cm^{-1}, representing the OH bands from eight-membered ring (8-MR) side pockets and twelve-membered ring (12-MR) main channels in MOR, respectively [155]. Via peak deconvolution, the distribution of the Bronsted sites from the 8-MR and the 12-MR can be known (**Figure 38**). It appears that at low La loadings, 12-MR sites are preferentially titrated (**Figure 37B**). This behavior is the opposite of sodium titration of MOR zeolite, where Na causes

a preferential titration of 8-MR sites [153, 156-158]. In the case of La, high concentration of lanthanum solution may cause large clusters of which proves to be difficult to titrate the smaller 8-MR side pockets. Interestingly, a broad peak around 3500 cm^{-1} increases in intensity as lanthanum loading increases. Klingenberg et al. studied FTIR characterizations of various lanthanum salts, and they found that the broad peak around 3500 cm^{-1} can be attributed to the OH group of the hydrated lanthanum species [159]. Therefore, as La loading increases, a higher concentration of hydrated lanthanum species will be present, thus increasing the intensity of the peak. This indicates the presence of lanthanum clusters within the zeolite pore, which was also observed in the XRD patterns.

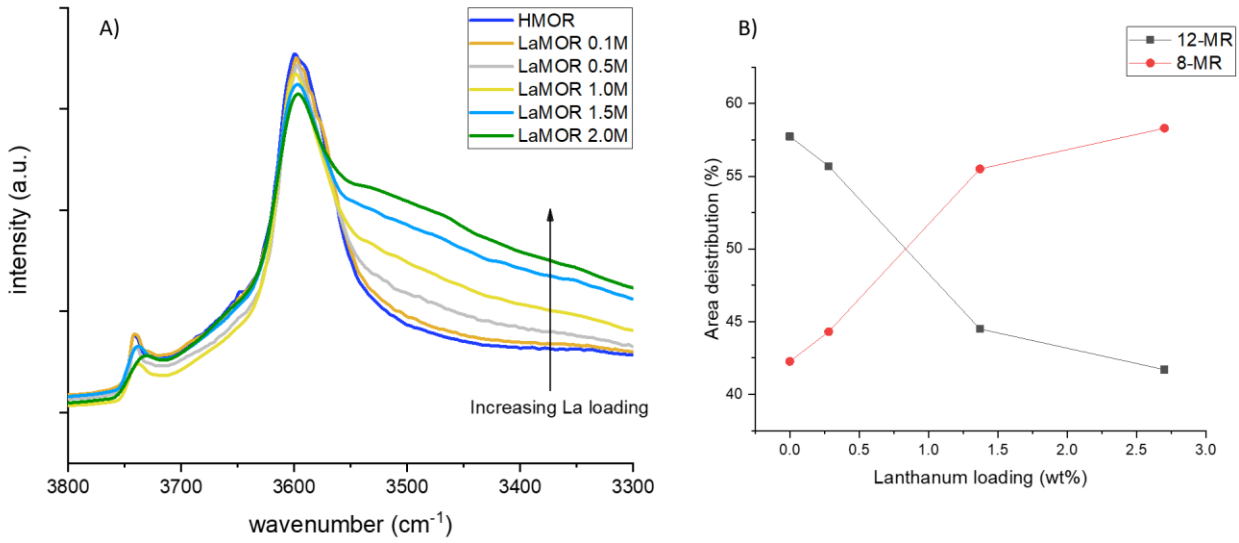

Figure 37. A) FTIR spectra of H-MOR and La-MOR samples, B) Area distribution of 8-MR and 12-MR Bronsted acid sites from the deconvolution of 3600 cm^{-1} peak.

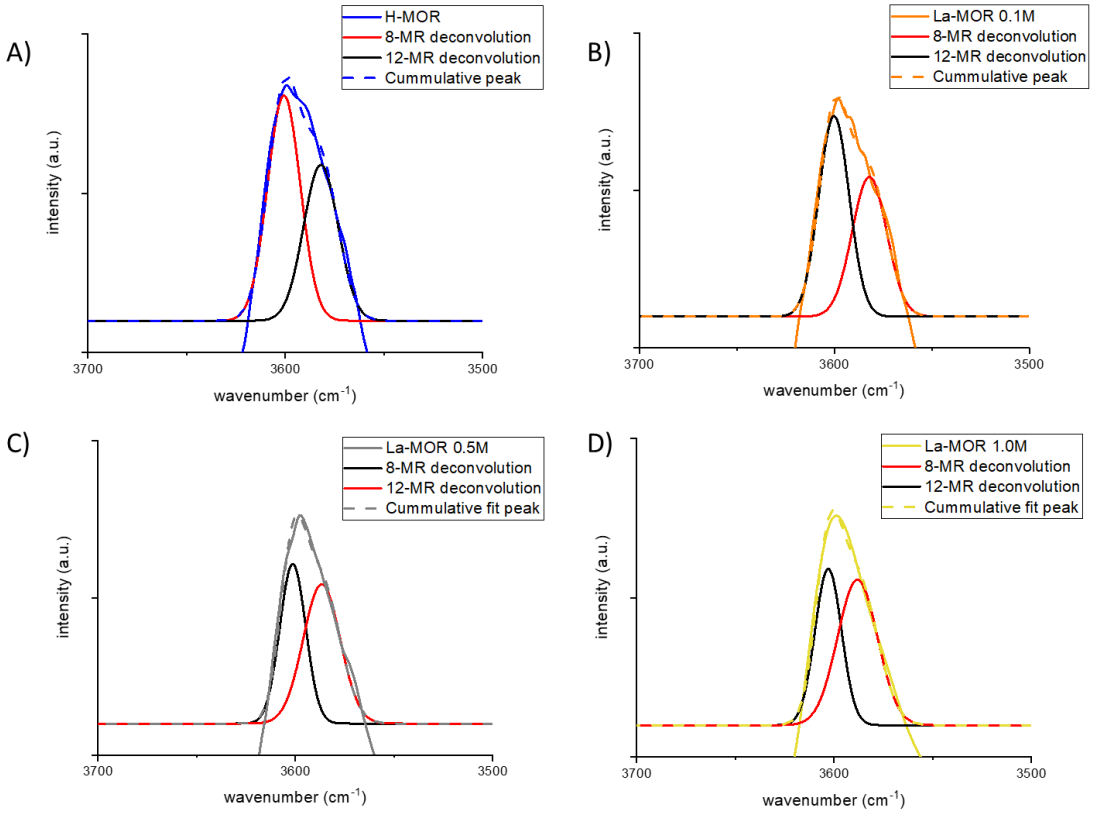

Figure 38. 3600 cm^{-1} peak deconvolution into 3592 cm^{-1} and 3611 cm^{-1} of A) H-MOR, B) La-MOR 0.1M, C) La-MOR 0.5M, La-MOR 1.0M

4.7.3 Alkylation Reaction

4.7.3.1 Reaction Pathways

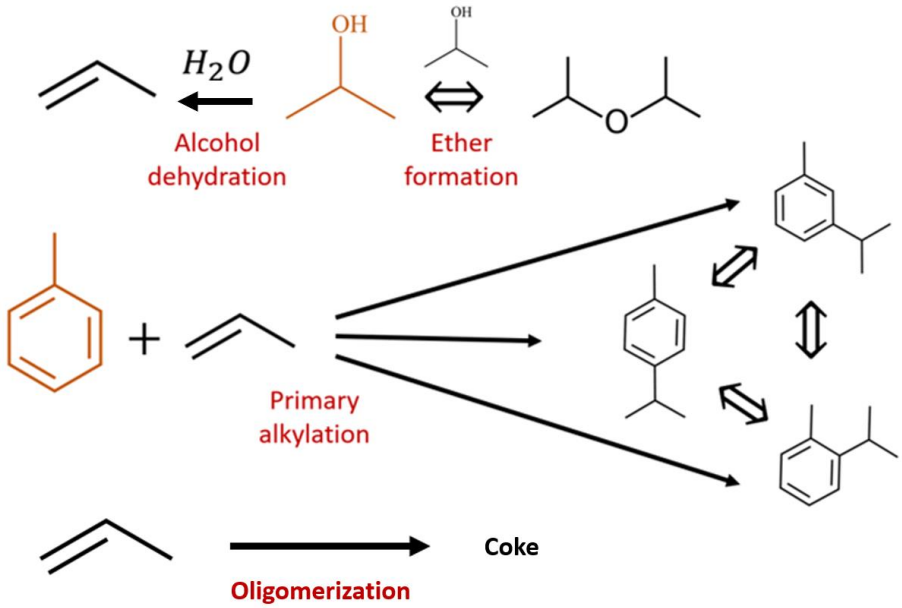

Figure 39. Reaction pathways in the alkylation reaction between toluene and isopropanol.

Under the reaction conditions of this work, the main products (>95%) that were observed from the alkylation reaction between toluene and isopropanol are propylene, diisopropyl ether, and the primary alkylated products: orto-, meta-, and para- cymene. A small amount of secondary alkylated products was also observed, which contributed to less than three percent selectivity of the total alkylated products. Propylene and diisoproyl ether were formed from dehydration of isopropanol over the Bronsted site [160-162]. The propylene will be the main alkylate, which will then react with toluene over the Bronsted acid site to form the primary alkylated products [43, 131, 163-165]. All three isomers of the alkylated products were present, and the main goal is to maximize the production of p-cymene due to the higher market demand. Considering the alkylated products are the rate limiting step, diisopropyl ether are assumed to be in equilibrium with isopropanol [164]. Propylene can also go through oligomerization reaction, which is common in

acidic zeolites and tends to be the main contribution of coke formation resulting in catalyst deactivation [166-168]. **Figure 39** shows the reaction pathways between toluene and isopropanol over MOR zeolite under this work's reaction conditions.

4.7.3.2 Shape selectivity

The primary alkylated products distribution for MOR catalysts at varying lanthanum loading in liquid phase reaction is depicted in **Figure 40**. In **Figure 40A**, at a similar reaction condition, the presence of La enhances the para-selectivity of the alkylated product and suppresses the orto-selectivity, even at a very small loading. This effect is further amplified with increasing La loading. These results suggest that the bulky alkylated product appears to be affected by the presence of lanthanum inside the pore. **Figure 40B** shows that this effect remains prominent at similar toluene conversion.

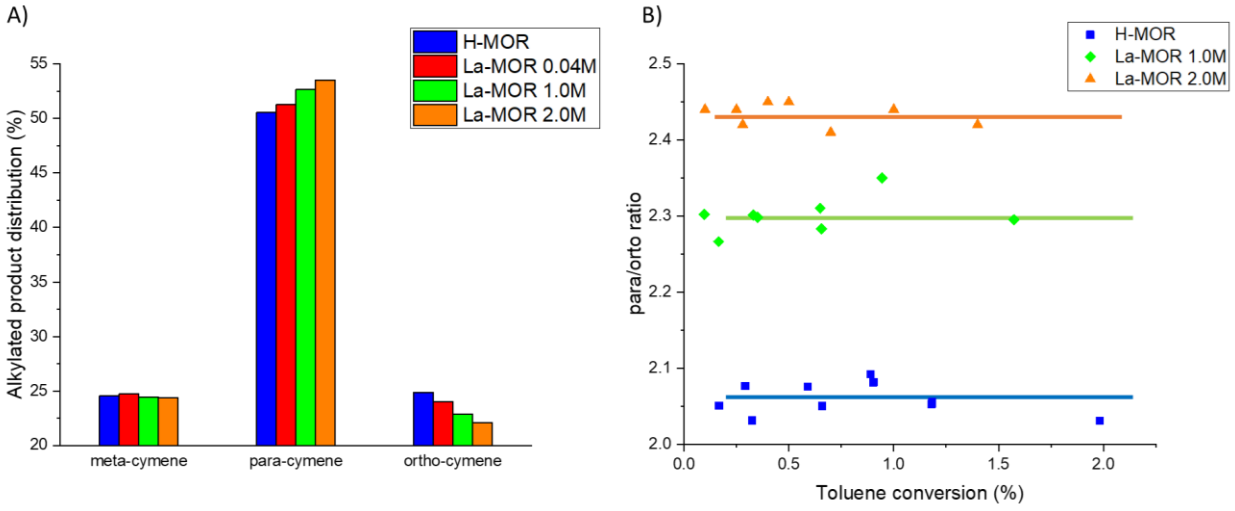

Figure 40. A) Alkylation product distribution for MOR catalysts at different La loading. Reaction conditions: 20 mins, 50 mL volume, 100 mg-cat, 0.5M isopropanol 1.0M toluene; B) ratio of para and orto-selectivity at varying toluene conversion in liquid phase.

4.7.3.3 Catalyst stability

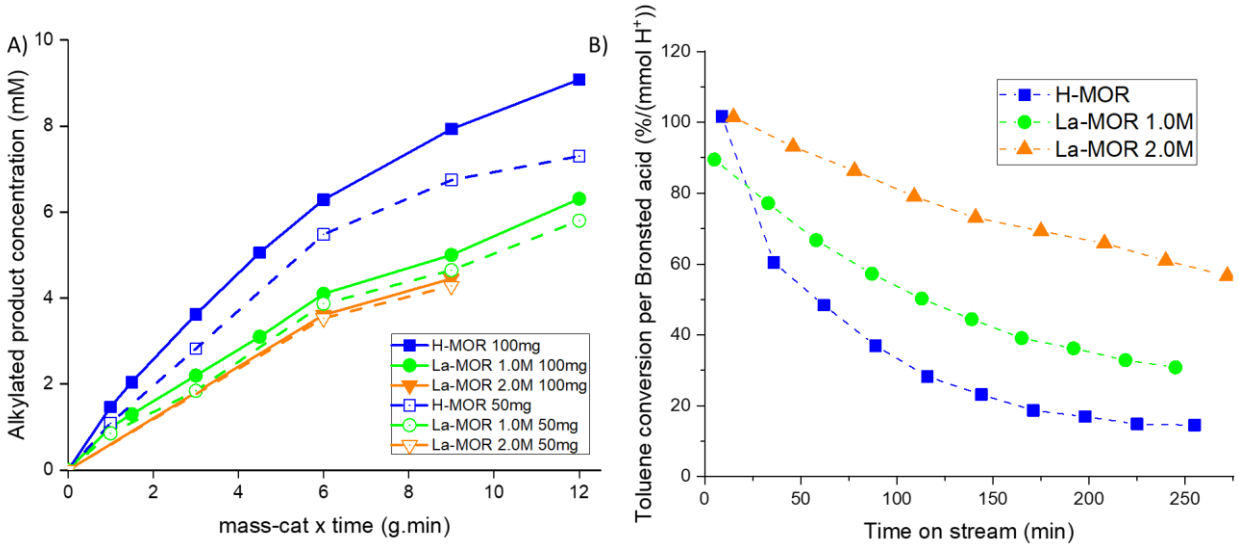

Figure 41. A) Liquid phase alkylation reaction. Concentration of alkylated products as a function of mass-cat x time for two different masses: 50 mg and 100 mg over H-MOR, La-MOR 1.0M, and La-MOR 2.0M. Reaction conditions: 220 ºC, 1.0M toluene and 2.0M isopropanol in cyclohexane, 50 mL total volume. B) Gas phase, continous flow alkylation reaction. Experimental data and deactivation model curve of toluene conversion as a function of time on stream. Reaction conditions: 5:1 mol toluene: isopropanol reactant mixture, 0.2 mL/hr reactant mixture injection rate, 220 C, 100 mL/min He, 1 atm, 200 mg catalyst.

The catalysts stability in performing alkylation reaction between toluene and isopropanol against coke formation was investigated in both liquid phase and gas phase. In liquid phase, from the products concentration bs mass-cat x time plot (**Figure 41A**), the degree of separation between 50mg and 100 mg for H-MOR appears to have the highest degree of separation, while La-MOR 2.0 is the least, This indicate that in liquid phase batch reaction, H-MOR experience the highest degree of deactivation, and La-MOR 2.0M has the least. On the other hand, in gas phase, a similar trend was observed where in the case of the lanthanum impregnated MOR samples, the catalyst lifetime is prolonged and deactivates less than the parent H-MOR (**Figure 41B**). **Table 14** summarizes that the addition of lanthanum decreases the deactivation coefficient in performing alkylation reaction in both liquid phase batch reactor and gas phase continuous flow reactor.

Table 14. Deactivation coefficient of alkylation reaction for all catalysts in both liquid phase batch reaction and gas phase continous flow reaction.

	Liquid phase, batch reaction	Gas phase, continuous flow reaction	
	βo (min^{-1})	Xo (%)	βo x 10^{-3} (min^{-1})
H-MOR	0.025	24.5	32.1
La-MOR 1.0M	0.018	15.5	8.17
La-MOR 2.0M	0.015	14.7	3.11

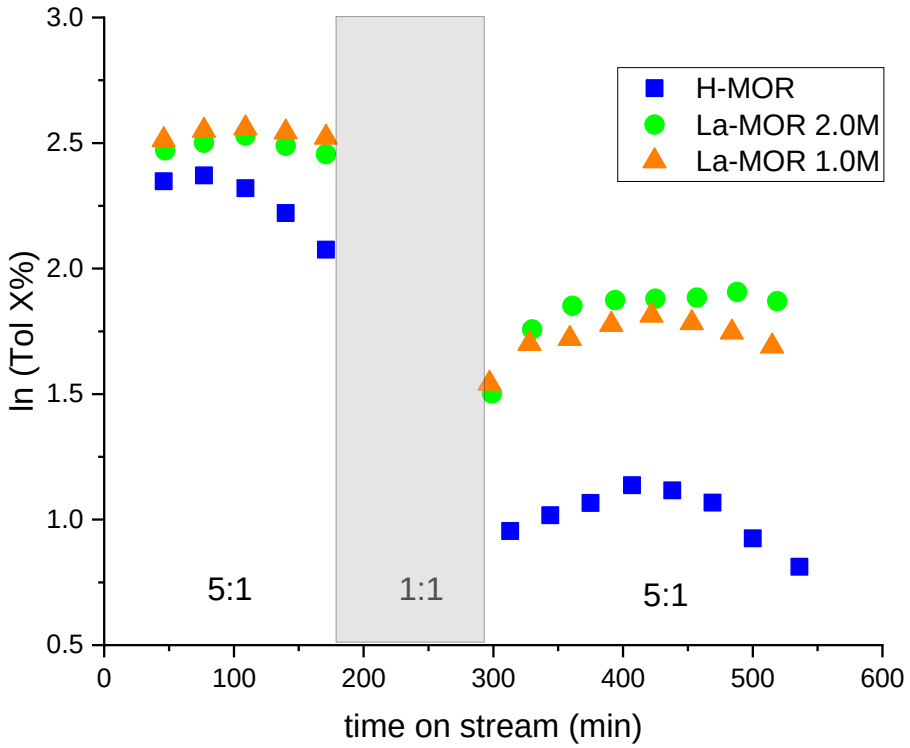

Figure 42. Changing toluene: isopropanol ratio to increase the degree of oligomerizations. Reaction conditions: 0.15 mL/hr reactant mixture injection rate, 220℃, 100 mL/min He, 100 mg cat, 1 atm

To further illustrate La ability to minimize deactivation, the catalysts were exposed to a higher partial pressure of isopropanol. The goal here is to increase the rate of olefin oligomerization, which causes a more severe catalyst deactivation due to a higher rate of coking [169, 170]. To do so, the reaction was initially conducted with a 5:1 toluene to isopropanol molar ratio for 150 min. Then, the ratio changed to 1:1 to allow for a higher degree of oligomerization. After 120 min, the

reaction was switched back to the 5:1 ratio. From **Figure 42**, we can see that both La-MOR 1.0M and La-MOR 2.0M were able to retain the alkylation activity much more than the regular H-MOR. Furthermore, the alkylation activity for La-MOR catalysts was maintained for a longer period after the 1:1 flow, while H-MOR experienced a further decrease in activity. This experiment further shows that La-MOR catalysts have higher stability against coking than H-MOR. To further understand the nature of the deactivation, the catalysts from the post reaction were further investigated.

4.7.4 Post Reaction Catalysts Characterizations

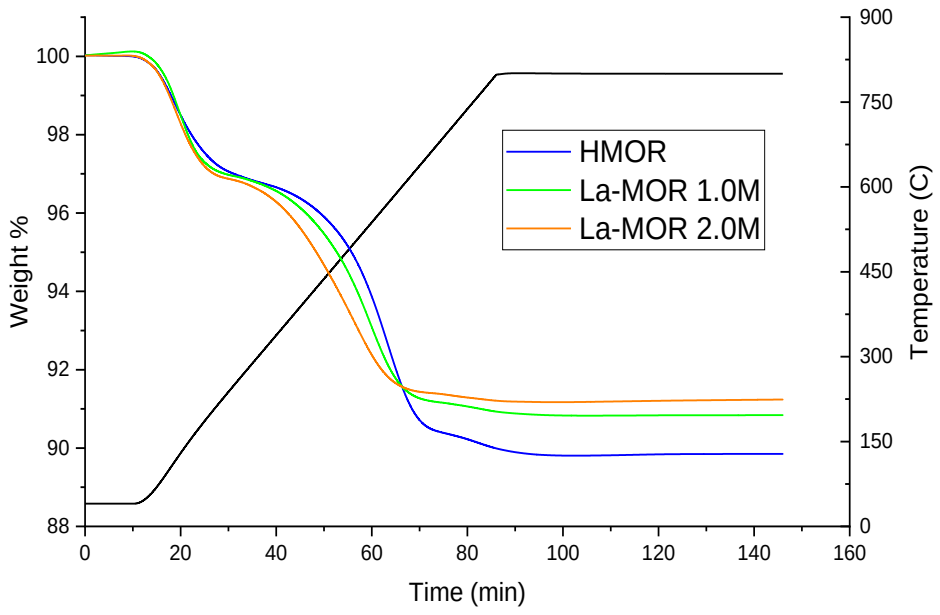

Figure 43. TGA curve of the spent catalyst from gas-phase reaction. Reaction conditions: 5:1 mol toluene: isopropanol reactant mixture, 0.2 mL/hr reactant mixture injection rate, 220℃, 300 min t.o.s., 100 mL/min He, 1 atm, 200 mg catalyst.

It was previously mentioned that the main contribution of the catalyst deactivation during the alkylation reaction was the coke formation via propylene oligomerization. Therefore, the spent catalysts were analyzed using TG-MS spectroscopy to investigate the amount of coke deposited and the nature of coke on the catalysts during the alkylation reaction. From the TGA curves

(**Figure 43**), the amount of coke deposited in H-MOR (7%) is higher than in the La-MOR 1.0 (6%) and La-MOR 2.0M (5.6%). These results correspond with the stability of the catalysts, as more coke deposits will result in a more severe catalyst deactivation by strongly titrating the acid sites available for reactions. These results are consistent with the Bronsted acid density of the post reaction catalysts, where La-MOR samples were able to retain the Bronsted acid site more than the parent H-MOR. Interestingly, the addition of lanthanum appears to lower the combustion temperature, indicating that La-MOR coke appears to burn off more easily compared to H-MOR. Note that this observation does not correlate with the extent of the reaction and the amount of coke deposited, as demonstrated by the combustion temperature of the coke deposited in H-MOR.

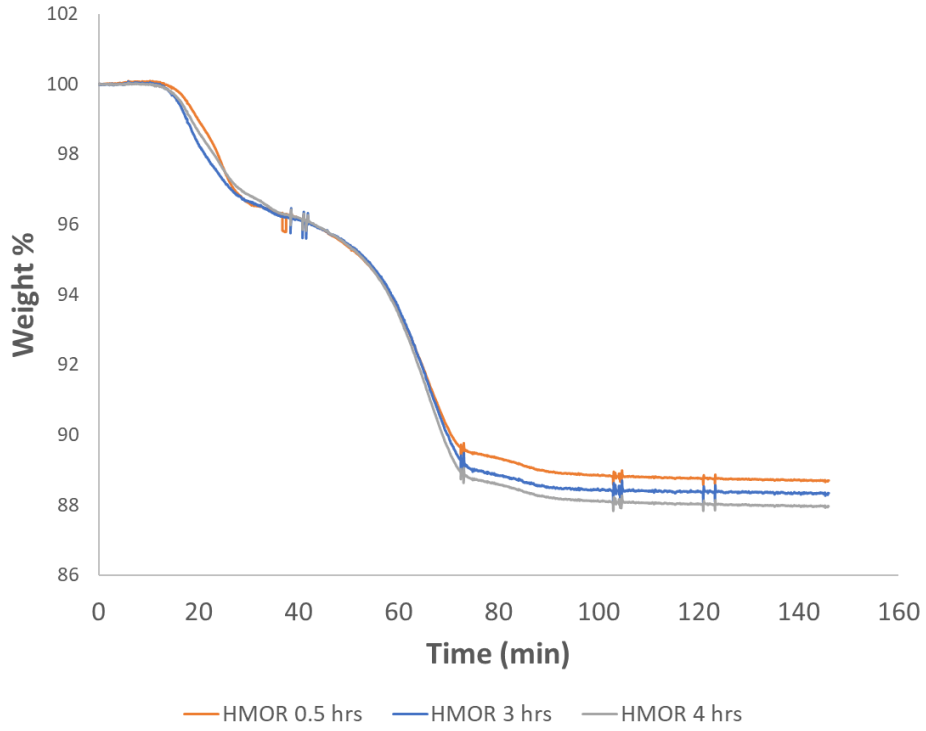

Figure 44. TGA curve of the spent catalyst of H-MOR from liquid-phase batch reaction at varying reaction time. Reaction conditions: 1.0M toluene, 1.0M isopropanol in cyclohexane, 50 mL, 300 rpm, 220℃, 300 psig, 100 mg catalyst.

The combustion temperature remains consistent across all runs at varying reaction temperatures but increases in coke content. (**Figure 44**). This suggests that the difference in the nature of the coke is strictly due to the presence of lanthanum inside the zeolite. Hence, the nature of coke was studied using mass spectroscopy of the evolved gas and ^{13}C MAS-NMR of the spent catalysts to understand why the lanthanum impregnated MOR samples require a lower coke oxidation temperature.

Table 15. Amount of coke deposited and Bronsted acid sites retained after reaction

	Amount of coke deposited (%)	Brosted acid site retained[a] (mmol/gcat)	Retained B acid densi
H-MOR	7.0	0.23	25
La-MOR 1.0M	6.0	0.41	50
La-MOR 2.0M	5.6	0.38	55

a) Reaction conditions: 5:1 mol toluene: isopropanol reactant mixture, 0.2 mL/hr reactant mixture injection rate, 220 C, 300 min t.o.s., 100 mL/min He, 1 atm, 200 mg catalyst.

Figure 45 shows the deconvolution of the MS signals from the evolved CO_2 and H_2O during the coke burning process of the spent catalysts. It has been demonstrated that hydrogen-rich coke is more easily oxidized than hydrogen-poor coke, which is more graphitic and requires a higher temperature to oxidize [171-173]. Therefore, the CO_2 MS signals are deconvoluted into two peaks. The first peak (dark red), centered around 220 ºC, represents hydrogen-rich coke, while the second peak (dark blue), centered around 235ºC, represents hydrogen-poor coke. On the other hand, by deconvoluting the H_2O MS curves, three peaks are the main interest: the first peak (green), centered around 208 ºC, represents adsorbed water; the second peak (dark red), centered around 220 ºC, represents hydrogen-rich coke; while the third (dark blue), centered around 235ºC represents hydrogen-poor coke. From the deconvolution, it is interesting to note that particularly the ratio of H_2O/CO_2 of the hydrogen-poor coke, La-MOR 2.0M is the highest by producing the most H2O and the least CO2, followed by La-MOR 1.0M and H-MOR. This suggests that the

heavier coke inside La-MOR catalysts is relatively richer in hydrogen, which explains the relatively lower temperature required to oxidize.

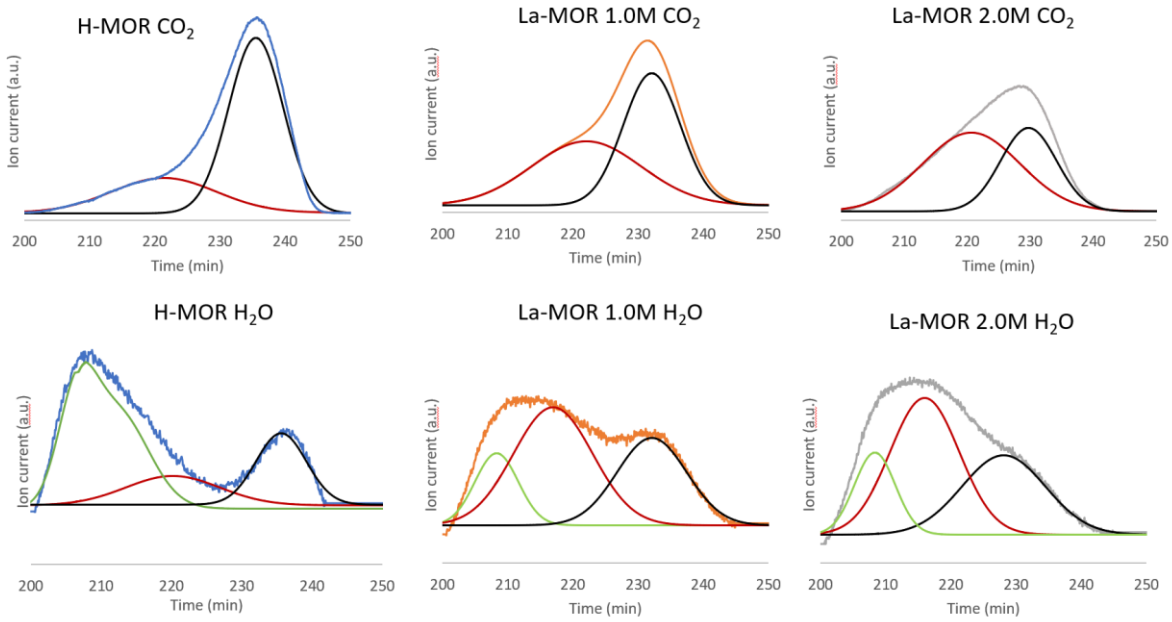

Figure 45. Deconvolution of the MS signals from evolved CO2 (m/z = 44) and H2O (m/z = 18) during the coke burning process of the spent catalysts from the gas-phase reaction.

To further understand the difference in nature of coke deposited in the catalysts, spent H-MOR and La-MOR 1.0M catalysts in liquid phase reaction. From **Figure 46B**, the difference in the ^{13}C MAS-NMR indicates a strong difference in the region 10-40 ppm, representing aliphatic carbons. **Figure 46C** shows that La-MOR 1.0M has a stronger signal at 15 ppm, 25-30 ppm, and 30-35, which represent methyl groups, short chains methylene groups, and long chains methylene groups, respectively [174]. These suggest that the coke in La-MOR 1.0M is more hydrogen-rich compared to the regular H-MOR since methyl groups and methylene groups make up a higher H/C ratio. This result would explain why the coke burnt off easier in the coke burning process.

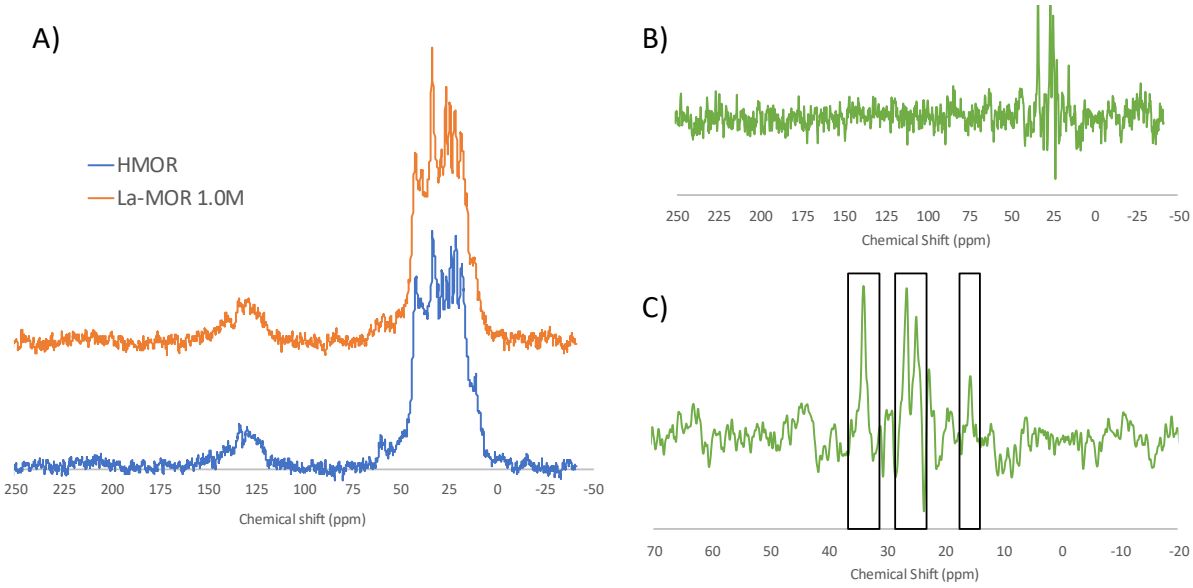

Figure 46. A) ^{13}C MAS-NMR of spent catalysts of H-MOR and La-MOR 1.0M in liquid phase; B) and C) the difference between the spectra. Reaction conditions: 20 mins, 50 mL volume, 100 mg-cat, 2.0M isopropanol, 1.0M toluene.

4.7.5 Isooctane cracking reaction

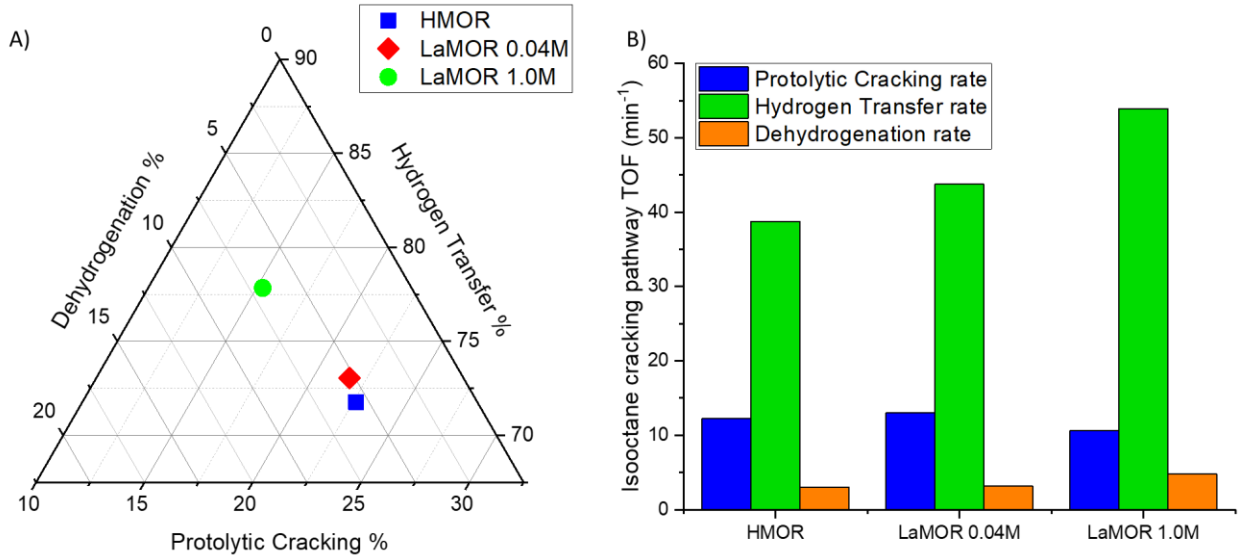

Figure 47. Isooctane cracking reaction A) Ternary plot of reaction pathways, B) Turnover frequency of reaction pathways. Reaction conditions: Approximately 10% isooctane conversion, 2.74 kPa isooctane partial pressure, continuous flow mode, 400°C, 80 mL/min N_2 carrier. Pretreatment: 0.5°C/min to 300°C and hold 1 h. Heat to 400°C at 2°C/min.

To understand the lanthanum's ability to improve the catalyst stability, we can analyze the different ways of minimizing oligomerization. One possibility is enhancing hydrogen transfer,

which would reduce the carbenium ion lifetime on the surface. We have recently shown that using isooctane cracking as a probe reaction, the catalyst ability to perform hydrogen transfer, protolytic cracking, and dehydrogenation can be quantified. This quantification can be represented in a ternary plot indicating the percentages in which an isooctane molecule can undergo each of the three reaction pathways. From the ternary plot (**Figure 47A**), it is seen that the addition of La increases the distribution towards hydrogen transfer. This enhancement is further illustrated by the significant increase in hydrogen transfer turnover frequency for the La-MOR samples (**Figure 47B**).

4.7.6 Comparing La-MOR and Na-MOR

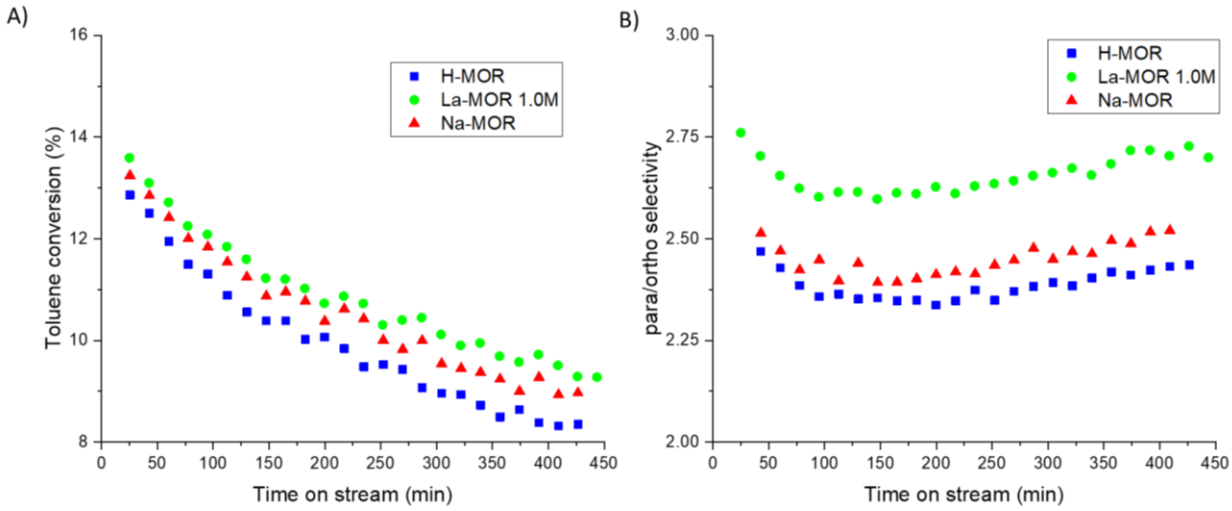

Figure 48. Alkylation reaction of H-MOR, La-MOR 1.0M and Na-MOR. Reaction conditions: 5:1 toluene to isopropanol. 0.2 mL/hr reactant mixture injection rate, 150 ºC, 100 mL/min He, 1 atm, 200 mg catalyst A) toluene conversion as a function of time on stream. B) Para- to ortho- cymene ratio as a function of time on stream.

Titration of Bronsted acid using Na cations have been shown to improve catalyst stability in zeolites [45]. To compare the roles of La and Na in MOR zeolite, a Na-MOR sample was prepared in such a way that the Bronsted acid density of Na-MOR (0.83 mmol/g) is within 3% of the La-MOR 1.0M Bronsted acid density. It appears that Na-MOR also improves the stability of MOR. Despite that, La-MOR has a better catalyst stability, indicating that the acid density is not the sole

reason for the improvement. Interestingly, the para/ortho ratio of the alkylated products is enhanced more significantly in La-MOR than in Na-MOR, suggesting a more significant role of La in improving the desired product selectivity.

4.8 Discussions

The addition of La constricts the micropore of zeolite resulting in enhanced shape selectivity to the alkylated product. BET, XRD and FTIR results are consistent with the presence of lanthanum clusters inside the zeolite pore, which results in a more constricted pore. This constriction favors the transport of the kinetically less bulky p-cymene product, restricting the kinetically bulkier o-cymene (**Figure 49A**). The addition of additives into zeolites is a common technique used in chemical industries to improve shape selectivity of the products. For instance, the incorporation of B and Mg into ZSM-5 zeolites have been shown to favor para-selectivity during toluene disproportionation reaction due to pore constriction [175].

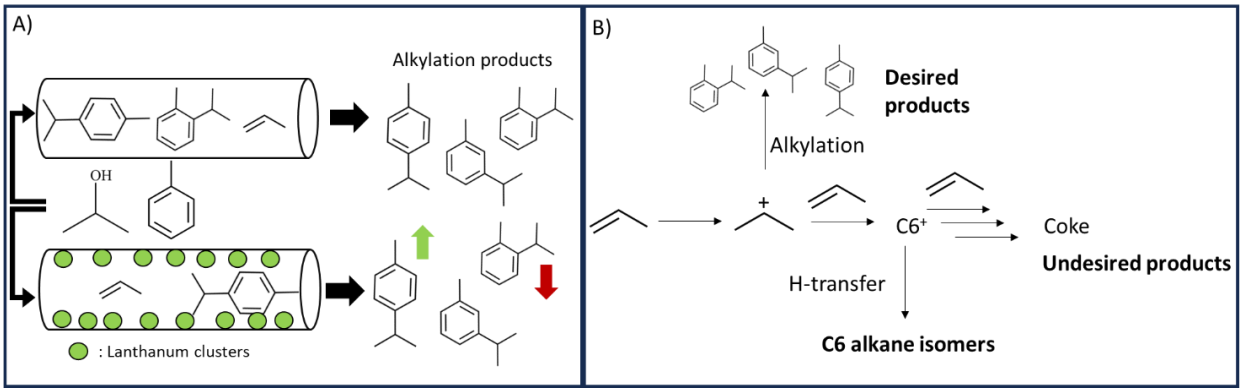

Figure 49. A) Lanthanum role in improving shape selectivity via pore constriction. B) Lanthanum role in improving catalyst stability by increasing the hydrogen transfer rate resulting in a lower carbenium ion lifetime on the surface.

Alkylation reaction results in both liquid and gas phase show that the addition of La to MOR zeolites improves catalyst stability. There are two potential reasons for this trend. The first reason can be the role of La in improving hydrogen transfer between the coke deposited on the surface and carbenium ion species [167, 176]. In fact, the isooctane cracking probe reaction showed that

the addition of La enhances hydrogen transfer rate when compared to regular H-MOR. From **Figure 49B**, this step is crucial in ensuring catalyst stability by shortening the carbenium ion lifetime that is susceptible to further oligomerization [29, 70, 177]. The enhancement in hydrogen transfer activity is attributed to the La capacity to improve intrinsic hydrogen transfer activity [29, 67] and/or its role in generating a more hydrogen-rich coke, which is the source of hydrogen [178]. Another factor contributing to enhanced stability is the reduction in Bronsted acid density. Increasing the Bronsted acid density has been shown to enhance the rate of olefin oligomerization [166, 179, 180]. Conversely, by reducing the density, both the rate and, consequently, coke formation are diminished. Sodium titration has been reported to enhance catalyst stability in aromatic alkylation reactions [45]. Consistent with this, this work reveals that titrating the MOR with Na improves catalyst stability. Therefore, the role of La in lowering the oligomerization rate can also be attributed to titrating Bronsted acid sites in the zeolite channels. It is noteworthy that La addition is found to improve stability when compared to a similar Bronsted acidity to Na-MOR, suggesting that the reduction in Bronsted acid density is not the sole contributor to enhanced stability. Additionally, lanthanum enhances the shape selectivity of the product, indicating its role in both product shape selectivity and catalyst stability. Nevertheless, it is crucial to acknowledge that sodium tends to preferentially titrate acid sites in the 8-MR channels, too small for alkylation reactions to occur [45], while lanthanum clusters occupy the 12-MR channels, as indicated by the deconvolution of the Bronsted FTIR peak.

4.9 Conclusion

In the alkylation of toluene with isopropanol, the incorporation of La within the MOR zeolite was observed to enhance para-selectivity while suppressing ortho-selectivity. The presence of La clusters constrains the zeolite pores, favoring the para-isomer, which is the kinetically less bulky

alkylated product. Additionally, La addition in MOR improves catalyst stability against coking, as evidenced by the decrease in the deactivation coefficient. La-MOR generates less coke than H-MOR, and the La-MOR coke exhibits easier combustion at a lower temperature than the H-MOR coke, indicating a difference in the nature of the coke. TG-MS and 13C-NMR analyses reveal that La-MOR coke has a higher H/C ratio than H-MOR coke. In the isooctane cracking reaction, the addition of lanthanum enhances hydrogen transfer activity. This increase in hydrogen transfer activity between the surface carbenium ion and deposited coke improves catalyst stability by reducing the carbenium ion's lifetime on the catalyst surface, leading to a lower degree of oligomerization. Comparing La-MOR to Na-MOR, lanthanum's role is to slightly improve catalyst stability and significantly enhance product selectivity, making lanthanum addition to MOR zeolite more appealing for the alkylation reaction between toluene and isopropanol.

References

[1] O. Roussak, H. Gesser, O. Roussak, H. Gesser, Crude Oil, Applied Chemistry: A Textbook for Engineers and Technologists, (2013) 41-55.

[2] T. Ahmad, D. Zhang, A critical review of comparative global historical energy consumption and future demand: The story told so far, Energy Reports, 6 (2020) 1973-1991.

[3] Oil and petroleum products explained: Refining crude oil, in, U.S. Energy Information Administration, 2023.

[4] A.M. Agnello, Petroleum-derived spray oils: chemistry, history, refining and formulation, Spray oils beyond 2000, (2002) 2-18.

[5] A. Corma, E. Corresa, Y. Mathieu, L. Sauvanaud, S. Al-Bogami, M. Al-Ghrami, A. Bourane, Crude oil to chemicals: light olefins from crude oil, Catalysis Science & Technology, 7 (2017) 12-46.

[6] A. Nicholson, The Fossil-Based BTX Market, Industrial Arene Chemistry: Markets, Technologies, Sustainable Processes and Cases Studies of Aromatic Commodities, 1 (2023) 1-18.

[7] R. Notz, I. Toennies, N. McCann, G. Scheffknecht, H. Hasse, CO2 Capture for Fossil Fuel-Fired Power Plants, Chemical Engineering & Technology, 34 (2011) 163-172.

[8] T. Nagy, P. Mizsey, Effect of fossil fuels on the parameters of CO2 capture, Environmental science & technology, 47 (2013) 8948-8954.

[9] M. Marder, T. Patzek, S.W. Tinker, Physics, fracking, fuel, and the future, Physics Today, 69 (2016) 46-52.

[10] A. Corma, A. Martínez, Zeolites and ordered mesoporous materials: Progress and prospects, Stud. Surf. Sci. Catal, 157 (2005) 337-366.

[11] A. Corma, State of the art and future challenges of zeolites as catalysts, Journal of Catalysis, 216 (2003) 298-312.

[12] V. Verdoliva, M. Saviano, S. De Luca, Zeolites as acid/basic solid catalysts: Recent synthetic developments, Catalysts, 9 (2019) 248.

[13] B.M. Weckhuysen, J. Yu, Recent advances in zeolite chemistry and catalysis, Chemical Society Reviews, 44 (2015) 7022-7024.

[14] J. Li, A. Corma, J. Yu, Synthesis of new zeolite structures, Chemical Society Reviews, 44 (2015) 7112-7127.

[15] G. Sartori, R. Maggi, Use of solid catalysts in Friedel− Crafts acylation reactions, Chemical Reviews, 106 (2006) 1077-1104.

[16] A. Corma, From microporous to mesoporous molecular sieve materials and their use in catalysis, Chemical reviews, 97 (1997) 2373-2420.

[17] J.W. Ward, The nature of active sites on zeolites: I. The decationated Y zeolite, Journal of catalysis, 9 (1967) 225-236.

[18] Q. Zhang, S. Gao, J. Yu, Metal sites in zeolites: synthesis, characterization, and catalysis, Chemical reviews, 123 (2022) 6039-6106.

[19] R. Harjula, A. Dyer, S.D. Pearson, R.P. Townsend, Ion exchange in zeolites. Part 1.—Prediction of Ca2+–Na+ equilibria in zeolites X and Y, Journal of the Chemical Society, Faraday Transactions, 88 (1992) 1591-1597.

[20] J.A. Kaduk, J. Faber, Crystal structure of zeolite Y as a function of ion exchange, Rigaku J, 12 (1995) 14-34.

[21] H.S. Sherry, Ion-exchange properties of zeolites. IV. Alkaline earth ion exchange in the synthetic zeolites Linde X and Y, The Journal of Physical Chemistry, 72 (1968) 4086-4094.

[22] M. Shamzhy, M. Opanasenko, P. Concepción, A. Martínez, New trends in tailoring active sites in zeolite-based catalysts, Chemical Society Reviews, 48 (2019) 1095-1149.

[23] K. Chen, M. Abdolrahmani, S. Horstmeier, T.N. Pham, V.T. Nguyen, M. Zeets, B. Wang, S. Crossley, J.L. White, Brønsted–Brønsted synergies between framework and noncrystalline protons in zeolite H-ZSM-5, ACS Catalysis, 9 (2019) 6124-6136.

[24] T.N. Pham, V. Nguyen, H. Nguyen-Phu, B. Wang, S. Crossley, Influence of Brønsted Acid Site Proximity on Alkane Cracking in MFI Zeolites, ACS Catalysis, 13 (2023) 1359-1370.

[25] G. Li, E.A. Pidko, The nature and catalytic function of cation sites in zeolites: a computational perspective, ChemCatChem, 11 (2019) 134-156.

[26] E. Sousa-Aguiar, Y Zeolites as a major component of FCC catalysts: Main challenges in the modification thereof, in: Zeolites and Zeolite-Like Materials, Elsevier, 2016, pp. 265-282.

[27] F. Trigueiro, D. Monteiro, F. Zotin, E.F. Sousa-Aguiar, Thermal stability of Y zeolites containing different rare earth cations, Journal of alloys and compounds, 344 (2002) 337-341.

[28] E.F. Sousa-Aguiar, F.E. Trigueiro, F.M.Z. Zotin, The role of rare earth elements in zeolites and cracking catalysts, Catalysis today, 218 (2013) 115-122.

[29] F. Schüßler, E.A. Pidko, R. Kolvenbach, C. Sievers, E.J. Hensen, R.A. van Santen, J.A. Lercher, Nature and location of cationic lanthanum species in high alumina containing faujasite type zeolites, The Journal of Physical Chemistry C, 115 (2011) 21763-21776.

[30] E.F. Lee, L.V. Rees, Effect of calcination on location and valency of lanthanum ions in zeolite Y, Zeolites, 7 (1987) 143-147.

[31] E.F. Lee, L.V. Rees, Dehydroxylation of lanthanum exchanged zeolite Y, Zeolites, 7 (1987) 545-548.

[32] S. Yu, J. Yan, W. Lin, J. Long, S.-B. Liu, Effects of lanthanum incorporation on stability, acidity and catalytic performance of Y zeolites, Catalysis Letters, 151 (2021) 698-712.

[33] S. Kotrel, H. Knözinger, B. Gates, The Haag–Dessau mechanism of protolytic cracking of alkanes, Microporous and Mesoporous Materials, 35 (2000) 11-20.

[34] A. Corma, A. Orchillés, Current views on the mechanism of catalytic cracking, Microporous and mesoporous materials, 35 (2000) 21-30.

[35] A. Corma, P.J. Miguel, A.V. Orchilles, The role of reaction temperature and cracking catalyst characteristics in determining the relative rates of protolytic cracking, chain propagation, and hydrogen transfer, Journal of catalysis, 145 (1994) 171-180.

[36] G. de la Puente, U.A. Sedran, The energy gradient selectivity concept and the routes of paraffin cracking in FCC catalysts, Journal of Catalysis, 179 (1998) 36-42.

[37] V. Fierro, Y. Schuurman, C. Mirodatos, J. Duplan, J. Verstraete, Study of the cracking reaction of linear and branched hexanes under protolytic conditions by non-stationary kinetics, Chemical Engineering Journal, 90 (2002) 139-147.

[38] R. Gounder, E. Iglesia, Catalytic hydrogenation of alkenes on acidic zeolites: Mechanistic connections to monomolecular alkane dehydrogenation reactions, Journal of catalysis, 277 (2011) 36-45.

[39] G.M. Mullen, M.J. Janik, Density functional theory study of alkane-alkoxide hydride transfer in zeolites, Acs Catalysis, 1 (2011) 105-115.

[40] J. Martens, P. Jacobs, J. Weitkamp, Attempts to rationalize the distribution of hydrocracked products. I qualitative description of the primary hydrocracking modes of long chain paraffins in open zeolites, Applied Catalysis, 20 (1986) 239-281.

[41] J. Weitkamp, Catalytic hydrocracking—mechanisms and versatility of the process, ChemCatChem, 4 (2012) 292-306.

[42] H. Krannila, W. Haag, B. Gates, Monomolecular and bimolecular mechanisms of paraffin cracking: n-butane cracking catalyzed by HZSM-5, Journal of catalysis, 135 (1992) 115-124.

[43] C. Perego, P. Pollesel, Advances in aromatics processing using zeolite catalysts, Advances in Nanoporous Materials, 1 (2010) 97-149.

[44] A. Marchese, C.R. Arciola, R. Barbieri, A.S. Silva, S.F. Nabavi, A.J. Tsetegho Sokeng, M. Izadi, N.J. Jafari, I. Suntar, M. Daglia, Update on monoterpenes as antimicrobial agents: A particular focus on p-cymene, Materials, 10 (2017) 947.

[45] K. Ithisuphalap, Nolen, M.A., Monroe, H. and Kwon, S., Kinetic, Spectroscopic, and Theoretical Study of Toluene Alkylation with Ethylene on Acidic Mordenite Zeolite, ACS Catalysis, 13 (2023) 16012-16031.

[46] G. McLellan, R.F. Howe, L. Parker, D. Bibby, Effects of coke formation on the acidity of ZSM-5, J. Catal.;(United States), 99 (1986).

[47] J. Huang, Y. Jiang, V.R. Marthala, A. Bressel, J. Frey, M. Hunger, Effect of pore size and acidity on the coke formation during ethylbenzene conversion on zeolite catalysts, Journal of Catalysis, 263 (2009) 277-283.

[48] H. Karge, Coke formation on zeolites, in: Studies in surface science and catalysis, Elsevier, 1991, pp. 531-570.

[49] J. Scherzer, Octane-enhancing, zeolitic FCC catalysts: scientific and technical aspects, Catalysis Reviews—Science and Engineering, 31 (1989) 215-354.

[50] M.C. Galiano, U.A. Sedran, Light alkene selectivity on Y zeolite FCC catalysts, Industrial & engineering chemistry research, 36 (1997) 4207-4211.

[51] H. Cerqueira, G. Caeiro, L. Costa, F.R. Ribeiro, Deactivation of FCC catalysts, Journal of molecular catalysis A: Chemical, 292 (2008) 1-13.

[52] J. Figueiredo, M. Pinto, J. Órfa, Adsorption of propene and coke formation on a cracking catalyst (FCC), Applied Catalysis A: General, 104 (1993) 1-9.

[53] J. Scherzer, Designing FCC catalysts with high-silica Y zeolites, Applied catalysis, 75 (1991) 1-32.

[54] J. Zhou, J. Zhao, J. Zhang, T. Zhang, M. Ye, Z. Liu, Regeneration of catalysts deactivated by coke deposition: A review, Chinese Journal of Catalysis, 41 (2020) 1048-1061.

[55] R. Maya-Yescas, D. Bogle, F. López-Isunza, Approach to the analysis of the dynamics of industrial FCC units, Journal of Process Control, 8 (1998) 89-100.

[56] E. Benazzi, T. Chapus, T. Cheron, H. Cauffriez, C. Marcilly, Relationship between zeolite structure and hydrogen-transfer reactions in naphthenes and paraffins cracking, in: Studies in Surface Science and Catalysis, Elsevier, 1994, pp. 1663-1669.

[57] R.J. Pellet, Hydrogen transfer catalysis by platinum on zeolites, Journal of Catalysis, 177 (1998) 40-52.

[58] J. Abbot, B. Wojciechowski, Hydrogen transfer reactions in the catalytic cracking of paraffins, Journal of Catalysis, 107 (1987) 451-462.

[59] A. Corma, P. Miguel, A. Orchillés, Product selectivity effects during cracking of alkanes at very short and longer times on stream, Applied Catalysis A: General, 138 (1996) 57-73.

[60] A. Brait, A. Koopmans, H. Weinstabl, A. Ecker, K. Seshan, J.A. Lercher, Hexadecane conversion in the evaluation of commercial fluid catalytic cracking catalysts, Industrial & engineering chemistry research, 37 (1998) 873-881.

[61] R. Shigeishi, A. Garforth, I. Harris, J. Dwyer, The conversion of butanes in HZSM-5, Journal of Catalysis, 130 (1991) 423-439.

[62] E.A. Lombardo, W.K. Hall, The mechanism of isobutane cracking over amorphous and crystalline aluminosilicates, Journal of Catalysis, 112 (1988) 565-578.

[63] D. Wallenstein, R. Harding, The dependence of ZSM-5 additive performance on the hydrogen-transfer activity of the REUSY base catalyst in fluid catalytic cracking, Applied Catalysis A: General, 214 (2001) 11-29.

[64] M.A. Sanchez-Castillo, N. Agarwal, A. Bartsch, R.D. Cortright, R.J. Madon, J. Dumesic, Reaction kinetics studies and analyses of isobutane conversion over H-mordenite and β-zeolite, Journal of Catalysis, 218 (2003) 88-103.

[65] G. de la Puente, U. Sedran, Evaluation of hydrogen transfer in FCC catalysts. A new approach for cyclohexene as a test reactant, Chemical engineering science, 55 (2000) 759-765.

[66] A. Feller, I. Zuazo, A. Guzman, J.O. Barth, J.A. Lercher, Common mechanistic aspects of liquid and solid acid catalyzed alkylation of isobutane with n-butene, Journal of Catalysis, 216 (2003) 313-323.

[67] A. Guzman, I. Zuazo, A. Feller, R. Olindo, C. Sievers, J.A. Lercher, On the formation of the acid sites in lanthanum exchanged X zeolites used for isobutane/cis-2-butene alkylation, Microporous and mesoporous materials, 83 (2005) 309-318.

[68] G.S. Nivarthy, A. Feller, K. Seshan, J.A. Lercher, The role of hydride transfer in zeolite catalyzed isobutane/butene alkylation, in: Studies in Surface Science and Catalysis, Elsevier, 2000, pp. 2561-2566.

[69] G.S. Nivarthy, K. Seshan, J.A. Lercher, The influence of acidity on zeolite H-BEA catalyzed isobutane/n-butene alkylation, Microporous and mesoporous materials, 22 (1998) 379-388.

[70] V.B. Höpfl, T. Schachtl, Y. Liu, J.A. Lercher, Pellet size-induced increase in catalyst stability and yield in zeolite-catalyzed 2-butene/isobutane alkylation, Industrial & Engineering Chemistry Research, 61 (2022) 330-338.

[71] T.F. Degnan Jr, Applications of zeolites in petroleum refining, Topics in Catalysis, 13 (2000) 349-356.

[72] V. Komvokis, L.X.L. Tan, M. Clough, S.S. Pan, B. Yilmaz, Zeolites in fluid catalytic cracking (FCC), Zeolites in Sustainable Chemistry: Synthesis, Characterization and Catalytic Applications, (2016) 271-297.

[73] H. Yuan, C. Li, R. Shan, J. Zhang, Y. Wu, Y. Chen, Recent developments on the zeolites catalyzed polyolefin plastics pyrolysis, Fuel Processing Technology, 238 (2022) 107531.

[74] A. Susastriawan, A. Sandria, Experimental study the influence of zeolite size on low-temperature pyrolysis of low-density polyethylene plastic waste, Thermal Science and Engineering Progress, 17 (2020) 100497.

[75] R. Miandad, M. Barakat, M. Rehan, A. Aburiazaiza, I. Ismail, A. Nizami, Plastic waste to liquid oil through catalytic pyrolysis using natural and synthetic zeolite catalysts, Waste Management, 69 (2017) 66-78.

[76] I. Vollmer, M.J. Jenks, R. Mayorga González, F. Meirer, B.M. Weckhuysen, Plastic waste conversion over a refinery waste catalyst, Angewandte Chemie International Edition, 60 (2021) 16101-16108.

[77] W. Haag, R. Dessau, R. Lago, Kinetics and mechanism of paraffin cracking with zeolite catalysts, in: Studies in Surface Science and Catalysis, Elsevier, 1991, pp. 255-265.

[78] F.C. Jentoft, B.C. Gates, Solid-acid-catalyzed alkane cracking mechanisms: evidence from reactions of small probe molecules, Topics in catalysis, 4 (1997) 1-13.

[79] A. Corma, J. Planelles, J. Sanchez-Marin, F. Tomas, The role of different types of acid site in the cracking of alkanes on zeolite catalysts, Journal of Catalysis, 93 (1985) 30-37.

[80] Y.V. Kissin, Chemical mechanism of hydrocarbon cracking over solid acidic catalysts, Journal of catalysis, 163 (1996) 50-62.

[81] Y.V. Kissin, Chemical mechanisms of catalytic cracking over solid acidic catalysts: alkanes and alkenes, Catalysis Reviews, 43 (2001) 85-146.

[82] P.G. Smirniotis, E. Ruckenstein, Comparison of the Performance of ZSM-5,. beta. Zeolite, Y, USY, and Their Composites in the Catalytic Cracking of n-Octane, 2, 2, 4-Trimethylpentane, and 1-Octene, Industrial & engineering chemistry research, 33 (1994) 800-813.

[83] R. Van Borm, A. Aerts, M.-F. Reyniers, J.A. Martens, G.B. Marin, Catalytic cracking of 2, 2, 4-trimethylpentane on FAU, MFI, and bimodal porous materials: influence of acid properties and pore topology, Industrial & engineering chemistry research, 49 (2010) 6815-6823.

[84] H.C. Beirnaert, J.R. Alleman, G.B. Marin, A fundamental kinetic model for the catalytic cracking of alkanes on a USY zeolite in the presence of coke formation, Industrial & engineering chemistry research, 40 (2001) 1337-1347.

[85] J. Lopes, F. Lemos, F.R. Ribeiro, E. Derouane, A comparison of the catalytic properties of SAPO-37 and HY zeolite in the cracking of n-heptane and 2, 2, 4-trimethylpentane, in: Studies in Surface Science and Catalysis, Elsevier, 1991, pp. 365-372.

[86] A.A. Brillis, G. Manos, Deactivation Studies During Catalytic Cracking of C 8 Aliphatic Hydrocarbons over Ultrastable Y-Zeolite. Conversion and Product Yield Profiles with Time Onstream, Catalysis letters, 91 (2003) 185-191.

[87] J. Engelhardt, W.K. Hall, Contribution to the understanding of the reaction chemistry of isobutane and neopentane over acid catalysts, I, Journal of Catalysis, 125 (1990) 472-487.

[88] J. Abbot, B. Wojciechowski, The mechanism of paraffin reactions on HY zeolite, Journal of Catalysis, 115 (1989) 1-15.

[89] J. Abbot, Reactions of 3-methylpentane and 2, 3-dimethylbutane on aluminosilicate catalysts, Journal of Catalysis, 126 (1990) 628-642.

[90] P.O. Fritz, J.H. Lunsford, The effect of sodium poisoning on dealuminated Y-type zeolites, Journal of Catalysis, 118 (1989) 85-98.

[91] C.V. Hidalgo, H. Itoh, T. Hattori, M. Niwa, Y. Murakami, Measurement of the acidity of various zeolites by temperature-programmed desorption of ammonia, Journal of Catalysis, 85 (1984) 362-369.

[92] H.K. Chau, H.D. Mai, A. Gumidyala, T.N. Pham, D.-P. Bui, A.D. D'Amico, I. Alalq, D.T. Glatzhofer, J.L. White, S.P. Crossley, Effect of water on cumene dealkylation over H-ZSM-5 zeolites, ACS Catalysis, 13 (2023) 9158-9170.

[93] T.N. Pham, V. Nguyen, B. Wang, J.L. White, S. Crossley, Quantifying the influence of water on the mobility of aluminum species and their effects on alkane cracking in zeolites, ACS Catalysis, 11 (2021) 6982-6994.

[94] K. Chen, A. Zornes, V. Nguyen, B. Wang, Z. Gan, S.P. Crossley, J.L. White, 17O Labeling Reveals Paired Active Sites in Zeolite Catalysts, Journal of the American Chemical Society, 144 (2022) 16916-16929.

[95] C. Liu, G. Li, E.J. Hensen, E.A. Pidko, Relationship between acidity and catalytic reactivity of faujasite zeolite: A periodic DFT study, Journal of Catalysis, 344 (2016) 570-577.

[96] B. Mezari, P.C. Magusin, S.M. Almutairi, E.A. Pidko, E.J. Hensen, Nature of enhanced Brønsted acidity induced by extraframework aluminum in an ultrastabilized faujasite zeolite: an in situ NMR study, The Journal of Physical Chemistry C, 125 (2021) 9050-9059.

[97] W. Li, S.Y. Yu, G.D. Meitzner, E. Iglesia, Structure and properties of cobalt-exchanged H-ZSM5 catalysts for dehydrogenation and dehydrocyclization of alkanes, The Journal of Physical Chemistry B, 105 (2001) 1176-1184.

[98] B. Hu, N.M. Schweitzer, U. Das, H. Kim, J. Niklas, O. Poluektov, L.A. Curtiss, P.C. Stair, J.T. Miller, A.S. Hock, Selective propane dehydrogenation with single-site CoII on SiO2 by a non-redox mechanism, Journal of Catalysis, 322 (2015) 24-37.

[99] S.Y. Yu, G.J. Yu, W. Li, E. Iglesia, Kinetics and reaction pathways for propane dehydrogenation and aromatization on Co/H-ZSM5 and H-ZSM5, The Journal of Physical Chemistry B, 106 (2002) 4714-4720.

[100] M.A. Sanchez-Castillo, R.J. Madon, J.A. Dumesic, Role of rare earth cations in Y zeolite for hydrocarbon cracking, The Journal of Physical Chemistry B, 109 (2005) 2164-2175.

[101] G. de la Puente, E.F. Souza-Aguiar, F.M.a.Z. Zotin, V.L.D. Camorim, U. Sedran, Influence of different rare earth ions on hydrogen transfer over Y zeolite, Applied Catalysis A: General, 197 (2000) 41-46.

[102] C. Sievers, A. Onda, A. Guzman, K.S. Otillinger, R. Olindo, J.A. Lercher, Low-temperature activation of branched octane isomers over lanthanum-exchanged zeolite X catalysts, The Journal of Physical Chemistry C, 111 (2007) 210-218.

[103] C. Sievers, A. Onda, A. Guzman, R. Olindo, J.A. Lercher, Surface chemistry of branched alkanes on lanthanum exchange zeolite X, in: Studies in surface science and catalysis, Elsevier, 2007, pp. 1153-1160.

[104] R.C. Shiery, S.J. McElhany, D.C. Cantu, Effect of lanthanum ions on the Brønsted acidity of faujasite and implications for hydrothermal stability, The Journal of Physical Chemistry C, 125 (2021) 13649-13657.

[105] P. Sazama, J. Dědeček, V. Gabova, B. Wichterlova, G. Spoto, S. Bordiga, Effect of aluminium distribution in the framework of ZSM-5 on hydrocarbon transformation. Cracking of 1-butene, Journal of Catalysis, 254 (2008) 180-189.

[106] S. Krishnaswamy, J. Kittrell, Deactivation disguised kinetics, Industrial & Engineering Chemistry Process Design and Development, 17 (1978) 200-204.

[107] J.N. Louwen, S. Simko, K. Stanciakova, R.E. Bulo, B.M. Weckhuysen, E.T. Vogt, Role of rare earth ions in the prevention of dealumination of zeolite Y for fluid cracking catalysts, The Journal of Physical Chemistry C, 124 (2020) 4626-4636.

[108] F. Lemos, F.R. Ribeiro, M. Kern, G. Giannetto, M. Guisnet, Influence of lanthanum content of LaHY catalysts on their physico-chemical and catalytic properties: Comparison with CeHY catalysts, Applied catalysis, 39 (1988) 227-237.

[109] J. Huang, Y. Jiang, V.R. Marthala, Y.S. Ooi, J. Weitkamp, M. Hunger, Concentration and acid strength of hydroxyl groups in zeolites La, Na-X and La, Na-Y with different lanthanum exchange degrees studied by solid-state NMR spectroscopy, Microporous and mesoporous materials, 104 (2007) 129-136.

[110] R. Carvajal, P.-J. Chu, J.H. Lunsford, The role of polyvalent cations in developing strong acidity: a study of lanthanum-exchanged zeolites, Journal of Catalysis, 125 (1990) 123-131.

[111] C. Deng, J. Zhang, L. Dong, M. Huang, B. Li, G. Jin, J. Gao, F. Zhang, M. Fan, L. Zhang, The effect of positioning cations on acidity and stability of the framework structure of Y zeolite, Scientific reports, 6 (2016) 23382.

[112] A. Zornes, N.B. Abdul Rahman, O.R. Das, L.A. Gomez, S. Crossley, D.E. Resasco, J.L. White, Impact of Low-Temperature Water Exposure and Removal on Zeolite HY, Journal of the American Chemical Society, 146 (2023) 1132-1143.

[113] R. Zhang, S. Xu, D. Raja, N.B. Khusni, J. Liu, J. Zhang, S. Abdulridha, H. Xiang, S. Jiang, Y. Guan, On the effect of mesoporosity of FAU Y zeolites in the liquid-phase catalysis, Microporous and Mesoporous Materials, 278 (2019) 297-306.

[114] N.-N. Wang, Y. Wang, H.-F. Cheng, M.-E. Fu, Z. Tao, W.-Z. Wu, Relationship between two characteristic diffractions and the status of cationic lanthanum species in zeolite LaNaY, Journal of Porous Materials, 20 (2013) 1371-1378.

[115] Y. Zu, Y. Hui, Y. Qin, L. Zhang, H. Liu, X. Zhang, Z. Guo, L. Song, X. Gao, Facile fabrication of effective Cerium (III) hydroxylated species as adsorption active sites in CeY zeolite adsorbents towards ultra-deep desulfurization, Chemical Engineering Journal, 375 (2019) 122014.

[116] J. Jiao, Y. Qin, J. Zheng, Y. Hui, L. Zhang, X. Gao, L. Song, Synergistic mechanism between Brønsted acid site and active cerium species in hydride transfer reaction over CeY zeolites, Journal of Rare Earths, 38 (2020) 912-920.

[117] J. Hagen, Industrial catalysis: a practical approach, John Wiley & Sons, 2015.

[118] S.J. Han, S.K. Kim, A. Hwang, S. Kim, D.-Y. Hong, G. Kwak, K.-W. Jun, Y.T. Kim, Non-oxidative dehydroaromatization of methane over Mo/H-ZSM-5 catalysts: A detailed analysis of the reaction-regeneration cycle, Applied Catalysis B: Environmental, 241 (2019) 305-318.

[119] A.C. Jerdy, T. Pham, M.Á. González-Borja, P. Atallah, D. Soules, R. Abbott, L. Lobban, S. Crossley, Impact of the presence of common polymer additives in thermal and catalytic polyethylene decomposition, Applied Catalysis B: Environmental, 325 (2023) 122348.

[120] B.E. Handyla, A. Jacobo, M.G. Cárdenas Galindo, M. González, M.E. LLanos, M. de Lourdes Gúzman, F. Hernández, Combined thermometric analysis of a series of highly dealuminated USY zeolites, Topics in catalysis, 19 (2002) 249-258.

[121] M. Niwa, N. Katada, New method for the temperature-programmed desorption (TPD) of ammonia experiment for characterization of zeolite acidity: a review, The Chemical Record, 13 (2013) 432-455.

[122] J.F. Denayer, W. Souverijns, P.A. Jacobs, J.A. Martens, G.V. Baron, High-temperature low-pressure adsorption of branched c5− c8 alkanes on zeolite beta, zsm-5, zsm-22, zeolite y, and mordenite, The Journal of physical chemistry B, 102 (1998) 4588-4597.

[123] A. Corma, M. Faraldos, A. Mifsud, Influence of the level of dealumination on the selective adsorption of olefins and paraffins and its implication on hydrogen transfer reactions during catalytic cracking on USY zeolites, Applied catalysis, 47 (1989) 125-133.

[124] N.-N. Wang, Y. Wang, H.-F. Cheng, Z. Tao, J. Wang, W.-Z. Wu, Impact of cationic lanthanum species on zeolite Y: an infrared, excess infrared and Raman spectroscopic study, RSC Advances, 3 (2013) 20237-20245.

[125] J. Meusinger, A. Corma, Influence of zeolite composition and structure on hydrogen transfer reactions from hydrocarbons and from hydrogen, Journal of catalysis, 159 (1996) 353-360.

[126] J.A. van Bokhoven, Strong Brønsted Acidity in Alumina-Silicates: Influence of Pore Dimension, Steaming and Acid Site Density on Cracking of Alkanes, in: Ordered Porous Solids, Elsevier, 2009, pp. 651-668.

[127] J. Abbot, Role of Brønsted and Lewis acid sites during cracking reactions of alkanes, Applied Catalysis, 47 (1989) 33-44.

[128] B. Xu, C. Sievers, S.B. Hong, R. Prins, J.A. van Bokhoven, Catalytic activity of Brønsted acid sites in zeolites: Intrinsic activity, rate-limiting step, and influence of the local structure of the acid sites, Journal of Catalysis, 244 (2006) 163-168.

[129] H.-G. Franck, J.W. Stadelhofer, Industrial aromatic chemistry: raw materials· processes· products, Springer Science & Business Media, 2012.

[130] G. Afreen, S. Upadhyayula, Alkylation of phenol and substituted phenols with C1–C4 alcohols/olefins as an upgrading route for bio-oil oxygenates: A review, Renewable and Sustainable Energy Reviews, 147 (2021) 111189.

[131] C. Perego, P. Ingallina, Recent advances in the industrial alkylation of aromatics: new catalysts and new processes, Catalysis today, 73 (2002) 3-22.

[132] P. Beltrame, G. Zuretti, Kinetic studies for processes of liquid-phase alkylation of aromatics over solid acid catalysts, Green Chemistry, 6 (2004) 7-13.

[133] T. Ennaert, J. Van Aelst, J. Dijkmans, R. De Clercq, W. Schutyser, M. Dusselier, D. Verboekend, B.F. Sels, Potential and challenges of zeolite chemistry in the catalytic conversion of biomass, Chemical Society Reviews, 45 (2016) 584-611.

[134] P. Espeel, R. Parton, H. Toufar, J. Martens, W. Hölderich, P. Jacobs, Zeolite effects in organic catalysis, in: Catalysis and Zeolites: Fundamentals and Applications, Springer, 1999, pp. 377-436.

[135] A.K. Aboul-Gheit, S.M. Abdel-Hamid, D.S. El-Desouki, Catalytic para-xylene maximization: IV. Hydroisomerization of meta-xylene on catalysts containing platinum on differently steamed H-ZSM-5, Applied Catalysis A: General, 209 (2001) 179-191.

[136] A.A. Gusev, A.C. Psarras, K.S. Triantafyllidis, A.A. Lappas, P.A. Diddams, I.A. Vasalos, ZSM-5 additive deactivation with nickel and vanadium metals in the fluid catalytic cracking (FCC) process, Industrial & Engineering Chemistry Research, 59 (2019) 2631-2641.

[137] V.K. Diez, C.R. Apesteguia, J.I. Di Cosimo, Aldol condensation of citral with acetone on MgO and alkali-promoted MgO catalysts, Journal of Catalysis, 240 (2006) 235-244.

[138] J. Zelin, A.F. Trasarti, C.R. Apesteguía, Self-metathesis of methyl oleate on silica-supported Hoveyda–Grubbs catalysts, Catalysis Communications, 42 (2013) 84-88.

[139] V. Weekman Jr, Model of catalytic cracking conversion in fixed, moving, and fluid-bed reactors, Industrial & Engineering Chemistry Process Design and Development, 7 (1968) 90-95.

[140] C.C. Lin, S.W. Park, W.J. Hatcher Jr, Zeolite catalyst deactivation by coking, Industrial & Engineering Chemistry Process Design and Development, 22 (1983) 609-614.

[141] S.C. Reyes, L. Scriven, Analysis of zeolite catalyst deactivation during catalytic cracking reactions, Industrial & engineering chemistry research, 30 (1991) 71-82.

[142] K. Kloetstra, M. Van Laren, H. Van Bekkum, Binary caesium–lanthanum oxide supported on MCM-41: A new stable heterogeneous basic catalyst, Journal of the Chemical Society, Faraday Transactions, 93 (1997) 1211-1220.

[143] J.K. Suh, B.-H. Ha, S.-Y. Jeong, J. Koh, J.M. Lee, Characterization of transition metal-impregnated La□ Al complex oxides for catalytic combustion, Microporous Materials, 3 (1995) 657-664.

[144] G. Kamalakar, S. Kulkarni, K. Raghavan, S. Unnikrishnan, A. Halgeri, Isopropylation of naphthalene over modified HMCM-41, HY and SAPO-5 catalysts, Journal of Molecular Catalysis A: Chemical, 149 (1999) 283-288.

[145] C.R. Moreira, N. Homs, J.L.G. Fierro, M.M. Pereira, P.R. De la Piscina, HUSY zeolite modified by lanthanum: Effect of lanthanum introduction as a vanadium trap, Microporous and mesoporous materials, 133 (2010) 75-81.

[146] P. Xu, J. Lu, C. Aydin, L.M. Debefve, N.D. Browning, C.-Y. Chen, B.C. Gates, Imaging individual lanthanum atoms in zeolite Y by scanning transmission electron microscopy: Evidence of lanthanum pair sites, Microporous and Mesoporous Materials, 213 (2015) 95-99.

[147] N. Rahimi, D. Moradi, M. Sheibak, E. Moosavi, R. Karimzadeh, The influence of modification methods on the catalytic cracking of LPG over lanthanum and phosphorus modified HZSM-5 catalysts, Microporous and Mesoporous Materials, 234 (2016) 215-223.

[148] H.P. Decolatti, E.G. Gioria, S.N. Ibarlín, N. Navascués, S. Irusta, E.E. Miró, L.B. Gutierrez, Exchanged lanthanum in InHMOR and its impact on the catalytic performance of InHMOR. Spectroscopic, volumetric and microscopic studies, Microporous and Mesoporous Materials, 222 (2016) 9-22.

[149] M.D. González, Y. Cesteros, P. Salagre, Establishing the role of Brønsted acidity and porosity for the catalytic etherification of glycerol with tert-butanol by modifying zeolites, Applied Catalysis A: General, 450 (2013) 178-188.

[150] B. Dalla Costa, M. Peralta, C. Querini, Gas phase dehydration of glycerol over, lanthanum-modified beta-zeolite, Applied Catalysis A: General, 472 (2014) 53-63.

[151] Z. Zhao, W. Qiao, G. Wang, Z. Li, L. Cheng, Alkylation of α-methylnaphthalene with long-chain olefins catalyzed by rare earth lanthanum modified HY zeolite, Journal of Molecular Catalysis A: Chemical, 250 (2006) 50-56.

[152] V.L. Zholobenko, M.A. Makarova, J. Dwyer, Inhomogeneity of Broensted acid sites in H-mordenite, The Journal of Physical Chemistry, 97 (1993) 5962-5964.

[153] D.B. Lukyanov, T. Vazhnova, N. Cherkasov, J.L. Casci, J.J. Birtill, Insights into Brønsted acid sites in the zeolite mordenite, The Journal of Physical Chemistry C, 118 (2014) 23918-23929.

[154] C. Lamberti, S. Bordiga, A. Zecchina, M. Salvalaggio, F. Geobaldo, C.O. Areán, XANES, EXAFS and FTIR characterization of copper-exchanged mordenite, Journal of the Chemical Society, Faraday Transactions, 94 (1998) 1519-1525.

[155] R. Gounder, E. Iglesia, Catalytic consequences of spatial constraints and acid site location for monomolecular alkane activation on zeolites, Journal of the American Chemical Society, 131 (2009) 1958-1971.

[156] L. Domokos, L. Lefferts, K. Seshan, J. Lercher, The importance of acid site locations for n-butene skeletal isomerization on ferrierite, Journal of Molecular Catalysis A: Chemical, 162 (2000) 147-157.

[157] V.A. Veefkind, M.L. Smidt, J.A. Lercher, On the role of strength and location of Brønsted acid sites for ethylamine synthesis on mordenite catalysts, Applied catalysis A: general, 194 (2000) 319-332.

[158] A. Bhan, A.D. Allian, G.J. Sunley, D.J. Law, E. Iglesia, Specificity of sites within eight-membered ring zeolite channels for carbonylation of methyls to acetyls, Journal of the American Chemical Society, 129 (2007) 4919-4924.

[159] B. Klingenberg, M.A. Vannice, Influence of pretreatment on lanthanum nitrate, carbonate, and oxide powders, Chemistry of materials, 8 (1996) 2755-2768.

[160] C.S. Triantafillidis, N.P. Evmiridis, Dealuminated H− Y Zeolites: Influence of the Number and Type of Acid Sites on the Catalytic Activity for Isopropanol Dehydration, Industrial & engineering chemistry research, 39 (2000) 3233-3240.

[161] D. Mei, J.A. Lercher, Mechanistic insights into aqueous phase propanol dehydration in H-ZSM-5 zeolite, AIChE Journal, 63 (2017) 172-184.

[162] J.-L. Dubois, G. Postole, L. Silvester, A. Auroux, Catalytic Dehydration of Isopropanol to Propylene, Catalysts, 12 (2022) 1097.

[163] C. Perego, S. Amarilli, A. Carati, C. Flego, G. Pazzuconi, C. Rizzo, G. Bellussi, Mesoporous silica-aluminas as catalysts for the alkylation of aromatic hydrocarbons with olefins, Microporous and Mesoporous Materials, 27 (1999) 345-354.

[164] Y. Liu, G. Cheng, E. Baráth, H. Shi, J.A. Lercher, Alkylation of lignin-derived aromatic oxygenates with cyclic alcohols on acidic zeolites, Applied Catalysis B: Environmental, 281 (2021) 119424.

[165] P.G. Smirniotis, E. Ruckenstein, Alkylation of Benzene or Toluene with MeOH or C2H4 over ZSM-5 or. beta. Zeolite: Effect of the Zeolite Pore Openings and of the Hydrocarbons Involved on the Mechanism of Alkylation, Industrial & engineering chemistry research, 34 (1995) 1517-1528.

[166] A. Corma, S. Iborra, Oligomerization of alkenes, Catalysts for Fine Chemical Synthesis: Microporous and Mesoporous Solid Catalysts, 4 (2006) 125-140.

[167] M.-F. Reyniers, H. Beirnaert, G. Marin, Influence of coke formation on the conversion of hydrocarbons: I. Alkanes on a USY-zeolite, Applied Catalysis A: General, 202 (2000) 49-63.

[168] P. Yarlagadda, C. Lund, E. Ruckenstein, Oligomerization of ethene and propene over composite zeolite catalysts, Applied catalysis, 62 (1990) 125-139.

[169] M. Guisnet, P. Magnoux, Coking and deactivation of zeolites: influence of the pore structure, Applied Catalysis, 54 (1989) 1-27.

[170] A.K. Ghosh, R.A. Kydd, A Fourier-transform infrared spectral study of propene reactions on acidic zeolites, Journal of Catalysis, 100 (1986) 185-195.

[171] M. Díaz, E. Epelde, J. Valecillos, S. Izaddoust, A.T. Aguayo, J. Bilbao, Coke deactivation and regeneration of HZSM-5 zeolite catalysts in the oligomerization of 1-butene, Applied Catalysis B: Environmental, 291 (2021) 120076.

[172] N. Hosseinpour, Y. Mortazavi, A. Bazyari, A.A. Khodadadi, Synergetic effects of Y-zeolite and amorphous silica-alumina as main FCC catalyst components on triisopropylbenzene cracking and coke formation, Fuel processing technology, 90 (2009) 171-179.

[173] F. Bauer, H.G. Karge, Characterization of coke on zeolites, in: Characterization II, Springer, 2006, pp. 249-364.

[174] H.G. Karge, H. Darmstadt, A. Gutsze, H.-M. Vieth, G. Buntkowsky, 13C MAS NMR and related studies of coke formation on H-ZSM-5, in: Studies in Surface Science and Catalysis, Elsevier, 1994, pp. 1465-1474.

[175] L. Young, S. Butter, W. Kaeding, Shape selective reactions with zeolite catalysts: III. Selectivity in xylene isomerization, toluene-methanol alkylation, and toluene disproportionation over ZSM-5 zeolite catalysts, Journal of Catalysis, 76 (1982) 418-432.

[176] M.-F. Reyniers, Y. Tang, G. Marin, Influence of coke formation on the conversion of hydrocarbons: II. i-Butene on HY-zeolites, Applied Catalysis A: General, 202 (2000) 65-80.

[177] K. Cumming, B.W. Wojciechowski, Hydrogen transfer, coke formation, and catalyst decay and their role in the chain mechanism of catalytic cracking, Catalysis Reviews, 38 (1996) 101-157.

[178] B. Wang, G. Manos, Deactivation studies during 1-pentene reactions over HUSY zeolite, Chemical Engineering Journal, 142 (2008) 217-223.

[179] E.E. Bickel, S. Lee, R. Gounder, Influence of Brønsted Acid-Site Density on Reaction-Diffusion Phenomena that Govern Propene Oligomerization Rate and Selectivity in MFI Zeolites, ACS Catalysis, 13 (2023) 1257-1269.

[180] A.N. Mlinar, P.M. Zimmerman, F.E. Celik, M. Head-Gordon, A.T. Bell, Effects of Brønsted-acid site proximity on the oligomerization of propene in H-MFI, Journal of catalysis, 288 (2012) 65-73.